Motion Compensation for Floating Installation of Offshore Wind Turbines

Fidalgo Domingos, D.A.

Important note
To cite this publication, please use the final published version (if applicable).
Please check the document version above.

MOTION COMPENSATION FOR FLOATING INSTALLATION OF OFFSHORE WIND TURBINES

David André Fidalgo Domingos

MOTION COMPENSATION FOR FLOATING INSTALLATION OF OFFSHORE WIND TURBINES

Dissertation

for the purpose of obtaining the degree of doctor
at Delft University of Technology,
by the authority of the Rector Magnificus Prof. dr. ir. T.H.J.J van der Hagen,
chair of the Board of Doctorates
to be defended publicly on
Thursday 16 October, 2025 at 15:00

by

David André FIDALGO DOMINGOS

Master of Science in Marine Technology,
Delft University of Technology, the Netherlands,
born in Loulé, Portugal.

This dissertation has been approved by the promotors.

Composition of the doctoral committee:

Rector Magnificus,	chairperson
Prof. dr. ir. J.W. van Wingerden,	Delft University of Technology, promotor
Dr.ir. P.R. Wellens,	Delft University of Technology, promotor

Independent members:

Dr.ir. A.J.H.M Reniers,	Delft University of Technology
Prof. dr. X. Zhang,	Shanghai Jiao Tong University
Dr. ir. J.P. Schilder,	University of Twente
Dr. ir. W.T. van Horssen,	Delft University of Technology
Prof. Dr. B. Jayawardhana,	University of Groningen

TUDelft Delft University of Technology

An electronic version of this dissertation is available at
http://repository.tudelft.nl/.

CONTENTS

SUMMARY

The decarbonisation of the energy sector is an important and urgent step in preventing a long lasting chain of climatic changes. One of the most promising renewable energy sources is wind energy. Driven by more stable wind conditions and abundant space, the offshore wind market has grown significantly, leading to larger turbines being installed farther offshore in deeper waters. However, this brings challenges to an industry, so far, relaying on jack-up vessels. An alternative is floating crane-vessels, with their large capacity cranes and the ability of operating at any water depth, these vessels can take the next generation of wind farms to new depths. However, the mitigation of wind- and wave-induced motions still remains a challenge.

Currently, damping tugger lines are an offshore industry standard for the mitigation of payload motions. Often designed to handle a wide variety of payloads and with limited actuation capacity in the side-lead direction, damping tuggers are often unable to answer to the specific needs of the offshore wind market. This has driven research into motion compensation for blade and foundation installations, yet literature regarding motion compensation solutions for wind turbine tower installations remains limited. In an attempt bridge this gap, this thesis focuses on the development of methodologies and motion compensation strategies to enhance the understanding and workability of floating installations of offshore wind turbine towers.

To assess the impact of wind and wave loads on the workability of the operation, a frequency-domain framework is introduced, verified and analyzed in the context of a case-study, where *SSCV Prometheus* installs a DTU 10 MW wind turbine tower at Figueira da Foz Wind Farm (Portugal). The results highlight the impact of wave loads on workability, stressing the relevance of payload motion control.

The representation of offshore operations by means of reduced-order models can lead to shortcomings, due to the high complexity and uncertainty present in an offshore environment. To prevent this, model-scale tests are often conducted for validation purposes. Yet, due to the nature of scaling laws, it is not possible to consistently scale wind and wave loads simultaneously. Therefore, a full-scale measurement campaign of the first-ever floating installation of an offshore wind turbine tower was conducted. The results show the impact of wave loads on tower motions as well as the presence of wind-driven vortex induced vibrations at full-scale.

With a goal of providing a more tailored solution to enhance the workability of floating installations, the use of a hook-mounted active control moment gyroscope is investigated. Given the limitations of model-free controller synthesis and manual loop-shaping a mixed sensitivity $\mathcal{H}_\infty$ optimal control framework is proposed instead. This allows to achieve a significant reduction in tower motions across a wide range of payout lengths and tower sizes. These results highlight the relevance of model-based control methods in offshore applications and the potential of gyroscopic actuation in the field of heavy-lift installations.

The contributions of this thesis highlight the challenges and relevance of motion compensation for the floating installation of wind turbine towers, advancing the state-of-the-art and contributing to the future of the offshore wind sector. Providing in this way, its sand-grain-sized contribution in tackling one of the greatest challenges in human history: climate change.

SAMENVATTING

Om een langdurige keten van klimaatveranderingen te voorkomen is het belangrijk en urgent om de energiesector te verduurzamen. Een van de meest veelbelovende duurzame energiebronnen is windenergie. De offshore windmarkt is, dankzij de stabielere windcondities en een overvloed aan ruimte, de afgelopen jaren aanzienlijk gegroeid. Dit heeft ertoe geleid dat steeds grotere turbines verder uit de kust en dieper in het water worden geïnstalleerd. Dit brengt echter nieuwe uitdagingen met zich mee voor een sector die tot nu toe grotendeels afhankelijk was van jack-up schepen. Drijvende kraanschepen bieden hier een alternatief voor. Met hun hijscapaciteit en het vermogen om op elke waterdiepte te opereren maken deze schepen de aanleg van de volgende generatie windparken mogelijk. Toch blijft het beperken van bewegingen die worden veroorzaakt door wind en golven een hardnekkige uitdaging.

Momenteel vormen dempende tugger lines de standaard in de offshore windmarkt voor het verminderen van ladingbeweging. Vaak zijn deze systemen ontworpen voor een breed scala aan ladingen maar ze hebben een beperkt bereik in zijwaartse richting. Hierdoor sluiten ze vaak niet goed aan op de specifieke eisen van de offshore windmarkt. Dit heeft geleid tot onderzoek naar bewegingscompensatie bij de installatie van rotorbladen en funderingen. Echter worden er in de literatuur nauwelijks oplossingen beschreven voor het plaatsen van windturbinetorens. In een poging om deze leemte op te vullen focust dit proefschrift op methoden en strategieën die de werkbaarheid vergroten van drijvende installaties van windturbinetorens. Om de invloed van wind- en golfbelastingen op de werkbaarheid van de installatie te onderzoeken is een frequentiedomeinmodel ontwikkeld, geverifieerd en toegepast in een casestudy waarin de *SSCV Prometheus* een DTU 10 MW windturbinetoren installeert in het Figueira da Foz Windpark (Portugal). De resultaten tonen aan dat golfbelastingen een grote invloed hebben op de werkbaarheid en benadrukken het belang van effectieve bewegingscontrole.

Het modelleren van offshore-operaties met reduced-order modellen kan tekortkomingen opleveren door de hoge mate van complexiteit en onzekerheid in de offshore omgeving. Om dit te voorkomen worden vaak modelproeven op schaal uitgevoerd ter validatie. Door de beperkingen van schaalwetten is het echter niet mogelijk om wind- en golfbelastingen tegelijk correct te schalen. Om die reden is een full-scale meetcampagne uitgevoerd van de eerste drijvende installatie van een offshore windturbinetoren. De resultaten laten de impact van zowel golfbelastingen op torenbewegingen als de aanwezigheid van windgedreven vortex-geïnduceerde trillingen zien op ware grootte.

Met het oog op een meer op maat gemaakte oplossing om de werkbaarheid van drijvende installaties te verbeteren is het gebruik van een aan de haak gemonteerde actieve 'control moment gyroscope' onderzocht. Vanwege de beperkingen van modelvrije regelaars en handmatige 'loop shaping' is in plaats daarvan gekozen voor een mixed-sensitivity $\mathscr{H}_\infty$-optimalisatieaanpak. Hiermee worden torenbewegingen, bij een grote verscheidenheid aan kabeluitgiften en torenafmetingen, significant gereduceerd. De

resultaten onderstrepen het belang van modelgebaseerde regelmethoden in offshore toepassingen en laten het potentieel zien van giroscopische actuatie voor zware hijsoperaties.

Dit proefschrift geeft inzicht in de uitdagingen en het belang van bewegingscompensatie bij drijvende installatie van windturbinetorens en draagt bij aan de verdere ontwikkeling van de offshore windsector. Daarmee levert het een kleine maar betekenisvolle bijdrage aan het aanpakken van een van de grote uitdagingen van onze tijd: klimaatverandering.

NOMENCLATURE

A_{PT}	Passive Tugger sectional area		s_F	Active tugger load PDS
a'	Acceleration measurement		$T_{install}$	Installation time
a_Ω	Acceleration due to rotation		T_p	Waves peak period
B	Vessel's beam		V_w	Wind speed
BM_l	Longitudinal metacentric radius		W	Workability
BM_t	Transverse metacentric radius		y_t	Tower bottom horizontal motion
b_A / b_{aero}	Aerodynamic damping		y_k	Crane tip horizontal motion
b_C	Precession damping			
b_D	Additional system damping		α	Flywheel's spinning angle
b_{sys}	System damping		$\Delta_{Lim}^{y_t}$	y_t installation tolerance
C_D	Drag coefficient		$\Delta_{Lim}^{\phi_b}$	ϕ_b installation tolerance
D_t / d_T	Tower diameter		Δ_ω	Discretization frequency
d_{PT}	Passive tugger-line diameter		∇	Vessel's submerged volume
E_{PT}	Passive Tugger Young's Modulus		ζ	Wave amplitude
F_A	Aerodynamic force		ζ_f	Filter damping ratio
f_n	Natural frequency		ρ_w	Salt-water density
g	Gravitational acceleration		ρ_{air}	Air density
H_s	Significant wave height		σ	Standard deviation
H_k	Crane tip height		τ	Torque applied to the flywheel
I	Identity matrix		$\tau_\psi^{\lim}$	Precession stiffness
I_f	Flywheel inertia		τ_S	Accelerometer sensor delay
I_t	Tower moment of inertia		ϕ_t	Tower angle
k_{PT}	Passive Tugger axial stiffness		ϕ_s	Sling angle
K_ψ	Precession stiffness		ϕ_b	Hoisting cable angle
L_b	Payout length		ϕ	Flywheel's precession angle around x
L_s / l_s	Sling length		ψ	Flywheel's precession angle around z
L_t / L_c	Tower height		Ω'	Angular velocity measurement
L_{PT}	Passive tugger length		ω	Frequency
L_g	CMG height		ω_c	Filter cutting frequency
M_t / M	Tower mass			
M_b / m	Block mass		$AHRS$	Attitude and Heading Reference System
M_f	Flywheel mass		CT	Constant Tension
R	Time-invariant rotation matrix		CoG	Center of Gravity
Re	Reynolds number		CMG	Control moment gyroscope
S_r	Response PDS		DP	Dynamic Positioning
S_ζ	Waves PDS		DoF	Degrees of Freedom
S_w	Wind PDS		$GNSS$	Global Navigation Satellite System
s_a	Acceleration PDS		IMU	Passive Tugger Young's Modulus

LOA	Length Over All	*SSCV*	Semi-Submersible Crane Vessel
OWT	Offshore Wind Turbine	*VIV*	Vortex Induced Vibrations
PDS	Power density spectrum		
RAO	Response Amplitude Operator		

1

INTRODUCTION

Everyone is entitled to his own opinions,
but not to his own facts.

-Senator Pat Moynihan

Driven by a permanent ambition of improving well-being, we arrived to a point where action must be urgently taken to prevent a long lasting chain of climatic changes. The decarbonisation of the energy sector is an important step in reducing global warming. One of the most promising sources of renewable energy is wind. Driven by more stable wind conditions and limited on-shore space, the offshore wind market has grown significantly in the past decades, resulting in bigger turbines further offshore, into deeper waters. This brings challenges to an industry, so far, depended on jack-up vessels. An alternative is floating crane-vessels, not limited by water depth and sea-bed conditions, these vessels can take the next generation of wind farms to new depths. Yet, the mitigation of wind and wave induced motions remains a challenge. The present work addresses this by developing methodologies and motion compensation strategies to enhance the understanding and workability of floating installation of wind turbines. Contributing, in this way, for the future of the offshore wind sector.

1

This chapter situates the contributions of this work within environmental, economic, and scientific contexts, highlighting its positive (although sand-grain sized) contribution in addressing one of the greatest challenges in human history: global warming.

The coming section provides the reader with a summary on the whys and hows of climate change. Reflecting some of the author's motivations in engaging in this work.

1.1. WHY RENEWABLE ENERGY?

Controlling fire was the first step in a journey of ever increasing energetic demands, contributing for the expansion of the human species and the shaping of society as we know it. Up until the end of the 17th century, the main source of energy was the burning of "traditional biomass", such as wood and agricultural by-products. However, there was a turning point for world and society in the 18th century: The industrial revolution. This came to unlock the use of a new energy source, fossil fuels [101]. Their abundance, energy density and accessibility propelled industrialization, population growth and consequently energy consumption. Within a 100 years period, fossil fuels became the main energy source to power society Figure 1.1, and today constitute close to 80% of the global energy consumption [103].
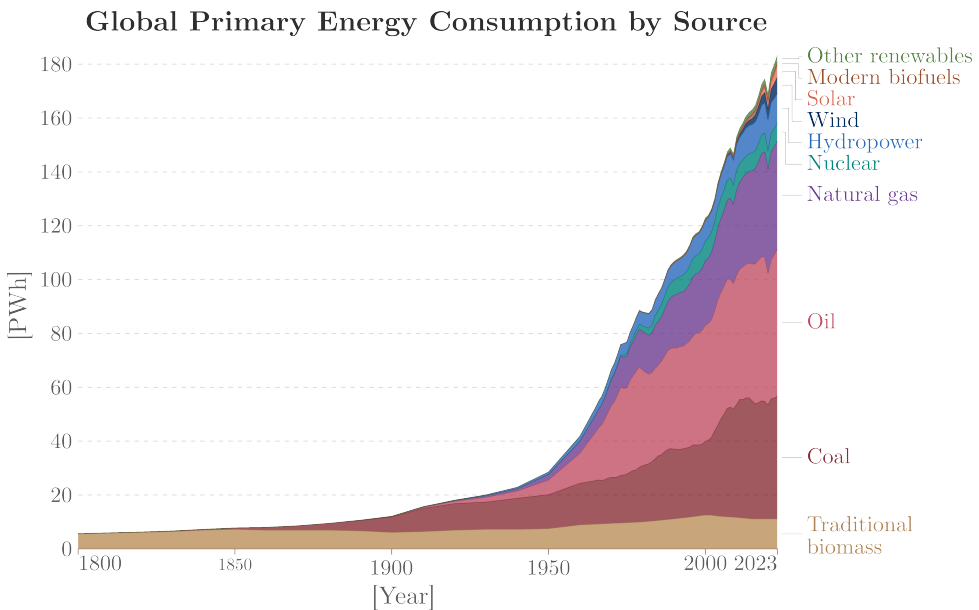
Figure 1.1: Global primary energy consumption by in peta watts hour since the industrial revolution [103]. Note that primary energy refers to the energy of the resources before being transformed.

However, there is a price to pay for the social and technological advances brought by fossil fuels. This source of energy is the result of decomposing organic matter over millions of years. Extracting and burning it releases powerful green house gases (GHGs) into the atmosphere (*e.g.* carbon dioxide, methane and nitrous oxide), which trap heat near the Earth's surface [104]. At the present time the burn and extraction of fossil fuels are

the source of 70% of GHG emissions [34], making them the main responsible for the rapid increase in average global temperature [102]. As a consequence, relative to pre-industrial times, each of the past 10 years was the warmest on record and 2024 exceeded for the first time 1.5 C mark of global average temperature increase. [19]. This trend is contributing for a steep decline in biodiversity [105, 74], putting at risk the ecological balance of the planet. To assess this risk, a set of climate tipping points have been defined. These are critical thresholds that when exceeded can lead to a significant and prolonged change of the planet's climate [69], which can last from decades to millennia. The 1.5°C threshold, at which we currently are, is likely the last chance to revert climate change without leaving long-term marks in the world's climate. Beyond this point a chain of events unravel, with the first one expected to be a widespread mortality of warm-water coral reefs [69]. At 2°C and beyond, systems such as the Amazon Rain Forest can tip, and a permanent collapse of Greenland and West Antarctic ice sheets is likely [69]. With the tipping of these systems it becomes increasingly difficult to revert global warming, even if temperatures fall below the thresholds again [69]. In this scenario, a loss of living conditions is expected due to extreme heat, groundwater depletion and spread of viruses [46, 84, 28].

What can be done to limit global warming? This question can be approached from multiple angles, *e.g.* land use, waste management, economy, energy, etc... In here we focus on the latter, energy. As earlier discussed, the burning and extraction of fossil fuels is the main caused of global warming. Therefore, it should be of primary importance to reduce the dependency on this source of energy. The longer we take, the bigger and sharper the reduction needs to be to prevent long term changes of the planet's climate [49]. Two promising renewable energy alternatives are solar and wind energy. With a levelized cost of energy (LCOE) less than half that of coal, onshore wind energy is the cheapest source of energy and among the cleanest and safest [107, 100]. The coming section elaborates on the role of its offshore counterpart on the energy transition.

1.2. The Role of Offshore Wind in the Energy Transition

Wind energy not only plays a crucial role in the decarbonization of the energy sector but also contributes to the energetic independence of states. Currently, this source of energy contributes for about 25% of the global renewable energy mix [37], most of which produced onshore. However, the growth of onshore installations is capped by public opinion and space limitations [9]. An alternative is offshore wind energy production, which allows for the installation of larger turbines in regions of higher wind speeds, resulting in exponential power gains [76]. As result, the European Union has set the ambitious target of achieving a total of 88 GW of offshore wind capacity by 2030 and 360 GW in 2050 [5], attracting large investments [23] and propelling the development of larger turbines, Figure 1.2. Therefore, a significant increase of the annual installed capacity is expected in the coming years, Figure 1.3.

The installation of offshore wind turbines consists of many high precision operations. Therefore, a steady platform on the sea greatly improves the safety and complexity of the operation. For this reason, jack-up vessels became an industry standard regarding the installation of wind turbines [43]. These vessels use large metallic legs to lift them-

1
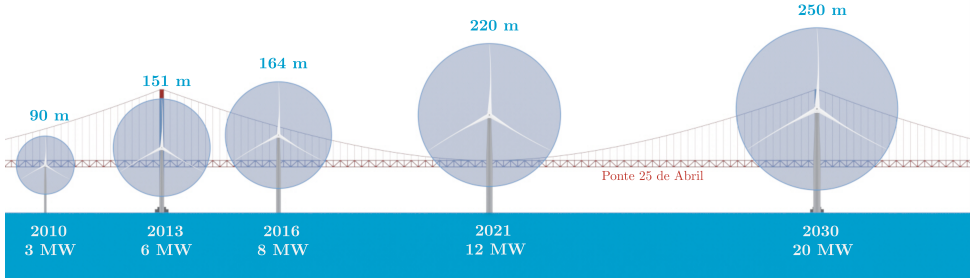
Figure 1.2: Evolution of commercially available wind turbine power and diameters over time [10].
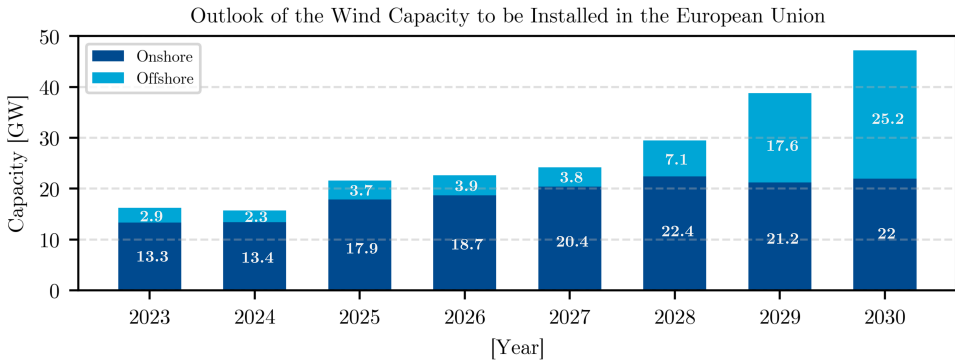
Figure 1.3: 2023-2030 outlook of new installed wind capacity in the European Union [48].

selves above the sea surface, mitigating wave-induced motions during installation, see Figure 4.1.

However, the increased stability comes at a cost: operational limitations in water depth, dependency on seabed conditions, vulnerability to changes in wind direction, and more operational time due to jacking operations [27]. This brings challenges to jack-up vessels to keep up with the demands of the rapid evolving offshore wind market. In which, wind farms are moving farther offshore into deeper waters due to more stable wind conditions and the depletion of near-shore locations [94, 38]. An alternative is the use of already existing floating crane vessels. However, as will be discussed in the following section, these vessels bring a new set of challenges, which have motivated the present work.

1.3. FLOATING INSTALLATION

Initially designed for the fossil fuel industry in the mid-1950s [93], floating crane-vessels were built to conduct complex operations at sea involving some of the biggest and heaviest mobile structures on the planet.

In contrast to jack-up vessels, floating vessels use dynamic positioning (DP) systems for station keeping. Over the years, their design converged to a semi-submersible type

(a) A wind turbine jack-up installation vessel [21].

(b) Heerema's SSCV *Sleipnir* performing a floating installation of an offshore wind turbine [39].

Figure 1.4: Offshore installation vessels.

of vessel. Despite their sensitivity to hanging loads in comparison to mono-hulls [88, 33], semi-submersible crane-vessels (SSCVs) provide flexible ballasting and enough deck area to accommodate two cranes of large capacity, outreach and lifting heights [33], see Figure 1.4b.

These characteristics make them also suited for the deployment of larger wind turbines at water depths beyond the limits of jack-up vessels [57], saving jacking time and allowing for real-time adjustment of the vessel's orientation relative to wind direction, characteristics which are essential for the installation of the next generation of wind farms, with larger turbines and further offshore. However, floating vessels are more susceptible to wind and wave induced motions compared to jack-up vessels [65, 29], which cause undesired motions of payloads (such as wind turbine components see Figure 4.2c), hindering the operation and consequently reducing workability. With the latter being here defined as:

Workability represents the percentage of time for which a pre-defined operational limit is not exceeded during an installation time-frame.

In an attempt to enable the floating installation of wind turbines, multiple installation methods have been proposed in the literature [72, 55]. A promising concept is a single-lift installation method [20]. This method involves using both cranes of an SSCV to transport and install a fully assembled wind turbine, thereby reducing the number of installation steps offshore. However, a major drawback is that this approach requires the transportation of fully assembled turbines offshore using feeder barges, which is both costly and risky. In contrast, this thesis focuses on enabling the floating installation of wind turbines through active motion compensation systems. These systems use sensors to detect payload motions and actuators to counteract them based on a mathematical algorithm (i.e., a controller), as discussed in the following section. However, the development of such active motion control systems requires addressing a gap in the literature regarding the dynamic behavior of floating wind turbine installation and its response to environmental disturbances, which is a key objective of this thesis.

1

1.4. OFFSHORE MOTION COMPENSATION

Pendulation refers to the oscillatory motion of pendulum-like systems. Given their presence in a broad range of practical applications, from small-scale mechanisms like watches to large-scale machinery such as cranes, controlling these oscillatory motions has been a widely researched topic with significant real-world implications.

One of the earliest contributions to pendulation control dates back to the 1960s when Alsop et al. proposed an automation system for an ore unloader crane [11]. Since then, multiple pendulation control strategies have been proposed, enhancing efficiency and safety of industrial processes. A significant portion of these studies has focused on gantry cranes (see Figure 1.5a), which are commonly used in mining sites, factories, and ports. Research in this area has aimed to improve automation and implement command shaping controllers that minimize residual pendulation caused by operator inputs [91, 110]. Over time, more advanced methods such as robust, adaptive, and nonlinear control have been introduced [52, 50, 114].
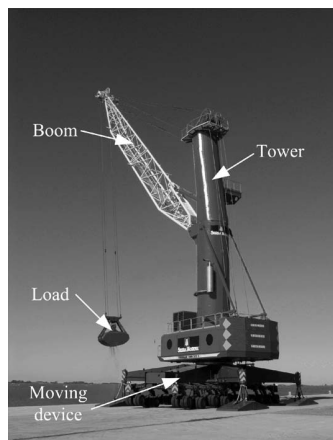
Similarly, progress has been made in payload motion control for rotary boom cranes, used in both onshore and offshore applications (see Figure 1.5b) [87, 53]. However, pendulation control in these systems is particularly challenging due to the coupling between the vertical and radial motions of the payload when luffing the boom (*i.e.* changing the boom's angle relative to the crane's tower).

Pendulation mitigation is especially critical in offshore operations where wind and wave disturbances can induce significant payload motions, hindering the operations. Given the importance of precision and safety in this field, substantial research has focused on motion compensation strategies for various offshore crane types and sizes [108, 79]. So far, most of the available literature has relied on a key assumption, which is the mitigation of payload motions by actuating the crane itself. Although it is a viable approach for smaller cranes, for larger cranes this method becomes less effective due to the crane's high inertia, limited actuation bandwidth, and increased wear and tear. A more efficient alternative is to use dedicated actuators that control payload motion without relying on the crane's actuators. Given the size of offshore heavy-lift cranes for wind turbine installations (see Figure 4.2a), this is the approach adopted in the present work.

Motion compensation of suspended payloads can be split in: heave compensation and horizontal-plane motion compensation, see Figure 4.2c. The first one refers to the mitigation of vertical motions, *i.e.* motions orthogonal to the horizontal plane, as defined in Figure 4.2c. Sudden motions in this direction can cause significant damages and pose risks to safety on the sea. To prevent this, active hoisting cable length control was developed and it has become a default solution especially for sub-sea applications, such as the deployment of remotely operated underwater vehicles [86]. More recently, a novel type of hook-mounted semi-active heave compensators was proposed [1]. This new generation of heave compensation reduces the wear and tear of hoisting cables and provides an answer for high precision operations, such as floating installation of wind turbines or the lifting of wind turbine components from feeder barges. In contrast, the compensation of horizontal plane motions remains an open challenge. The use of cables attached to the payload or hook block have become standard in the industry due to their simplicity and reliability, see Figure 4.2b. These cables, known as tugger lines (or tuggers), are often actuated via a winch and use strain sensors and encoders to measure

(a) Iconic gantry crane from Lisnave shipyard, located in Lisbon (Portugal) [71].   (b) Example of a land based boom crane [87].

Figure 1.5: Industrial cranes.

(a) SSCV *Sleipnir* performing the first floating installation of a wind turbine tower.
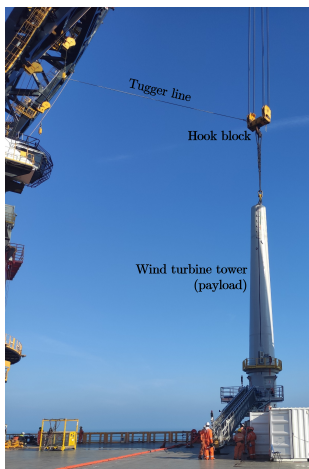
(b) SSCV *Sleipnir's* tugger line system during offshore wind turbine tower installation.
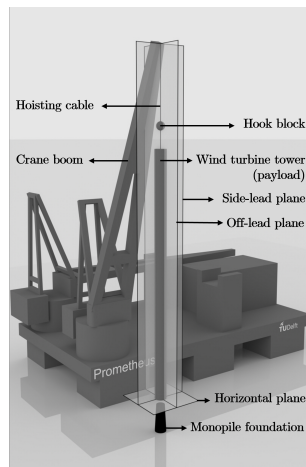
(c) Illustration of SSCV *Prometheus* [44] installing a wind turbine tower accompanied by relevant nomenclature.

Figure 1.6: Floating installation of wind turbine towers.

line tension and speed. The first active tugger line system was designed to maintain constant line tension [81]. This approach aids in the positioning of payloads and prevents sudden surges in line tension, also known as snap loads, which could lead to the line's rupture. However, constant tension tugger lines do not mitigate pendulation. To address this, damping tuggers were more recently proposed as a concept for payload motion reduction [81, 64]. This method aims to reduce pendulation through a control feedback loop, where line tension varies proportionally with its velocity. Simulations and tank

tests have demonstrated promising results. However, these studies have not explored the robustness and performance of the control system for different payload types and sizes. A drawback of this system is that it is not possible to compensate motions in the side-lead and off-lead planes in an independent manner, see Figure 4.2c. This has motivated research into alternative mechanisms, one being the use of a large number of lifting wires which can compensate both vertical and horizontal plane motions using an ingenious control allocation algorithm [98]. However, this method requires a novel configuration of a crane system which is fundamentally different from traditional ones currently used in the offshore heavy-lifting industry, not answering to the needs of existing heavy-lift vessels. Therefore, more research is needed in the development of motion compensation solutions for existing heavy-lift crane-vessels.

In the field of motion compensation for offshore wind turbine installation, it is essential to consider the specificity of the operation. The unique demands of the offshore wind industry have motivated driven research into tailored motion compensation solutions, motivated by three main factors: 1) Compared to offshore oil and gas structures, wind turbine components have a small weight to size ratio, making them more susceptible to wind induced motions; 2) The assembly of a wind turbine consists of multiple delicate operations; and 3) in contrast to oil and gas structures, offshore wind turbines are repetitively installed at the scale of hundreds, all featuring nearly identical components. Current literature in motion compensation for offshore wind turbine installation can be mostly divided in two main categories: installation of foundations [85, 109] and blade installation [58, 96]. This leaves a gap in motion compensation solutions for tower installations.

A challenging aspect of motion compensation for wind turbine tower installation is that the attachment of installation aiding devices to the tower can compromise its structural integrity and corrosion protection coating. When using tugger lines this often means attaching them to the hook-block instead (*i.e.* the crane's hook), as shown in Figure 4.2b. This results in an challenging control problem, since the controller is indirectly controlling the tower position, similarly to reversing a car with a trailer. The added control difficulty arises from the presence of system dynamics between the location of the actuator (*e.g.* the hook-block) and the desired location of motion control performance (the tower bottom), requiring a careful controller design. In an ingenious attempt to overcome this issue, Atzampou *et al.* have proposed a novel actuator using electromagnets, which can induce a force directly on the tower without being in direct contact with it [16]. However, the simultaneous control of motions in the side-lead and off-lead planes remains a challenge since in the proposed system the direction of magnetic force is unique and constant.

So far, it is possible to identify three main gaps in literature regarding motion compensation for floating installation of wind turbine towers: 1) Lack of specificity for tower installations, *e.g.* [81]; 2) too low technological readiness level for offshore application, *e.g.* [98]; and 3) lack of side-lead motion control ability, *e.g.* [16]. These gaps lead to to the objectives of this thesis, in the following section.

1.5. This Thesis

Since the 1950s that the offshore industry has been playing a key role in the energy market and it is expected to continue, this time with the ambition of decarbonizing the energy sector, by means of offshore renewable energy. As motivated in the previous sections, floating installation of wind turbines plays an important role in achieving this goal, enabling the future of offshore wind farms. However, controlling the motions of wind turbine towers during floating installation is currently a challenge to which there is no clear answer. In an attempt to contribute towards a solution, we formulate the following objective for this thesis:

> **Thesis Objective:** To develop a methodology for assessing the impact of wind- and wave-induced motions on the floating installation of wind turbine towers and exploring their mitigation through (novel) motion compensation techniques.

The novelty of floating installation of wind turbines and the competitive nature of the offshore wind market have resulted in a limited amount of literature in the field. Therefore, the first step in investigating motion compensation strategies is to develop an understanding of the impact of environmental disturbances and system's characteristics on workability. Mathematical models are comprehensive and affordable tools to assess this. Commonly used in the field of systems and control, linear frequency-domain models have proven to be valuable for the analysis and control of dynamic systems [32]. Therefore, the first contribution of this thesis concerns the development of a frequency-domain framework and its application in the context of a case-study, for which a workability, sensitivity and dynamic error budgeting analysis are performed to assess the impact of environmental disturbances on the operation:

> **Contribution I**: A frequency-domain method to assess the impact of waves and wind on the workability of floating installations of wind turbine towers.

As a by-product of this first contribution, the second contribution aims at stimulating open-research and consists of a first of its kind reference floating crane-vessel:

> **Contribution II**: Introduction of an open-source semi-submersible crane-vessel (*SSCV Prometheus*) and respective data.

Offshore installations take place in an uncontrolled and complex environment, characterized by a high degree of uncertainties. When representing such systems, mathematical models consider a set of assumptions and simplifications, which can lead to shortcomings. To prevent this, model-scale tests are often conducted for validation purposes. However, due to the nature of scaling laws, it is not possible to ensure a consistent scaling of wind and wave loads simultaneously. To address this limitation, a full-scale measurement campaign was conducted to provide a more in-depth understanding of this type of operation. Consequently, the third contribution provides a dataset on the motions of the first-ever full-scale floating installation of an offshore wind turbine tower, along with an analysis of its dynamic behavior.

> **Contribution III**: A motion dataset from the first full-scale floating instal-
> lation of a wind turbine tower and an analysis of its dynamic behavior.

Despite the limitation of tugger lines in controlling side-lead motions, these are employed for a wide range of payload types and sizes. Given the scale of wind farms, a more tailored solution can result in significant gains in safety and installation time. Therefore, a hook-mounted active Control Moment Gyroscope is proposed as an alternative motion compensation strategy to enhance the workability of floating installation of offshore wind turbine towers. Leading to the final contribution of this thesis:

> **Contribution IV**: Development of a model-based control strategy for a
> gyroscopic actuator to enhance the workability of floating installation of
> wind turbine towers.

1.5.1. Outline
The subsequent 4 chapters detail the contributions of this thesis. Written in an independent manner, each chapter contains its own introduction, conclusions and notation.

In **Chapter 2** a frequency-domain framework is proposed to perform extensive site-specific analysis, of floating installations of wind-turbine towers, subjected to wind and wave loads. The versatility and potential of this framework is demonstrated with a case-study of a wind farm near the coast of Portugal. The results highlight the effect of wave loads on yearly workability, the impact of tower size and excitation frequencies on tower motions. Furthermore, the open-source semi-submersible crane-vessel *SSCV Prometheus* is introduced. This chapter is based on the following publications [43, 44].

Chapter 3 provides an analysis of the data gathered during the first full-scale floating installation of a wind turbine tower. With a set of tailored motion tracking units being develop for this purpose. The results show that most of the wave induced motions were caused originated from wave loading, and that the presence of a passive tugger line caused vortex induced vibrations. Since a simultaneous scaling of wind and waves at model scale is not possible, the data set here presented provides a unique understanding of the dynamics of this type of operation. This chapter is based on the following publications [41, 40].

Finally, **Chapter 4** addresses the challenge of motion compensation from a systems and control stand point. A novel scissored pair active control moment gyroscope is proposed together with a model-based framework for controller synthesis. The results highlight the challenge of mitigating tower induced motions and the importance of complementing active damping with disturbance rejection. As result, the yearly workability significantly increased, demonstrating the potential of control moment gyroscopes enhancing offshore operations. This chapter is based on the following publication [42].

Chapter 5 provides an overarching conclusion of this thesis alongside with recommendations for future research.

2

FREQUENCY-DOMAIN FRAMEWORK FOR FLOATING INSTALLATION OF WIND-TURBINE TOWERS

A tree without roots cannot live.
But a tree without new branches cannot grow.

-Stand High Patrol

As a result of more stable wind conditions and the depletion of near-shore locations, wind farms are moving farther offshore into deeper waters, challenging the current limits of offshore heavy-lift operations. This paper presents and verifies a novel frequency-domain framework to perform extensive site-specific analysis, of floating installations of wind-turbine towers, subjected to wind and wave loads. The versatility and potential of this framework is demonstrated with a case-study of a wind farm near the coast of Portugal. The results lead to the following conclusions: 1) Only considering beam-seas the yearly workability is 25 %; 2) The presence of wave induced motions significantly reduces workability for all cases; 3) Tower motions tend to decrease with tower size and are not significantly affected by hook-tower distance (sling length); and finally, 4) In this case-study the most contributing disturbance frequencies for tower motions are 0.3 and 0.4 rad/s, corresponding mainly to the first pendulation mode.

2.1. Introduction

Current environmental circumstances require an immediate step away from fossil fuels as main energy sources. Therefore, Europe aims at increasing the installed offshore wind power at least 25 times by 2030, compared to the total of 14.6 GW in 2021, [5]. As a result of more stable wind conditions and the depletion of near-shore locations, wind farms are moving farther offshore into deeper waters [94], challenging the current limits of offshore heavy-lift operations.

Initially motivated by the fossil fuel industry in the mid-1950s [93], offshore heavy-lift operations consist of handling large and heavy structures at sea. Given the exposure to weather conditions and the risk involved, safety is of primary importance. Because of the lack of data, the requirement of safety poses challenges when facing new, dynamic and exponentially growing markets, such as offshore wind [23].

Over time, the design of offshore crane vessels has converged to a semi-submersible crane-vessel (SSCV) type. Although semi-submersibles are known for being sensitive to hanging loads, in comparison to mono-hulls [88, 33], they provide flexible ballasting and enough deck area to accommodate two cranes of large capacity, outreach and lifting heights [33]. In contrast to this, in the offshore wind industry jack-up vessels have been dominating the scene due to higher stability. However, this increased stability comes at a price, which is: operational water depth limit (up to 80 meters [4]), dependency on seabed conditions, vulnerability to wind direction changes and jack-up time [27]. Limitations that floating vessels can overcome, as shown by Heerema Marine Contractors (HMC), Delft Offshore Turbine (DOT) and Delft University of Technology (TUDelft) with the *FOX* project [8]. However, ensure that no safety limits are exceeded during the installation of an Offshore Wind Turbine (OWT), it is crucial to have a good understanding of how wind and wave induced motions can be mitigated and how these affect workability, according to the following definition:

Workability represents the percentage of time for which a pre-defined operational limit is not exceeded during an installation time-frame.

The mitigation of load motions is an intrinsic challenge of heavy-lift operations. Some heavy-lift cranes feature heave compensation to control vertical motions by adjusting the cable length [86]. However, not every crane has this capability. To address this, Seaqualize has launched a series of semi-active heave compensators that are placed between the hook and the load [1]. For horizontal-plane motions, tugger-lines are the to-go choice, despite their limitations in the side-to-side direction. Tugger-winches with constant tension (CT) control [35] are the standard. This method mitigates snap loads, but does not reduce pendulation. In this regard, damping tuggers are a more promising concept [81, 64]. The field of tugger-line control is an active field of research, an example of this is the holistic approach presented in [63], where the interaction of tugger-line control and dynamic-positioning (DP) is studied, showing that actuator usage can be reduced by taking into account this interaction. However, the effect of improving this interaction on yearly workability was outside the scope of the article. In this regard, the approach presented in [32] addresses this by leveraging the properties of linear frequency-domain

methods, reducing the cost of workability calculations by a factor of 1000, which allowed to efficiently explore a larger design space and perform a manual sensitivity analysis of a motion compensated gangway. Given the sheer size of wind farms, every percent of extra downtime is quickly amplified by the large number of operations required, which increases the interest in tailored solutions. This is addressed in specific literature about floating installation of OWTs, most of it can be divided in three categories: installation of foundations [85, 109]; blade installation [95, 58, 96, 97, 51]; and new concepts of vessels and installation methods [72, 55, 54]. With a relevant example of research in this field being the work presented in [20], where a cost, system dynamics and loads analysis are presented for novel single-lift installation method. This installation method consists of using two cranes simultaneously with a lifting-frame that holds the fully assembled wind turbine by the tower. This research concluded that: 1) The installation of pre-assembled wind-turbines is economically feasible for wind-farms over 1500 MW; 2) Waves can cause guidance pins stabbing outside the buckets; and 3) Using 2-minute wave forecasts can drastically reduce the installation time. However, there are still operational challenges to be overcome, such as: ensuring tower integrity, limitations in crane height capacity, difficult use of heave-compensation, and the need of feeder barges to transport assembled OWT or to facilitate their assembling on-site. From a more scientific perspective, the main limitations of this work lie in the fact that wind loads are neglected and the results are not reproducible, due to intellectual property protection.

Currently, literature lacks information about the workability and dynamics of floating installation of OWT towers, leaving unanswered questions, such as: How should floating installation of wind turbine towers be modeled and how can it benefit from motion compensation? This work aims at making a step towards answering to these questions by developing a mathematical framework that it is used to: Assess yearly workability based on site-specific weather data for head and beam waves; Perform a Sensitivity Analysis, using *Sobol's* global method [77], to characterize the impact of variations in system parameters on tower motions; And finally, to determine the frequency ranges where the operation is most vulnerable to environmental conditions by means of a Dynamic Error Budgeting analysis [56, 32].

To summarize, the main three contributions of this arcticle are: 1) The development and verification of an open-source frequency-domain framework for floating installation of OWT towers; 2) Assessing the workability of this type of operation based on site-specific weather records; and 3) Providing a better understanding of the effect of wind, waves and system's parameters, on tower motions. Complementary to this, a reference open-source SSCV design is presented, with the intention of stimulating open-research.

This chapter is structured in the following way. In *Section* 2.2 the structure and derivation of the frequency-domain framework is presented. This is followed by the introduction of a case-study in *Section* 2.3, allowing the verification of the framework in *Section* 2.4. In *Section* 2.5 the results of workability, sensitivity and error budgeting analyses are presented and discussed, in the context of the case-study earlier defined, showing the framework's versatility and potential. This finally leads to the conclusions, in

Section 2.6.

2.2. MATHEMATICAL FRAMEWORK

This section presents a frequency-domain framework for floating installation of OWT towers, subjected to stochastic disturbances from wind and waves. The goal is to assess site-specific workability based on weather records and operational limits. *Figure* 2.1 displays the structure of the framework.
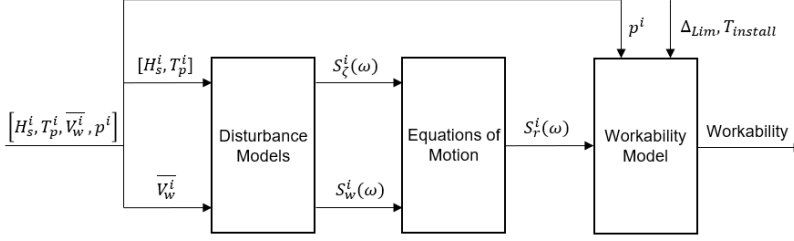

Figure 2.1: Framework overview.

As it can be seen, the inputs are: significant wave height (H_s in m); wave peak-period (T_p in s); mean wind speed ($\overline{V_w}$ in m/s); the probability of occurrence (p) of a combination i; the installation tolerance (Δ_{Lim} in m) and the installation time ($T_{install}$ in s). The "Disturbance Models" block is responsible for converting the environmental data into wave and wind power spectral density (PSD), $S_\zeta(\omega)$ and $S_w(\omega)$ in m^2.s and m^2/s, respectively. From here, using the equations of motion of the system, it is possible to determine the response PSD $S_r(\omega)$, in m^{2}s. Once $S_r(\omega)$ is known, the statistical properties of PSD are used to determine the percentage of time for which the operation can be safely executed, *i.e.:* workability. The following subsections describe in detail each module of the framework.

2.2.1. DISTURBANCE MODELS

Wind and waves are stochastic in nature, due to turbulence and the superposition of a large amount of wave components, which excites the system in an undesired way, reducing workability. In the context of this work, both wind and waves assumed unidirectional. Wind turbulence is modeled using the *Kaimal* PSD [75, 22], given by:

$$S_w(\omega) = \sigma_u^2 \frac{4L_{1u}}{\overline{V_w}(1 + 6\omega L_{1u}/(2\pi\overline{V_w}))^{5/3}} \qquad , \qquad (2.1)$$

in which $\overline{V_w}$ represents the mean wind speed in m/s, σ_u is the standard deviation of wind speed ($\approx 0.15 \cdot \overline{V_w}$) and L_{1u} is a turbulence length scale in meters (≈ 175 m) [22]. Note that in the context of this framework, $\overline{V_w}$ represents the mean wind speed at the tower center of gravity.

Irregular waves are modeled using the JONSWAP PSD [60], which is described by the following expression:

$$S_\zeta(\omega) = \frac{320 H_s{}^2 \cdot \omega^{-5}}{T_p{}^4} \cdot e^{\frac{-1950\omega^{-4}}{T_p{}^4}} \cdot \gamma^A \qquad , \qquad (2.2)$$

where γ is the peakness factor (often assumed to be 3.3), A is an exponential function of the peak-period T_p, and σ a step function which assumes different values for the range of frequencies below and above the peak frequency. More details can be found in [60].

The first block in the framework consists of these two spectra. In the coming section, a mathematical model is derived which allows correlation of output disturbances PSD with tower motions.

2.2.2. EQUATIONS OF MOTION

Reduced-order models describe systems working within a narrow operational range such that the governing physical laws can be approximated to their local solutions. Their simplicity and reduced computational cost allow to explore wider design spaces and provide a more clear perspective on the role of specific physical phenomena on the system behaviour. An example of this, is the work presented in [26], where a reduced order model is used to provide a better understanding of the fluid-structure interaction between regular waves and a simple pendulum.

To derive a reduced-order model it is necessary to define frames of reference and parameterize the system. Two frames or reference are adopted in this research, an inertial one ([X,Y,Z], earth-fixed) and an non-inertial one ([x',y',z'], ship-fixed), as shown in *Figure 2.2*, below.

The non-inertial frame of reference is located at the vessel's centre of gravity with the
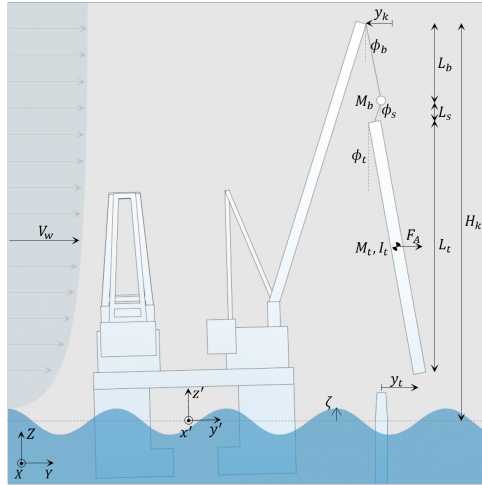

Figure 2.2: Diagram describing system parametrization.

x-axis pointing towards the bow, the y-axis pointing towards port-side and the z-axis perpendicular to the undistorted water surface, according to the right hand convention. The parameters shown in *Figure* 2.2 characterize the system. The sources of disturbances are: wind speed (V_w) and wave elevation (ζ). The disturbances to the system are: crane tip motion (y_k) and aerodynamic force (F_A). The variables that describe the states of the system are: off-lead angle (ϕ_b), sling angle (ϕ_s), tower angle (ϕ_t) and the distance between the tower bottom and foundation (y_t). And lastly, the properties of the system: hook block mass (M_b), tower mass and inertia (M_t, I_t), length of the hook block cable (L_b), sling (L_s) and tower (L_t), and finally, crane tip height (H_k). For simplicity, the system is modeled in 2D by assuming long-crested waves. Given this, the next step is to model the effect of disturbances on the system by deriving the governing equations.

WAVE INDUCED MOTIONS

The wave loads are composed of a mean-component, low-frequency component and a high frequency component [60]. In the context of this research, only the high-frequency component (first-order wave loads) are considered. The interaction of current and second-order low-frequency wave loads with the vessel's dynamic positioning (DP) system can induce slow varying motions on the vessel. Given their low frequency, these are not expected to significantly excite tower pendulation. Therefore, in this paper it is assumed that the DP system perfectly cancels these motions. It has been shown in the literature that there is a degree of interaction between the DP and pendulation control system [63], in future work it would be interesting to assess impact the DP performance on workability.

The wave induced motions are considered to be linear and frequency dependent [60]. They are described using response amplitude operators (RAOs). These can be obtained using potential-flow panel-methods [60], and map wave-amplitudes to steady-state ship motions, as follows:

$$RAO_r(\omega) = \frac{r_a(\omega)}{\zeta_a(\omega)} \Rightarrow \begin{cases} |RAO_r(\omega)| = \sqrt{RAO_r(\omega) \cdot RAO_r(\omega)^*} \\ \angle RAO_r(\omega) = arctan\left(\frac{Im\{RAO_r(\omega)\}}{Re\{RAO_r(\omega)\}}\right) \end{cases}, [r_a(\omega), \zeta_a(\omega)] \in \mathbb{C}, \quad (2.3)$$

where $r_a(\omega)$ and $\zeta_a(\omega)$ are complex numbers representing the system response and wave amplitudes in meters, respectively. The norm of $RAO_r(\omega)$ represents the amplitude of the relative response and the argument the phase angle, in radians. Note that $*$ represents the complex conjugate. Since turbine towers are likely to represent less than 1% of a SSCV's displacement, tower to vessel interactions are considered negligible, and therefore the use of RAOs in this context deemed valid [88, 33]. Given this, the vessel's response PSD is as follows [60]:

$$S_{\zeta, r(\omega)} = S_\zeta(\omega) \cdot |RAO_r(\omega)|^2 \quad , \tag{2.4}$$

in which $S_\zeta(\omega)$ is the wave energy spectra, as previously introduced.

WIND LOADS

In contrast to traditional heavy-lift installations, wind disturbances are believed to be important in the context of OWT installations, given the light weight of the components

and the fact that these installations take place in regions of high wind energy. In order to simplify the problem, it is assumed that the wind turbine tower is a perfect cylinder; the aerodynamic centre of pressure is located at the tower's centre of gravity (CoG); wind disturbance is caused by aerodynamic drag. Furthermore, it is also considered that vessel's wind-induced motions are much smaller and of much lower frequency than wave-induced motions. Therefore, not being expected to significantly contribute to OWT tower motions. A quantitative assessment of these motions is recommended for future work. Given this, the aerodynamic force, F_A in *Figure* 2.2, acting on the tower is described as follows [24]:

$$F_A = \frac{1}{2} \rho_{air} V_w^{r\,2} D_t L_t C_D \quad , \tag{2.5}$$

in which, ρ_{air} represents the air density in kg/m^3, V_w^r the relative wind speed in m/s, C_D the drag coefficient of a cylinder, and D_t and L_t the tower diameter and length in m. The expression for the relative wind speed is:

$$V_w^r = V_w - \dot{y}_{t,CoG} = \overline{V_w} + V_w' - \dot{y}_{t,CoG} \quad , \tag{2.6}$$

where $\dot{y}_{t,CoG}$ is the velocity of the tower's CoG in m/s and V_w is decomposed into a mean wind speed component $\overline{V_w}$ plus a wind speed fluctuation component V_w'. By substituting the previous equation into the aerodynamic force expression, *Equations* 2.5 and 2.6, the latter can be decomposed into an aerodynamic excitation component (F_A^{exc}) and damping component (F_A^{damp}), as follows:

$$F_A = \frac{1}{2} \rho_{air} (\overline{V_w} + V_w' - \dot{y}_{t,CoG})^2 D_t L_t C_D \Rightarrow$$

$$\Rightarrow \begin{cases} F_A^{exc} = \frac{1}{2} \rho_{air} D_t L_t C_D (\overline{V_w}^2 + 2\overline{V_w} V_w' + V_w'^2) \approx \rho_{air} D_t L_t C_D \overline{V_w} V_w' = E_A V_w' \\ F_A^{damp} = \frac{1}{2} \rho_{air} D_t L_t C_D (-2(\overline{V_w} + V_w') \dot{y}_{t,CoG} + \dot{y}_{t,CoG}^2) \\ \qquad \approx -\rho_{air} D_t L_t C_D \overline{V_w} \dot{y}_{t,CoG} = -b_A \dot{y}_{t,CoG} \end{cases} \tag{2.7}$$

where E_A and b_A are the aerodynamic excitation and damping coefficients, in Ns/m, both functions of mean-wind speed ($\overline{V_w}$). Disregarding smaller wind load contributions, results in a linearized form of the expression for aerodynamic loads. Furthermore, the static component arising from $\overline{V_w}^2$ are disregarded under the assumption that a static offset is compensated by the crane operator. Furthermore, the damping expression ensures system damping as far as the wind speed is non-zero. In the coming section the additional b_{sys} is introduced.

SYSTEM DYNAMIC MODEL
While previous sections modeled the environmental disturbances acting on the system, y_k and F_A, this section models the system response using the *Lagrange* method, presented as as follows:

$$\frac{\partial}{\partial t}\left(\frac{\partial T(q_i)}{\partial \dot{q}_i}\right) - \frac{\partial T(q_i)}{\partial q_i} + \frac{\partial R(q_i)}{\partial \dot{q}_i} + \frac{\partial U(q_i)}{\partial q_i} = Q_i \quad , \tag{2.8}$$

in which q_i represents an independent coordinate system of each degree of freedom, in this case: block angle ϕ_b, sling angle ϕ_s and tower angle ϕ_t, all in rad. $T(q_i)$, $U(q_i)$

and $R(q_i)$ are functions of q_i, representing the system's kinetic, potential and dissipative energies, in J. Q_i represents the external loading applied to each q_i. In order to determine these expressions, the system is simplified to a 2D, driven, tripe-pendulum with a distributed mass. Given this, the crane tip position, relative to the initial condition is:

$$\vec{p}_k = (y_k - y_k^0)\,\vec{j} + (z_k - z_k^0)\,\vec{k} \qquad , \tag{2.9}$$

in which y_k and z_k are the horizontal and vertical coordinates of the crane tip, in m. The superscript 0 represents undisturbed initial conditions. $\vec{j}$ and $\vec{k}$ are unit vectors in the Y and Z axis, respectively. From this, the block and tower position vectors, $\vec{p}_b$ and $\vec{p}_{t,CoG}$, are given by:

$$\begin{cases} \vec{p}_b = \vec{p}_k + L_b\left(sin\phi_b\,\vec{j} + (1-cos\phi_b)\,\vec{k}\right) \\ \vec{p}_{t,CoG} = \vec{p}_b + L_s\left(sin\phi_s\,\vec{j} + (1-cos\phi_s)\,\vec{k}\right) + \frac{L_t}{2}\left(sin\phi_t\,\vec{j} + (1-cos\phi_t)\,\vec{k}\right) \end{cases} \tag{2.10}$$

From here, analytical expressions can be derived for the potential $U(\phi_b, \phi_s, \phi_t)$, kinetic $T(\phi_b, \phi_s, \phi_t)$ and dissipative $R(\phi_b, \phi_s, \phi_t)$ energies of the system, as well as for the external loading Q_i:

$$\begin{cases} U(\phi_b, \phi_s, \phi_t) = g(M_b z_b + M_t z_t) \\ T(\phi_b, \phi_s, \phi_t) = \frac{1}{2}\left(M_b|\dot{\vec{p}}_b|^2 + M_t|\dot{\vec{p}}_{t,CoG}|^2 + I_t\dot{\phi}_t^2\right) \\ R(\phi_b, \phi_s, \phi_t) = \frac{1}{2}\left(b_A \dot{y}_{t,CoG}^2 + b_{sys}\dot{y}_b^2\right) \\ Q_b = L_b E_A V_w \\ Q_s = L_s E_A V_w \\ Q_t = \frac{L_t}{2} E_A V_w \end{cases} \tag{2.11}$$

where the subscripts b, s and t refer to the coordinates ϕ_b, ϕ_s and ϕ_t, see *Figure* 2.2. b_{sys} is an additional generic damping coefficient term, in Ns/m, which accounts for mechanical losses of the system (*e.g.*: sheaves and cables) aerodynamic damping at non-zero wind-speeds and energy dissipated by the vessel through water viscosity. Note that the dot on top of a vector is used to represent a time derivative, analogous to $\frac{\partial}{\partial t}$.

By combining the *Equations* 4.3 and 2.11, the dynamic model of the system is obtained. To ensure linearity, small angle approximation is adopted and the vertical motion of the crane tip neglected, as follows:

$$\begin{cases} z_k = \dot{z}_k = \ddot{z}_k \approx 0 \\ sin(\phi) \approx \phi \\ cos(\phi) \approx 1 \end{cases} \quad , \tag{2.12}$$

in which ϕ is representative of ϕ_b, ϕ_s and ϕ_t. Although neglecting crane tip vertical motion can affect the pendulation behaviour, it is not expected to significantly affect workability since side-to-side accelerations are expected to be much larger.

A common way to represent coupled ordinary differential equations is with state-space modeling. A variety of tools is implemented in common programming languages to manipulate, analyse and solve this type of system, making it convenient to use. In the coming section the equations of motion, here derived, are represented in this form.

STATE-SPACE MODEL

The general form of a state-space representation is:

$$\begin{cases} \dot{x} = Ax + Bu \\ y = Cx + Du \end{cases}, \tag{2.13}$$

where A is the dynamics matrix, B the input matrix, C output matrix and D the direct term matrix. x, u and y are the state, input and output vectors, which in the context of this problem are:

$$x = \begin{bmatrix} \dot{y}_k \\ y_k \\ \dot{\phi}_b \\ \phi_b \\ \dot{\phi}_s \\ \phi_s \\ \dot{\phi}_t \\ \phi_t \end{bmatrix}, u = \begin{bmatrix} \ddot{y}_k \\ V'_w \end{bmatrix}, y = \begin{bmatrix} y_k + L_b\phi_b + L_s\phi_s + L_t\phi_t \end{bmatrix}, \tag{2.14}$$

in which the inputs of the system are crane tip acceleration ($\ddot{y}_k$) and wind speed (V_w). The output is the tower bottom position, y_t. Since the latter requires a double integration of the crane tip acceleration signal, a second-order high-pass filter is added to mitigate numerical drift:

$$\begin{bmatrix} \ddot{y}_k \\ \dot{y}_k \end{bmatrix} = \begin{bmatrix} -2\zeta_f\omega_c & -\omega_c^2 \\ 1 & 0 \end{bmatrix} \begin{bmatrix} \dot{y}_k \\ y_k \end{bmatrix} + \begin{bmatrix} 1 \\ 0 \end{bmatrix} \begin{bmatrix} \ddot{y}_k \end{bmatrix}, \tag{2.15}$$

where ζ_f it is the damping ratio of the filter and ω_c the cut-off frequency, in rad/s.

Conventionally, the A, B, C and D matrices have constant values. However, both the aerodynamic excitation $E_A(\overline{V_w})$ and damping $b_A(\overline{V_w})$ coefficients are functions of the mean wind speed $\overline{V_w}$, as shown in *Equation* 2.7, meaning that matrix A and B are functions of $\overline{V_w}$.

FREQUENCY RESPONSE

The state-space model can be converted to the frequency-domain using the *Laplace* transform [59]. With s being the complex frequency-domain parameter, the system can be described by the following two transfer functions:

$$\begin{cases} G_{\zeta,r}(s) = \frac{R(s)}{Z(s)} \\ G_{w,r}(s) = \frac{R(s)}{V'_w(s)} \end{cases}, \tag{2.16}$$

in which $R(s)$ represents the system response (tower bottom motion), $Z(s)$ the wave elevation and $V'_w(s)$ the time varying component of wind speed, all in the *Laplace* space.

Analogously to *Equation* 2.4, the responses PSD of the system, $S_{\zeta,r}(\omega)$ and $S_{w,r}(\omega)$, are given by:

$$\begin{cases} S_{\zeta,r}(\omega) = S_{\zeta}(\omega) \cdot |G_{\zeta,r}(i\omega)|^2 \\ S_{w,r}(\omega) = S_w(\omega) \cdot |G_{w,r}(i\omega)|^2 \end{cases} \quad , \tag{2.17}$$

where the normal $|G_{\zeta,r}(i\omega)|$ and $|G_{w,r}(i\omega)|$ are gain spectra of the respective transfer functions [59]. Given the stochastic nature of wave and wind induced motions, the phase angle ϵ of the spectrum is described by a uniform probabilistic distribution in the range of $[0, 2\pi]$ rad/s, [60]. Thus, the response PSD $S_r(\omega)$ of the system, subjected to wind and waves, is given by:

$$S_r(\omega) = S_{\zeta,r}(\omega)e^{i\epsilon_{\zeta}} + S_{w,r}(\omega)e^{i\epsilon_w} \tag{2.18}$$

This step completes the equations of motion block in *Figure* 2.1. In the coming section, the last block of the framework is described, concerning the workability model.

2.2.3. WORKABILITY MODEL

For the successful installation of a wind-turbine tower, it is necessary to ensure that no operational safety limits are exceeded. The goal of the workability model derived in this section is to rapidly assess whether or not an installation can be completed, based on site-specific environmental conditions. For this the following definition of workability is adopted:

Workability (W) represents the percentage of time for which a pre-defined operational limit (Δ_{lim}) is not exceeded during the installation time-frame ($T_{install}$).

This can be assessed by making use of the statistical properties of the response PSD of the system, $S_r(\omega)$. According to [60], the amount of times (N_{exc}) that an operation limit (Δ_{lim}) is expected to be exceeded during the installation time ($T_{install}$) is given by:

$$N_{exc} = \frac{T_{install}}{T_{2r}} \cdot P\{r > \Delta_{lim}\} \quad , \tag{2.19}$$

where T_{2r} denotes the average zero-crossing period of the system response, and $P\{r > \Delta_{lim}\}$ the probability of the response exceeding the operational limit Δ_{lim}, with the former being given by:

$$T_{2r} = 2\pi \cdot \sqrt{\frac{m_{0r}}{m_{2r}}} \quad , \tag{2.20}$$

in which m_{nr} denotes the nth order moment of $S_r(\omega)$:

$$m_{nr} = \int_0^{\infty} \omega^n \cdot S_r(\omega) d\omega \quad , \tag{2.21}$$

According to [60], $S_r(\omega)$ can be assumed narrow banded. In this case the cumulative probability function of the system response is approximated by a *Rayleigh* distribution:

$$P\{r > \Delta_{lim}\} = e^{\frac{-\Delta_{lim}^2}{2m_{0r}}} \quad . \tag{2.22}$$

From the workability definition we find that a condition is workable if the expected number of times that an operational limit is exceeded is lower than 1, *i.e.:* $N_{exc} < 1$. This results in a binary condition: workable or not workable. Using the probability of occurrence p^i of an environmental condition i, it is then possible to compute workability W, as follows:

$$W = \sum_{i=1}^{N} p^i \cdot \delta(N_{exc}^i) \quad , \tag{2.23}$$

in which N represents all the existing combinations of sea-states, p^i the respective probability of occurrence and $\delta(N_{exc}^i)$ a Dirac function:

$$\delta(N_{exc}^i) = \begin{cases} 1 & , N_{exc}^i < 1 \\ 0 & , N_{exc}^i \geq 1 \end{cases} \tag{2.24}$$

2.3. CASE-STUDY

Research about floating installation of OWTs has been increasing in recent years, as jack-up vessels start not to suffice the demands of the market. However, intellectual property regulations of offshore companies are strict, which often limits open-research in this field. To overcome this, in this section a case-study is presented, in which an open-source semi-submersible crane-vessel (SSCV) is performing the installation of DTU 10 MW wind turbine towers near the Portuguese coast. This case focuses on the final tower installation stage, in which the bottom end of the tower is suspended 3 meters above the foundation waiting for a weather window for the set-down. Below, *Figure* 2.3 shows the open-source crane-vessel, which we name SSCV Prometheus.
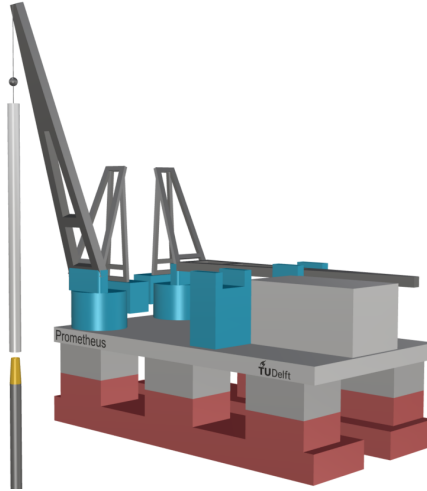

Figure 2.3: Prometheus, an open-source SSCV [44].

Prometheus is a 160 m semi-submersible crane-vessel, representative of existing ones of its kind. For the sake of results reproduction, its design consists of straight lines. Table 2.1 describes the main characteristics.

Table 2.1: Prometheus' characteristics [44].

Description	Notation	Value	Unit
Length Overall	LOA	160	m
Beam	B	90	m
Draft	D	25	m
Submerged Volume	∇	196250	m^3
Transverse Metacentric Radius	BM$_t$	25.4	m
Longitudinal Metacentric Radius	BM$_l$	56.8	m

The 3D geometry, as well as response amplitude operators and hydrostatic data are publicly available [44]. The vessel and crane are considered as one rigid body. In this case-study two operational conditions are considered: 1) Head wave, installing the tower over the bow, the vessel is free to surge and pitch; 2) In beam waves installing the tower over star-board, in which it sways and rolls.

The wind-turbine tower is inspired by the *DTU 10 MW* reference wind turbine, [18]. It is 115 m tall, with a diameter of 5.5 m and a weight of 600 ton. The location of the installation is inspired by a recent tender for 10 GW of offshore wind energy to be installed before 2030 in Portugal [6]. One of the designated areas, Figueira da Foz wind park, *Figure* 2.4, is planned to have an installed capacity of 4 GW. Located at an average water-depth of over 100 meters, as shown in *Figure* 2.4 below, this wind park is beyond the depth-limits of any currently existing jack-up vessel [4]. The great exposure to Atlantic swell, makes the Figueira da Foz wind park a relevant case-study for floating installation of OWTs.

The operational limits here considered are: installation tolerance (*i.e.:* the allowable mis-
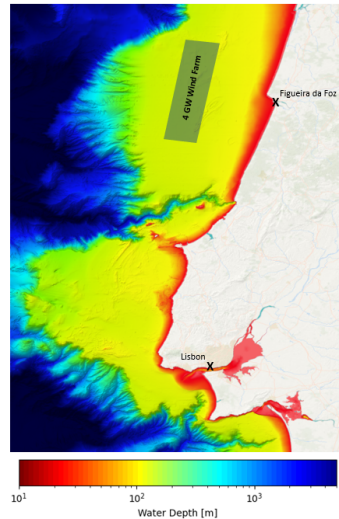

Figure 2.4: Location of Figueira da Foz wind farm [83] and bathymetric map [3].

alignment between the tower and the foundation) and the maximum off-lead angle (ϕ_b),

a mechanical limitation of the crane. Regarding the installation time-frame ($T_{install}$), [20] considers 65 seconds. This accounts for set-down time, thinking time and mechanical system delays. However, this value does not include monitoring time and buffer time in case any of any extra delay. Thus, 120 seconds is considered to be a more realistic time interval to ensure a safe operation.

Site-specific weather data is obtained from satellite measurements, publicly available in [2]. These records consist of 30 years of hourly measurements of sea-states and average wind speeds, between the years of 1990 and 2019. The wind-speeds are interpolated to the vertical position of the tower's CoG using a boundary-layer power-law [66].

All the relevant parameters describing this case-study are to be found in *Table* 2.2. The coming section uses this case study to validate the framework previously presented, against a high-fidelity model.

Table 2.2: Case-study parameters.

Description	Notation	Value	Unit
Crane tip height	H_k	176	m
Block cable length	L_b	35	m
Sling length	L_s	10	m
Tower height	L_t	115	m
Tower diameter	D_t	5.5	m
Hook block mass	M_b	50×10^3	kg
Tower mass	M_t	600×10^3	kg
Tower moment of Inertia	I_t	66.125×10^7	kgm^2
Installation tolerance	$\Delta_{lim}^{y_t}$	1.5	m
Off-lead angle limit	$\Delta_{lim}^{\phi_b}$	3	deg
Installation time-frame	$T_{install}$	120	s
Sea-water density	ρ_w	1025	kg/m^3
Air density	ρ_{air}	1.293	kg/m^3
Tower drag coefficient	C_D	0.65	-
Additional system damping	b_{sys}	17	kNs/m
Installation site coordinates	N-E	40.25-9.5	deg

2.4. Verification of Wave Induced Motions

Model verification is an essential step in the development process of a mathematical model. Inspired by [73], this section makes a direct comparison between a *WEC-Sim* model and the mathematical model previously presented in this paper. The case-study introduced in the previous section is used for the verification of wave induced motions. In future research it is recommended to verify wind induced motions recurring to CFD, for more accurate aerodynamic force estimations.

2.4.1. Hydrodynamic Calculations

WEC-Sim is a open-source, multibody, non-linear, time-domain solver for floating bodies [90, 73]. The hydrodynamic data required by *WEC-Sim* to determine wave loads is computed, in this paper, using the diffraction code *Capytaine* [12, 17]. From this hydrodynamic data, crane tip acceleration RAOs are also computed, which are used by the framework, under the assumption of negligible tower to vessel interaction

Figure 2.5 shows the mesh for the diffraction calculations. It is composed of 2D quadrangles, with a reference size of 2 meters, fulfilling *Capytaine's* recommendations: maximum element size needs to be smaller than $\lambda(\omega_{max})/8$, where $\lambda(\omega_{max})$ represents the shortest wave length of interest. This mesh was obtained using the open-source meshing software *Salome* [7]. For the *Capytaine* calculations, the wave frequency range varies according to the range $\omega = [10^{-2}; 2]$ rad/s in steps of 10^{-2} rad/s.
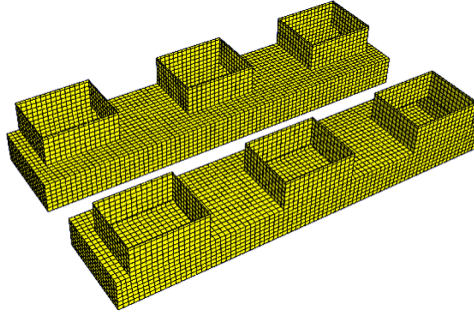

Figure 2.5: Prometheus SSCV mesh for BEM calculations.

In the present case, the distance from the top of the floaters to the free-surface is of 12.5 m. Numerical instabilities of the BEM code were observed for shallower drafts, when this distance becomes 10 m or less. It is caused by the presence of panels with normals pointing towards the free-surface [61]. The hydrodynamic characteristics of Prometheus can be also found in [44], as well as geometry and other relevant information such as mass, draft, moments of inertia, among others. The crane tip acceleration is as follows:

$$RAO_{\ddot{y}_k}\vec{j} = -\omega^2\left(RAO_{sway}\vec{j} + H_k\vec{k} \times RAO_{roll}\vec{i}\right) \quad , \tag{2.25}$$

in which H_k is the crane tip height (*Table* 2.2), RAO_{sway} the response amplitude operator in sway and RAO_{roll} in roll. Note that $[\vec{i}, \vec{j}, \vec{k}]$ are unit vectors representing the axis $[X, Y, Z]$ of the earth fixed frame of reference, respectively.

2.4.2. VERIFICATION RESULTS

The *WEC-Sim* simulator setup is shown in *Figure* 2.6.
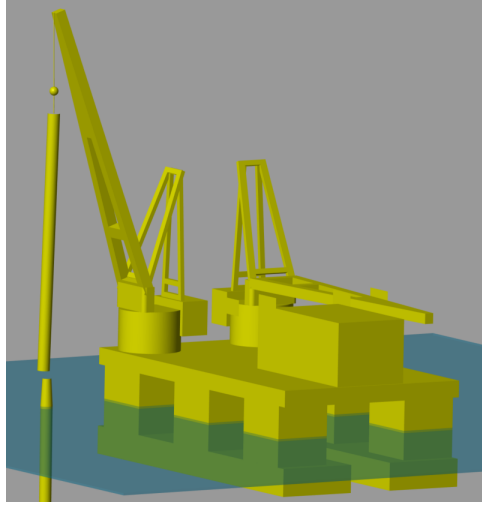

Figure 2.6: *WEC-Sim* setup for the verification.

A beam-sea characterized by a *JONSWAP* spectrum with 8 seconds peak-period (T_p) and 3 meters significant wave height (H_s) is chosen as a representative limiting condition. Given the stochastic nature of the disturbances and the relevance of the statistical properties of the system's response spectra in the context of this work, cumulative standard deviation, $c\sigma(\omega_n)$, is chosen as a verification criterion:

$$c\sigma(\omega_n) = \sqrt{m_0(\omega_n)} = \sqrt{\int_0^{\omega_n} S_r(\omega)\,d\omega}, \tag{2.26}$$

where ω_n represents a discrete frequency n, in rad/s. This criterion provides detailed information about the contribution of each frequency to the total standard deviation. To obtain the tower-bottom motion PSD from WEC-Sim, the time trace is first converted into an amplitude spectrum $y_t(\omega_n)$ using Fast Fourier Transform (FFT) and then normalized by the discretization frequency $\Delta\omega$ in the following manner [60]:

$$S_r(\omega_n) = \frac{y_t^2(\omega_n)}{2\Delta\omega}, \tag{2.27}$$

Figure 2.7 shows good agreement between the WEC-Sim model and the framework model in terms if the cumulative standard deviation. While the framework's mathematical model over-estimates the response amplitude by 2 %, it perfectly predicts the main contributing frequencies to the standard deviation. The 2% difference between the framework model and *WEC-Sim* is thought to originate from tower to vessel interaction. The difference is small enough to consider the framework verified.
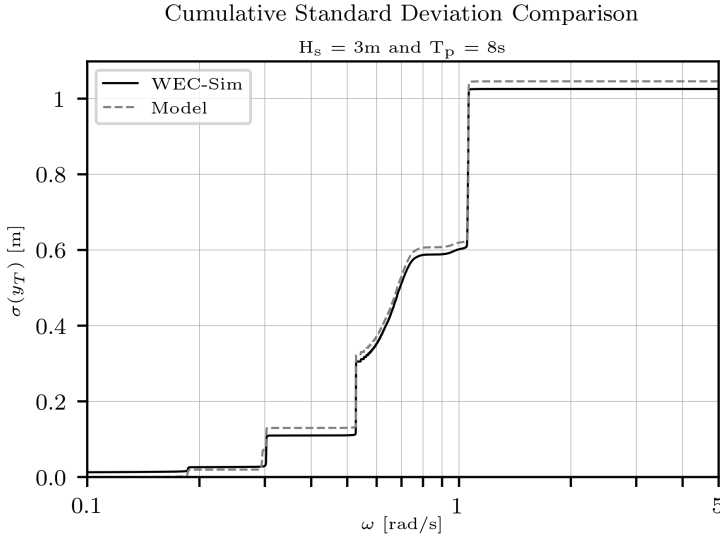
Cumulative Standard Deviation Comparison

Figure 2.7: Comparison of cumulative standard deviation of tower horizontal bottom motions between the framework's model and a WEC-Sim model.

2.5. RESULTS AND DISCUSSION

This section aims at providing a better understanding of the floating installation of OWT towers, by answering to a number of questions that literature has not answered yet, such as: What is the expected yearly workability? Is head-seas the most favourable condition? What are the most important system parameters? Are waves the main source of disturbance?

This type of insight is important for the improvement of floating offshore operations. Therefore, this section applies the framework presented in this paper to the case-study defined in *Section* 2.3. It answers the previous questions, while demonstrating the versatility and potential of the framework.

2.5.1. WORKABILITY

In *Figure* 4.11, the workability of this operation is assessed and compared for beam and head waves, on the monthly basis.

The gray bars represent the workability if only assessed considering wind, therefore, independent from wave direction. The blue bar represents workability when only considering wave induced motions. Finally, the dark blue dots connected by a dashed line, represent the total workability, *i.e.* the workability considering wind and waves. As can be expected, the summer period is the one with higher workability (30-40 %), in contrast to winter. In contrast to beam seas where the workability is mainly limited by wind induced motions, in head-seas the workability is limited by waves. Nevertheless, the total workability is significantly lower than when considering wind alone, with waves reducing the yearly workability by over 20 percentage points. This not only stresses the importance of considering wind and waves simultaneously, but also the potential role

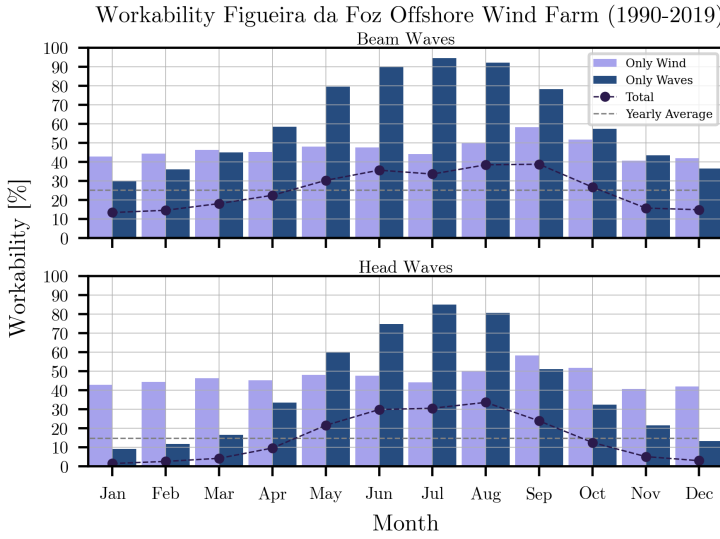Workability Figueira da Foz Offshore Wind Farm (1990-2019)

Figure 2.8: Workability at Figueira da Foz offshore wind farm in beam and head seas.

of motion compensation systems in enhancing the workability of floating installation of wind turbine towers. Lastly, the most limiting wave direction is head-seas, with an average yearly workability of 15% compared to the 25% in beam-seas. This difference is explained by the higher hydrostatic stiffness in pitch than in roll, leading to larger crane-tip accelerations. During the simulations it was also possible to observe that a 3 degrees off-lead angle limit is seldomly reached.

2.5.2. SENSITIVITY ANALYSIS

A sensitivity analysis is a type of analysis that characterizes the impact of variations in system parameters on the output. This information provides a better understanding of a system's behaviour, which is useful from the operational point of view, as well as from the modelling point of view. It allows for quantification of model uncertainties, and identifies unnecessary parameters in an informed way. Most of the approaches for sensitivity analysis can be split in three groups: Sample-based methods, Linearization methods and Global methods [77]. In the context of this research a global method is adopted via *Sobol's Sensitivity*. This method performs an evaluation of the model at different working points by means of a Monte-Carlo simulation. Then the variance of the model output is related to the variance of each parameter [80], being the reason why this method is also known as *ANOVA* (ANalisys Of VAriance). There are first-order *Sobol's* indices and higher-order ones. While the first-order ones assess the impact of varying individual parameters, higher-order indices assess the impact of varying combinations of parameters. Despite the fact that the computational cost increases linearly with the order of the indices [77], in the context of this research, the added value of considering higher-order *Sobol* indices is not considered significant, and therefore neglected. The sensitivity analysis is performed with the open-source software *UQLab* [78].

The system sensitivity to parameter variations is assessed based on the tower bottom's motion standard deviation (σ). The environmental conditions are: 8 seconds peak-period (T_p), 3 meters significant wave height (H_s) and 10 meters per second average wind speed ($\overline{V_w}$). In order to ensure physically meaningful sets of parameters, the system is reduced to 3 independent variables: sling length (L_s), tower length (L_t) and hook block mass (M_b). *Table* 2.3 contains the intervals for which each parameter was varied, using a uniform probabilistic distribution. According to dimensional analysis, the remaining variables are

Table 2.3: Parameter's variation intervals for sensitivity analysis.

Description	Notation	Interval	Unit
Sling length	L_s	[2.5; 17.5]	m
Tower height	L_t	[90; 140]	m
Hook block mass	M_b	[25; 75] $\times 10^3$	kg

functions of tower length (L_t):

$$\begin{cases} L_b = h_{k0} - L_s - L_t - \Delta z_0 \\ D_t = D_{t0}\left(\frac{L_t}{L_{t0}}\right) \sim L_t \\ M_t = M_{t0}\left(\frac{L_t}{L_{t0}}\right)^3 \sim L_t^3 \\ I_t = \frac{1}{12} M_t L_t^2 \sim L_t^5 \end{cases}, \tag{2.28}$$

where Δz is the 3 m clearance between the tower bottom and the foundation, and the subscript 0 refers to the reference values defined in *Table* 2.2. The crane tip height (H_k) is kept constant to ensure the same operational setting between simulations. The *Sobol's* sensitivity indices shown in *Figure* 2.9, below, are computed from a sample of 1250 Monte Carlo simulations.

According to these results, tower length (L_t) is the parameter that affects tower bottom motions the most, by a large margin, independently from wave direction. Hook block mass (M_b) is the second most relevant parameter, especially in beam waves, since it affects the stiffness of the second pendulation mode. However, not as much as tower size, since $M_t \sim L_t^3$. The least important parameter is sling length (L_s), showing a very limited influence on the results. This is explained by the fact that the sling length is only relevant for the third pendulation mode, which occurs at frequencies above 2 rad/s, near which the wave spectrum has minimal energy content. This result is particularly interesting, since it indicates that the degree of freedom ϕ_b might be superfluous. It is expected that neglecting it can reduce the computational cost of the model and its derivation by over 50 % (assuming Gaussian elimination), while having a limited impact on the relevance of the results.

Although *Sobol* sensitivity provides useful information about how much variations in the system's parameters can affect the output, it does not provide information about in which way the response is affected. In order to assess this, the 3D surface plot of *Figure* 2.10 shows, for the case of beam waves, the explored design space, neglecting the variation
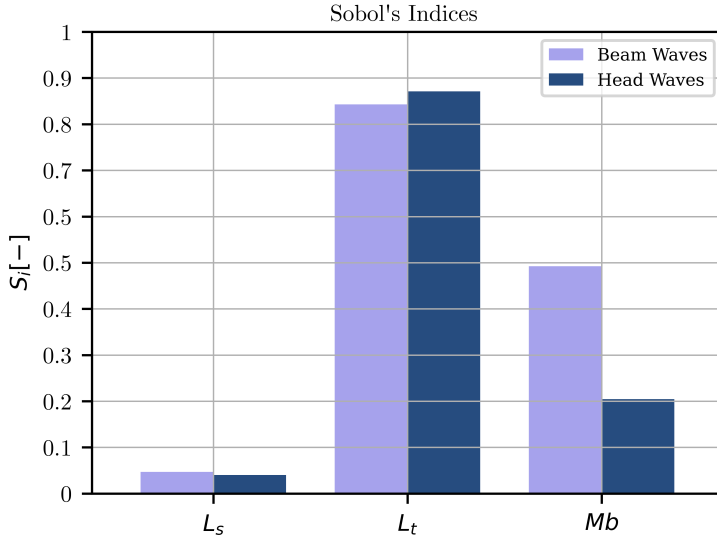
Figure 2.9: *Sobol's* sensitivity indices.

sling length. The black dots are the data points from the *Monte Carlo*. The 3D surface is the result of a linear interpolation between *Monte Carlo* data points. Looking at this data, it is possible to identify clear trends. Tower bottom motions increase with block weight (M_b) and decrease with tower length (L_t). Following the same reasoning as before, increasing block mass decreases the natural frequency of the second pendulation mode, bringing it closer to wave excitation frequencies. While increasing tower size increases the natural frequency of the second pendulation mode (away from wave excitation) as well as making the system more resilient to wind gusts. The scaling law for tower weight (*Equation* 2.28) also explains why for larger towers the effect of varying block mass is of less importance than for smaller towers. It is not intuitive that when these results are extrapolated to workability, that workability increases with tower size. To confirm this hypothesis a similar study must be conducted assessing workability. However, it is important to ensure that tower to vessel interactions remain irrelevant for larger tower sizes, according to the current assumptions of the framework.

2.5.3. DISTURBANCE ANALYSIS

Although the analysis provide a picture of the system limitations and behaviour, they do not provide information about what frequencies are limiting workability the most. In this section, this is assessed using *Dynamic Error Budgeting* (DEB) [56, 32], a method born in the field of precision engineering, that uses the concept of cumulative standard deviation (introduced in *Section* 2.4) to assess the effects of stochastic disturbances on a system's response. In this context, DEB provides in-depth knowledge that is crucial to explore means to improve workability.

In order to draw meaningful conclusions about the effect of environmental distur-
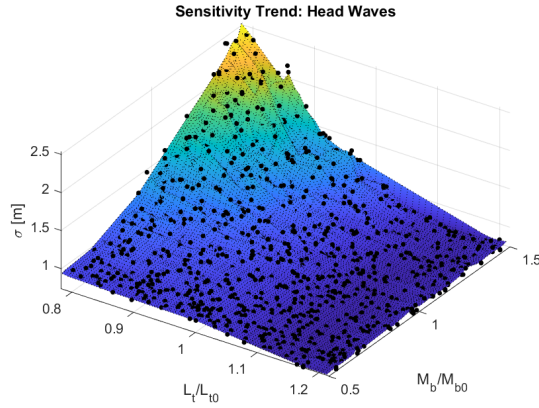
Figure 2.10: Surface plot showing the effects of varying tower length (L_t) and hook block mass (M_b) on the standard deviation (σ) of the tower bottom position.

bances on the system response, all the possible weather combinations are taken into account. This results in the error budgeting clouds shown in *Figure* 2.11, providing an indication of how the standard deviation of tower bottom motion builds-up over frequency. Please note that the opacity represents the probability of occurrence and the larger the gradient, the larger the contribution of the respective frequencies to wind turbine bottom motions.

The plots on the left column, in *Figure* 2.11, refer to beam seas and the ones on the right to head seas. The first row shows error budgeting clouds for wind disturbances, since these ones do not depend on wave direction, both plots are analogous. The second row shows the contribution of wave induced motions to standard deviation. The bottom row refers to the motions caused by wind and waves simultaneously. The fading of the error budgeting clouds represents the probability of occurrence of each environmental condition. The dashed lines represent the weighted average of the clouds. From these results it is possible to immediately notice a difference in the scale of the vertical axis between beam and head waves. This is caused by significantly higher values of standard deviation in tower bottom motions in head seas, with sea-states causing standard deviations of over 20 meters. As earlier explained, this is caused by the higher hydrostatic stiffness in pitch direction. However, these values challenge the model's linearity assumption. Nevertheless, it is an indication that head waves are not favorable for the operation, which is in line with the workability results shown earlier. Regarding wind induced motions, the most contributing frequency is 0.3 rad/s, with maximum weighted average of 1.2 m. In beam waves, the wave contributions occur in two intervals: a narrow one close to 0.3 rad/s (same as wind induced motions); and a broad one ranging from 0.5 to 0.7 rad/s, containing the larger portion of the contributions. Furthermore, standard deviation weighted average converges to 0.7 m. In head waves, most of the wave contributions are concentrated at 0.4 rad/s and with a standard deviation weighted average of 2.9 m. When considering wind and waves simultaneously, it it is possible to see that for the beam waves case most of the contributions are concentrated at 0.3 rad/s while for head waves
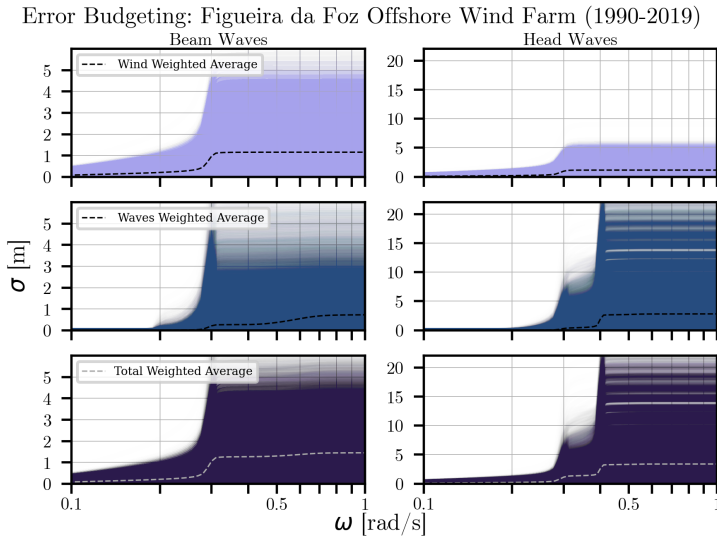
Figure 2.11: Error budgeting for all the recorded combinations of weather conditions from 1990 to 2019, for beam and head seas.

at 0.3 and 0.4 rad/s, with the weighted averages converging to 1.45 and 3.4 m, respectively. Overall the most contributing frequencies to tower motion are located in the range of 0.2 to 0.7 rad/s, with the main peaks at 0.3 and 0.4 rad/s. Wind acts on the lower range of this spectrum. Furthermore, these results back-up the workability analysis, where it is concluded that wave-induced motions are more limiting in head-seas than in beam-seas. Regarding the latter, it has been shown in literature that accounting for wave directional spreading can affect the performance of installation vessels [27], given that it induces 3D motions on the ship and load. This should be addressed in future research.

Although these results show which frequencies contribute the most to tower motions, they do not explain which pendulation modes are being excited the most. For this purpose, *Figure* 2.12 shows the Frequency Response Function (FRF) of the system: According to this FRF, is is possible to conclude that the main pendulation mode is the first one. The natural frequency of the third pendulation mode occurs at around 4.5 rad/s, explaining its small relevance. It is also interesting to note the presence of anti-resonant dips from wind excitation to tower bottom motions, meaning that at these frequencies minimal tower bottom displacements are expected, in contrast to the resonance peaks.
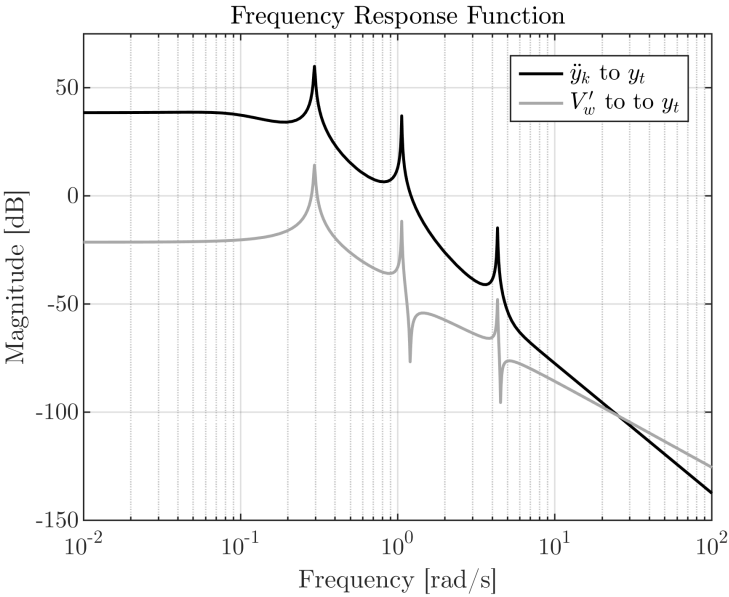
Figure 2.12: Crane tip acceleration amplitude spectra and tower bottom position response to crane tip accelerations.

2.6. Conclusions

In recent years attention has shifted to floating installation of OWT. This installation method overcomes some of the current limitations of jack-up vessels and allows conventional offshore heavy-lift contractors to enter the wind market. With the goal of creating a better understanding of this type of operations, this paper presents and open-source framework for floating installation of OWT towers and applies it to a case-study. A by-product of this work is the novel open-source crane-vessel, aimed at promoting open-research in this field [44].

The framework is successfully verified using WEC-Sim. The results show a 2% overestimation of the system response to the first pendulation mode, while the main contributing disturbance frequencies are predicted with no error. These results justify the use of a linear model with no tower to vessel interaction. The versatility of the framework is demonstrated by means of the case study in which the installation of a DTU 10 MW wind turbine tower on the Portuguese coast is analysed. Based on on-site records from 1990 to 2019, the results show that the workability in beam-waves is higher than in head-waves, with an yearly value of 25%. The overall difference in workability between beam and head-waves comes from the higher hydrostatic stiffness in pitch, resulting in larger crane-tip accelerations. Nevertheless, in both cases, wave induced motions are shown to significantly reduce the total workability. This not only stresses the importance of considering wind and waves simultaneously, but also the potential role of motion compensation systems in enhancing the workability of floating installation of wind turbine towers. In order to better understand the influence of the system's parameters on tower motions, a sensitivity analysis based 1250 Monte Carlo simulations was performed. The results show that larger towers tend to reduce motions, which is explained by the reduction of the second pendulation mode. In contrast to this, tower motions tend to increase with block mass, since it reduces the natural frequency of the second pendulation mode, making it more vulnerable to environmental disturbances. Variations in this parameter do not affect motions as much as tower size, given that tower mass scales with L_t^3. Also the same analysis points in the direction that sling angle (ϕ_s) is a superfluous degree of freedom, which increases the computational cost of the model by over 50% while having very limited influence on tower motions. The third pendulation mode frequency is too high to be significantly excited in this case study.

While workability and sensitivity analyses provide a picture of the system's limitations and behaviour, an error budgeting analyses provides information about the most relevant frequencies exciting the system. Error budgeting clouds are computed for all the combinations of significant wave height, peak-period and mean wind speed, taking into account their probability of occurrence. Showing that, for this case-study, the main contributing frequencies for tower motions occur at 0.3 and 0.4 rad/s, with wind acting at the lower range of this spectrum.

This work contributes to existing literature by providing a better understanding of the susceptibility of floating installation of OWT towers to environmental conditions, in the context of an open-source case-study and framework.

2

2.7. ACKNOWLEDGEMENTS

3

FULL-SCALE MEASUREMENTS AND ANALYSIS OF THE FLOATING INSTALLATION OF AN OFFSHORE WIND TURBINE TOWER

"Until man learns to respect and speak to the natural world, he can never truly understand his place on this earth."

-Enzo Maiorca

Europe has set an ambitious target to increase the offshore wind power capacity to approximately 30 GW by 2026. With nearshore locations already allocated, future wind farms must be installed in deeper waters, pushing the operational limits of currently used jack-up vessels. Utilizing existing floating heavy-lift vessels presents a viable alternative. This paper disseminates data gathered during the full-scale testing campaign of a floating installation of an offshore wind turbine tower. For this purpose, novel time-synchronized motion-tracking units were developed. Analysis of the obtained data reveals that approximately 96% of the motion response of the tower is due to wave action and 3% to vortex-induced vibrations caused by the presence of a passive tugger line, which shifted one of the system's natural frequencies towards the tower's vortex-shedding frequency. Next to wind and wave-induced motion, the data reveal that the hoisting itself induces tower vibrations, accounting for less than 1% of the tower motion response. The collected data offer a distinctive perspective on this type of installation, which is unlikely to be replicated at model scale due to the scaling limitations associated with the interdependence of waves and wind. The data can be used to validate motion control strategies to enhance the efficiency, safety, and workability of floating offshore wind turbine installations.

3.1. Introduction

Driven by the effects of climate change, the global energy sector is undergoing a transition from fossil fuels as main sources of energy to renewable energy. As a result, investments in wind energy have surged in recent decades [23]. As a result of more stable wind conditions and the depletion of onshore and nearshore locations, wind farms are moving further offshore, into deeper waters, [43, 94]. According to a recent Wind Europe report [113], Europe has set the ambitious goal of installing 116 GW of additional wind turbines by 2025, one-fourth of which offshore wind turbines (OWTs). To meet this goal and satisfy ever-increasing energy demands, OWTs with greater capacities and thus bigger dimensions are being installed in deeper waters [38]. Over the years, jack-up vessels have monopolized the installation of OWTs worldwide. As these vessels are constrained by their installation depth and lifting capacity [115], an opportunity arises for heavy lift vessels (HLVs). Traditionally used in the oil and gas industry, HLVs can lift loads up to 20,000 tonnes, and as such appear well-suited for the deployment of heavy wind turbine assemblies at water depths beyond the limits of jackup vessels [57]. Another issue with installing large OWTs is the sensitivity of the operation to wind direction changes (wind veering). The dynamic positioning system (DP) has the potential to reduce this sensitivity, at the price of increasing the sensitivity to wave loading [65, 29]. The latter external excitation is of primary importance to payload motion [29, 99], limiting workability [43].

The project 'Floating installation Offshore XXL wind turbines' (DOT6000-FOX) was funded by the Netherlands Enterprise Agency RVO to study the cost-effectiveness of HLVs for the installation of OWTs compared to current methods, towards broadening the industry's installation options. During the offshore campaign (October 2021), a 2.75 MW OWT was installed. The consortium of the DOT6000-FOX project consists of Delft Offshore Turbine B.V. (DOT), responsible for the OWT; Heerema Marine Contractors Nederland SE (HMC), which employed Sleipnir, the largest semi-submersible HLV to date; and Delft University of Technology (TU Delft), which developed tailored sensors to record the motion of the wind turbine components during various stages of the offshore campaign. These sensors offer the significant advantage of synchronization with any onboard measurement system in Coordinated Universal Time (UTC).

Scaling limitations pose challenges in reproducing offshore operations at model-scale. On one hand, wind loads are a function of the the ratio between inertial and viscous forces, which scales proportionally with the geometric scaling factor (λ) (*Reynolds number scaling*). On the other hand, wave loads are a function of the ratio between inertial and gravitational forces, which scales with the inverse of the square root of λ (*Froude number scaling*). This scaling inconsistency is often referred as "The Dilemma in Model Testing" [68]. Furthermore, mathematical models, as well as reduced-scale models are often simplified, which can condition the outcomes. This work aims at complementing the existing literature by providing an analysis of the full-scale dynamics of an OWT tower installation using a floating vessel and corresponding data. The response of the crane-payload-vessel dynamical system is examined and discussed alongside an analysis of the effects of environmental disturbances. Moreover, the collected sensor data from the attitude and heading reference system (AHRS) deployed offshore, is made publicly available with this article [40] in order to support the reproducibility of results, the validation of numerical models, and the development of novel motion control strategies,

Figure 3.1: Semi-submersible crane vessel Sleipnir of Heerema Marine Contractors performing a floating offshore installation of an OWT [39].

[82, 15].

The paper is organized as follows: The dynamical system of the operation, the development and placement of sensors in the full-scale testing campaign, and the methodology employed for data treatment are presented in Section 2. The numerical model analysis is presented in Section 3. Section 4 details the findings and analysis of the measurements and the system's response. Lastly, Section 5 draws conclusions and offers recommendations for future work.

3.2. METHODOLOGY

3.2.1. DESCRIPTION OF THE DYNAMICAL SYSTEM

This study concerns the set-down stage of the OWT installation, during which the tower is suspended by the crane and lowered towards the monopile foundation. A schematic representation of this operation is presented in Figure 3.2a. Fundamentally, the system comprises the floating crane vessel and the suspended load subsystem that resembles a triple pendulum. The constituent elements of this triple pendulum are the crane cable and block hook, as well as the sling linking the hook to the attachment point of the suspended load. This load corresponds to a hollow cylindrical structure representing the OWT tower. The numerical values for the parameters of this system are listed in Table 3.1.

To compensate for the external disturbances originating from wind and waves, two tugger line systems were deployed (Figure 3.2b). An active tugger line is attached to the hook block to damp out its motion and thus constrain the vibrations of the suspended tower. In addition, a set of passive tugger lines was directly connected to the tower above its center of gravity (Figure 3.2a). The latter tugger line system was connected to a cleat and manually operated by the crew.

Respective to the waterline.

Three stranded polypropylene rope.

Table 3.1: Overview of the system parameters.

Parameter	Notation	Value	Unit
Crane Tip Height	H_k	180	m
Tower Height	L_c	74	m
Averaged Tower Diameter	d_T	3.6	m
Tower Mass	M	226	ton
Block Mass	m	45	ton
Sling Length	ℓ_s	10.6	m
Passive Tugger Length	L_{PT}	2×10^1	m
Passive Tugger Diameter	d_{PT}	0.064	m
Passive Tugger Young's Modulus	E_{PT}	113	GPa
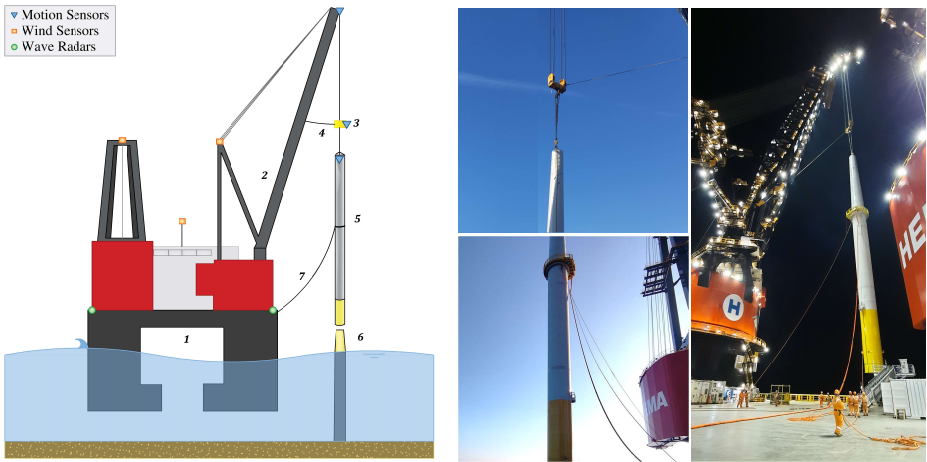
(a) Schematic diagram of the tower installation: 1. Floating vessel, 2. Heavy lift crane, 3. Lifting block/hook, 4. Active (damping) tugger line, 5. Wind turbine tower, 6. Monopile head and 7. Passive (manual) tugger line. Symbols indicate motion sensors, wind sensors, and wave radars.

(b) Tugger lines attached to the OWT tower during installation: Active tugger line attached on the hook block (top left), passive manual tugger line attached on the skybox location on the lower tower (lower left), and overview picture (right).

Figure 3.2: Measurement campaign setup for the floating installation of an offshore wind turbine tower.

3.2.2. SENSORS DESIGN AND PLACEMENT

Since only part of the required data, e.g. wave motion and tugger line loads, are recorded by the vessel's on-board monitoring system, the offshore measurement campaign required the development of tailored motion tracking units, as shown in Figure 3.3a. These units were designed to

- withstand challenging environmental conditions and mechanical loads;
- be deployed at locations that were difficult to access;
- be operated with five days of autonomy;
- synchronize the data to UTC;
- facilitate both real-time data transmission and local data storage.

The units were designed and developed in partnership with the Técnico Solar Boat (TSB) team from the Instituto Superior Técnico in Portugal. They consisted of an AHRS *Xsens MTi-7* GNSS/INS sensor for motion measurements, a *Teensy* microprocessor responsible for reading and locally saving measurements on a micro SD-card, as well as for transmitting them to a receiver station using a *LoRa* radio transceiver. Power was supplied by two 12 Ah Li-Po batteries. The printed circuit board (PCB), designed by TSB, interconnected all subsystems and monitored the batteries' health. The specifications of the AHRS's accelerometer and gyroscope measurements are described in Table 3.2.

Table 3.2: Sensor specifications.

Sensor	Bias	Noise	Sampling Rate
AHRS accelerometer	40 μg	70 μg/$\sqrt{\text{Hz}}$	5 Hz
AHRS gyroscope	6 deg/h	$3 \cdot 10^{-3}$ deg.s^{-1}/$\sqrt{\text{Hz}}$	5 Hz

Wind, wave, and tugger line loads as well as hoisting cable length data were measured during the campaign by an array of radars and sensors, which were strategically located on the vessel as shown in Figure 3.2a. More specifically, wind speeds were measured using anemometers at the top of the cranes' A-brackets and on the met-mast on top of the super-structure. The actual wind speed was estimated from the wind measurements at these points. The sea state was measured using two wave radars, on the starboard and portside of the vessel. The motion measurements were performed using the motion tracking modules presented in Figure 3.3a. The sampling rate of the wind sensors, wave radars, tugger gauges, and hoisting cable encoder was 1 Hz, time synchronized to UTC. For these measurements, the sensors' noise level and bias are not available.

3.2.3. Data Treatment

Each sensor unit measured the raw acceleration and angular velocity in its local frame of reference, which is denoted by XYZ, see Figure 3.3b. This data is publicly available in [40]. Normally, in an AHRS, these motion components are transformed to an Earth-fixed reference frame using GNSS. Here, instead, the raw acceleration and angular velocity data are transformed in post-processing such that the measured mean acceleration vector always aligns with the positive z-axis of the global xyz-frame. This transformation ensures that the gravitational acceleration points along the z-axis regardless of the sensor unit's orientation.

In the local XYZ reference frame, the sensor measures the acceleration $\mathbf{a}'(t)$ and angular velocity $\Omega'(t)$, where the prime denotes the quantity in the local frame. By applying the time-invariant rotation matrix $\mathbf{R}$ to the time signals, the acceleration $\mathbf{a}(t)$ and angular velocity $\Omega(t)$ become

$$\mathbf{a}(t) = \mathbf{R}\mathbf{a}'(t), \tag{3.1}$$

$$\Omega(t) = \mathbf{R}\Omega'(t). \tag{3.2}$$

The rotation matrix $\mathbf{R}$ ensures that the normalized mean acceleration vector $\overline{\mathbf{a}'}$ aligns with the preferred direction of gravitational acceleration, which is denoted by the unit vector $\mathbf{g}$ in Figure 3.3b. Using a variant of Rodrigues' rotation formula [31], the rotation matrix $\mathbf{R}$ is
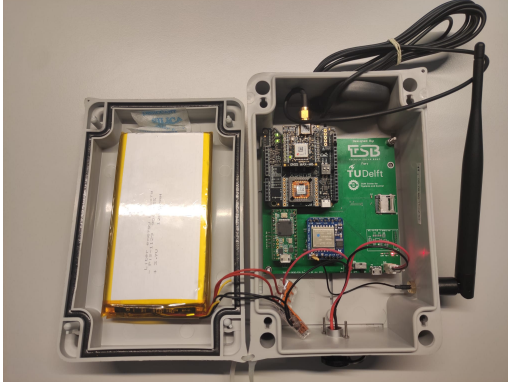
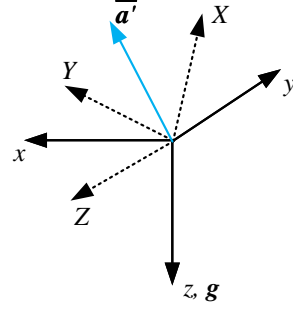(a) Wireless motion tracking module.

(b) Reference frames used for processing the raw acceleration and angular velocity data. Global reference frame xyz, local reference frame XYZ, normalized mean acceleration vector $\overline{\mathbf{a}'}$, and preferred direction of gravitational acceleration $\mathbf{g}$

.

Figure 3.3: Inertial measurement unit data acquisition and respective frames of reference.

given by

$$\mathbf{R} = \mathbf{I} + \mathbf{K} + \frac{1}{1 + \overline{\mathbf{a}'} \cdot \mathbf{g}} \mathbf{K}^2, \tag{3.3}$$

where $\mathbf{I}$ is the identity matrix, $(\cdot)$ represents the inner product, and $\mathbf{K}$ is

$$\mathbf{K} = \mathbf{g} \otimes \overline{\mathbf{a}'} - \overline{\mathbf{a}'} \otimes \mathbf{g}, \tag{3.4}$$

in which $(\otimes)$ denotes the outer product.

After rotation, the acceleration components a_x and a_y are in the plane perpendicular to $\mathbf{g}$, and Ω_z describes the angular velocity about the z-axis. Note that the exact orientations of the x- and y-axes are not defined by this rotation operation. However, since our main interest is to quantify and identify the cause for the motion of OWT components in the plane parallel to the sea surface, the exact orientation of these axes is less important. In the remainder, components a_x and a_y will be referred to as the in-plane accelerations.

3.3. Dynamics of the Crane-Payload-Tugger System

To estimate the natural frequencies of the full-scale system, a simplified mathematical model is used. This model comprises a suspended cylinder of mass M (and a uniform diameter along its length) to represent the tower, and a point mass (m) pendulum representing the hook block and main crane cable (ℓ_h). These two subsystems are connected through a rigid rod simulating the sling (ℓ_s). The resulting triple pendulum is free to oscillate in 3D space and its motion is projected into two perpendicular planes: xz- and yz-plane, see Figure 3.4.

The motion of the system is restrained by the use of tugger lines. In Figure 3.4a, the spatial tugger line placement is presented alongside the orientation of the axes selected as the frame of reference for this model.In contrast with the active tugger attached to the hook block, the passive line is rigidly attached to the vessel deck by means of a cleat. Consequently, this tugger influences the dynamics of the suspended system. Given that it is pre-tensioned, for small motion amplitudes it can be modelled as a linear spring element [62] connecting the vessel's deck to the tower, at a distance $\ell_p = 31\,\text{m}$ from its suspension point, see Figure 3.4. As the passive tuggers are oriented at an angle γ with respect to the two planes, the force exerted by this spring is projected onto two components (with spring coefficients k_x and k_y, respectively) in the xz- and yz-planes to account for its out-of-plane orientation. The complete derivation of the equations of motion of the dynamical system is detailed in 3.5.

(a) Active and passive tugger line orientation.

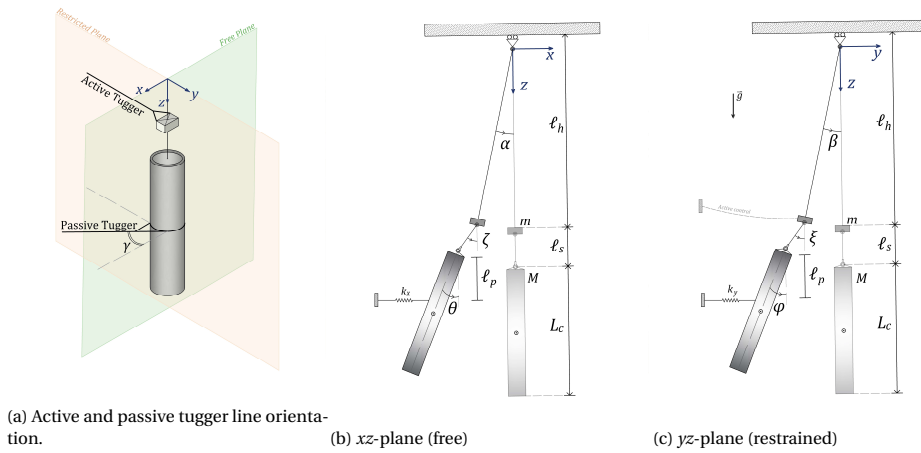(b) xz-plane (free)

(c) yz-plane (restrained)

Figure 3.4: Schematics of the numerically simulated triple spherical pendulum system analogue.

Since the motion of the system is not actively controlled in the xz-plane, it is reasonable to derive the modes of the system by studying only the planar triple pendulum with a spring k_x (Figure 3.4b). The forces exerted by the passive tugger lines were not recorded throughout the operation. Furthermore, the exact orientation of the tugger is not known. Thus, the natural frequencies of the system are calculated as a function of the spring coefficient k_x (for $\gamma = 0°$) as shown in Figure 3.5a. The influence of the stiff spring is evident when $k_x > 10^4$, thus increasing the natural frequencies, especially in the second and third modes. The values of the natural frequencies of the system with (highly restrained system, $k_x = 10^6$ N/m) and without (free system, $k_x = 0$ N/m) a passive tugger line are given in Table 3.3.

The axial stiffness of the passive tugger can be estimated by utilizing the known characteristics of the ropes provided in Table 3.1, as follows:

$$k_{PT} = \frac{E_{PT} A_{PT}}{L_{PT}} = 2.14 \cdot 10^5 \text{ N/m.} \tag{3.5}$$

Evaluating the model with the stiffness k_{PT} for $\gamma = 0°$, the following values for the natural

Table 3.3: Natural frequencies per mode of vibration.

Modes	$k_x = 0\,\text{N/m}$	$k_x = 10^6\,\text{N/m}$	$k_x = 2.14 \cdot 10^5\,\text{N/m}$
Mode 1 [Hz]	$f_{n,1} = 0.048$	$f_{n,1} = 0.094$	$f_{n,1} = 0.087$
Mode 2 [Hz]	$f_{n,2} = 0.112$	$f_{n,2} = 0.332$	$f_{n,2} = 0.166$
Mode 3 [Hz]	$f_{n,3} = 0.446$	$f_{n,3} = 0.918$	$f_{n,3} = 0.581$

frequencies are derived: for Mode 1: $f_{n,1} = 0.087\,\text{Hz}$, for Mode 2: $f_{n.2} = 0.166\,\text{Hz}$ and for Mode 3: $f_{n,3} = 0.581\,\text{Hz}$ (Table 3.3). It is anticipated that these values might be slightly lower due to the out-of-plane orientation of the tugger ($\gamma > 0°$) and the fact that the connection of the tugger to the cleat is not perfectly stiff. Figure 3.5b presents the decrease in the effective spring coefficient k_x (for the estimated stiffness k_{PT}) for different angles γ as well as the corresponding values of the natural frequencies of the three modes. A small decrease occurs in the natural frequency of the second and third modes when $\gamma > 20°$.

(a)

(b)
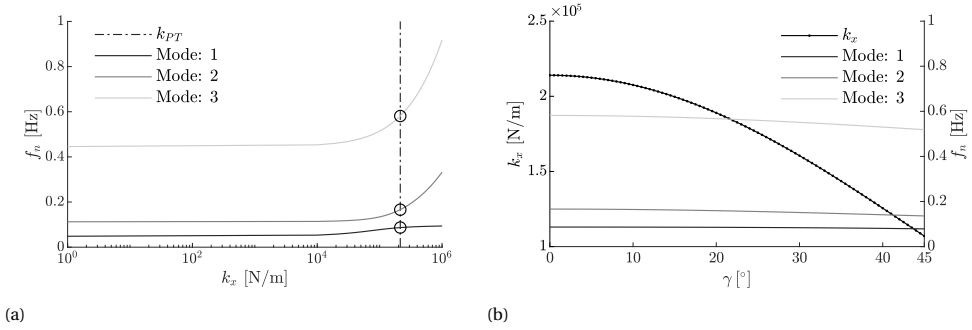
Figure 3.5: (a) Natural frequencies for different stiffness coefficients k_x and $\gamma = 0°$. (b) Stiffness k_x (left vertical axis) and corresponding natural frequency f_n (right vertical axis) for estimated tugger stiffness k_{PT} and different orientation angles γ.

Once aligned with the monopile foundation, the tower is progressively lowered (with intervals of constant length). The time series of the main cable payout length (ℓ_h) during the two lifts studied is shown in Figure 3.6. To assess the effect of the changes in payout length (l_h) on the dynamic behavior of the system, an analysis was performed using the frequency-domain framework presented by Domingos *et al.* [43]. The results shown in Figure 3.7 are in accordance with the natural frequencies presented in Table 3.3 for the unrestrained case. Moreover, the recorded changes in the payout length have limited influence on the dynamic response of the system.

3.4. DATA ANALYSIS AND DISCUSSION

The operation analyzed in this work is the lowering of an OWT tower on a pre-installed monopile using a semi-submersible crane vessel (Figure 3.2a). During the lowering, the crane's orientation and boom angle were kept constant; the only parameter that varied was the hoisting length as the tower was lowered towards the monopile. Datasets from two separate lifts are studied and compared to gain insight into the influence of different

(a) Lift 1.   (b) Lift 2.
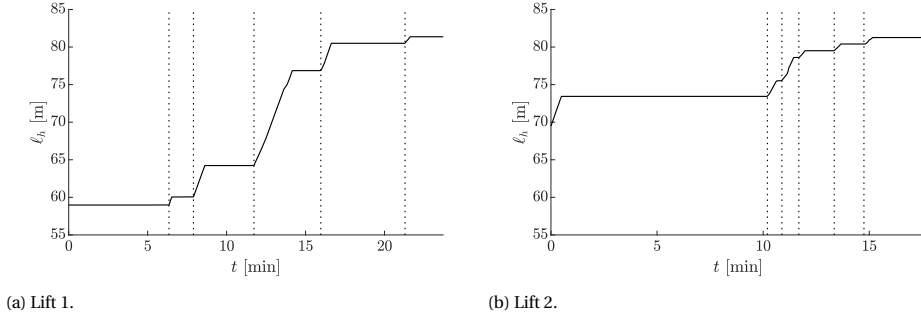
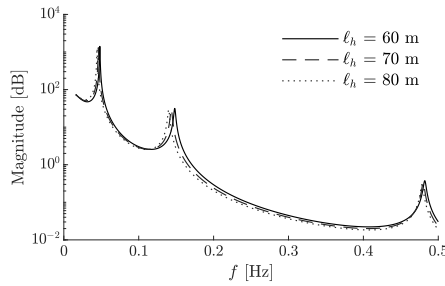Figure 3.6: Payout length as a function of time during tower installation.

Figure 3.7: Unrestrained tower motion response to crane tip accelerations for different payout lengths.

external environmental excitations and lowering speeds on the response of the overall dynamical system.

For the in-plane motion of the two components of the tower-block system, the power density spectra are analyzed to identify the frequency range contributing most significantly to the tower's motions. Subsequent time-frequency analysis delves into the time variance of the energy to identify the modes of vibration as well as the physical processes exciting these modes. One of the processes, wind-induced vibrations, is discussed in more depth. Lastly, in section 3.4.4, the contribution of these disturbances to the actual motion of the components is analyzed.

3.4.1. POWER DENSITY SPECTRA OF THE IN-PLANE ACCELERATION

Figure 3.8 presents the power density spectra (PDS) of the in-plane accelerations of the different components of the system as well as the energy density measured by the wave radars for Lift 1 and 2. It is noted that the tugger line tension has a non-zero mean, which is attributed to the variation in tugger tension set-point during the operation. By comparing the wave energy spectra of the portside (PS) and starboard (SB) wave radars for Lift 1 and Lift 2, it is clear that the sea state was calmer during Lift 2 than during Lift 1. The peak period T_p and significant wave height H_s are determined from these uni-directional spectra as follows: $T_p = 12.2\,\text{s}$ and $H_s = 0.45\,\text{m}$ for Lift 1 and $T_p = 13.5\,\text{s}$ and $H_s = 0.30\,\text{m}$ for Lift 2. These values suggest that the two operations were conducted under calm sea

(a) Lift 1.   (b) Lift 2.
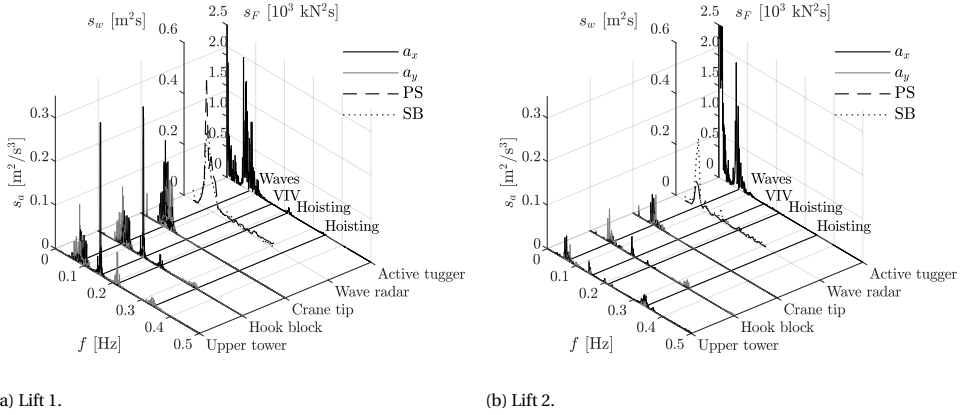
Figure 3.8: Power density spectra for the in-plane accelerations, the wave radar, and the active tugger line force as measured during Lift 1 and Lift 2. The translational accelerations in the xy plane are denoted as α_x and α_y for the x- and $y$axis, respectively. The abbreviations PS and SB denote the port side and starboard side of the vessel, respectively. The acceleration power density spectra uncertainty is of the order $\mathcal{O}(10^{-4})$, Figure 3.13. For the remaining measurements, sensor bias and noise are not available.

conditions.

The crane tip, hook block, and upper tower acceleration spectra have a common acceleration peak at approximately 0.09 Hz for both lifts (Figure 3.8). This peak matches the data from the wave radars, suggesting that, at this frequency, wave energy is effectively being transferred to the block-tower system through the crane tip. Note that the motion sensors have a higher sampling rate than the wave radars, resulting in a higher resolution of the acceleration spectra. Naturally, the energy associated with the crane tip motion of Lift 1 is higher than Lift 2, due to the higher wave energy density of the former.

The crane tip sensor detected only one acceleration peak frequency, matching the range of wave energy measured by the wave radars. However, it is clear that other frequency components are also present in the response of the hook block and the tower, namely 0.15 Hz, 0.21 Hz, and 0.34 Hz.

3.4.2. TIME-FREQUENCY ANALYSIS

A time-frequency analysis is performed to identify the moments in time when the frequencies of 0.15 Hz, 0.21 Hz and 0.34 Hz were excited. Figure 3.9 presents the time-frequency responses of the different motion components measured by the hook sensors. For each time-frequency plot, the corresponding power density spectrum is presented on the left-hand side, while a_x and a_y correspond to the acceleration in the free and restricted plane, respectively (Figure 3.4). As discussed in section 3.3, these planes are defined by the presence of the active tugger line at the hook block. Note that Ω_z denotes the angular velocity around the z-axis of the hook block.

Figures 3.9d and 3.9e are obtained by subtracting the translational acceleration component caused by the block rotation, as the sensor was not placed at the block's centre of

(a) Hook block a_x.

(b) Hook block a_y.

(c) Hook block Ω_z.

(d) Hook block a_x, no rotation.

(e) Hook block a_y, no rotation.
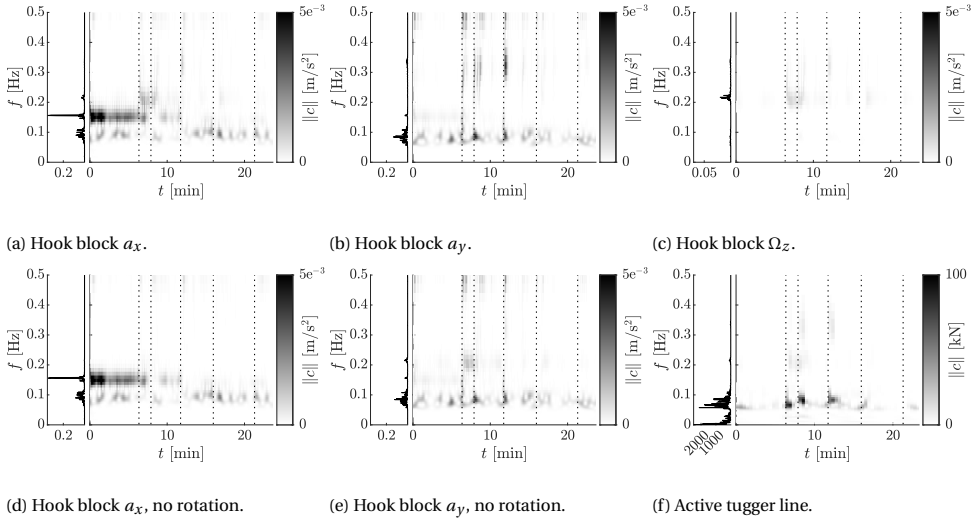
(f) Active tugger line.

Figure 3.9: Time-frequency plot of the hook block accelerations and angular velocity around its vertical axis, and active tugger tension during Lift 1. The dashed vertical lines denote the moments when the tower was lowered. For each component, the corresponding power density spectrum is presented on the left-hand side.

rotation. The acceleration due to rotation $\mathbf{a}_\Omega(t)$ is given by

$$\mathbf{a}_\Omega(t) = \frac{\mathrm{d}}{\mathrm{d}t}\mathbf{L} \times \Omega(t), \tag{3.6}$$

in which $\mathbf{L}$ is the vector from the centre of rotation of the hook block to the location of the sensor, and ($\times$) denotes the cross product. In this case, $\mathbf{L} = [-0.90, 0.68, 0.35]^\mathrm{T}$ m.

From the figures, it becomes clear that the waves induce translational motions throughout the entire operational time window. The peaks at 0.21 Hz and 0.34 Hz are concentrated at relatively small time intervals, which coincide with the moments when the hook block and the tower are lowered. These lowering operations are indicated by vertical lines in time-frequency plots. As the lowering begin, the wire is paid out relatively quickly compared to the other characteristic dynamics of the suspended system. This sudden acceleration, which can be compared to an impact load, in combination with the restrictions posed by the tugger lines, excites a range of vibration modes (translational and rotational). Comparing Figure 3.9a with 3.9d, and 3.9b with 3.9e, it is evident that most of the energy at 0.21 Hz and 0.34 Hz is not present when the rotational component is removed. However, for Lift 1, the acceleration a_y still displays some energy at 0.21 Hz (Figure 3.9e). This is caused by the action of the active tugger line, as can be seen in Figure 3.9f, where the time-frequency response of the active tugger line is presented. The time-frequency responses for Lift 2 can be found in 3.5, which show similar behavior as described here for Lift 1.

The remaining energy peak at $f = 0.15$ Hz has a more consistent presence during the first 10 minutes of the time window shown. According to Table 3.3, this vibration occurs when the second translational natural frequency of the system in the free plane

(containing the passive tugger line) is excited. Since the cable length was constant and equal to 60 m (Figure 3.6a) during this time interval, the wind may have excited the system at this frequency due to vortex shedding from the tower. In the following section, the possibility of vortex-induced vibrations is investigated.

3.4.3. VORTEX-INDUCED VIBRATIONS

Flow past cylinders has been extensively described in the literature given the periodic nature of the resulting lift forces. These forces are caused by vortices that shed alternately from each side, which can excite natural modes of mechanical systems, resulting in so-called Vortex-Induced Vibration (VIV) [112]. The vortex shedding frequency is governed by the Reynolds (Re) and Strouhal (St) dimensionless numbers [66], which, for a stationary cylinder, can be determined by using the following expression:

$$f = \frac{St(Re)U}{D},$$ (3.7)

in which f represents the vortex shedding frequency in Hz, U the flow velocity in m/s and D the cylinder diameter in m. For the range of Reynolds numbers of interest ($\approx 7 \times 10^5$), the Strouhal number is approximately 0.22.

The average wind speeds for Lift 1 and 2 during the measurement campaign were approximately 2.5 and 4 m/s, respectively, as shown in Figure 3.10. Furthermore, the wind direction during the operation was stern-quartering starboard side. During the first 10 minutes of Lift 1, when motions at 0.15 Hz were excited, a fairly constant wind was present with a speed of approximately 2.5 m/s (Figure 3.10a). As the speed of the wind gradually increased after 10 minutes, the intensity of the energy at this frequency decreased. This behavior suggests that the motion with this frequency may be induced by the wind.

To check whether VIV is induced in the system, the average wind speed is compared to the so-called critical velocities of the system. At these velocities, the natural frequency of the system coincides with the vortex shedding frequency. Hence, a critical velocity $U_{c,i}$ is given for each natural frequency $f_{n,i}$ by

$$U_{c,i} = \frac{f_{n,i}D}{St(Re)}.$$ (3.8)

For wind speeds around the critical velocity, the vortex shedding frequency will be equal to the natural frequency, i.e. frequency lock-in occurs. For a cylinder in air, this lock-in region is a relatively narrow velocity band. However, given the large dimensions and mass of the present structure, no experimental data exist to specify the exact extent of this lock-in region. Therefore, in accordance with Ehrmann *et al.* [47], the lock-in region is assumed to be between $0.63U_c$ and $1.4U_c$.

Figure 3.10c presents the average wind speed divided by the critical velocities for the crane-payload-vessel system (Table 3.3) during Lift 1. It is clear that for the second mode of vibration the wind speed is close to the critical velocity, and VIV can be generated. When the wind speed increases after $t = 10$ min, it remains within the potential lock-in band (grey shading). Figure 3.9 indicates a reduction of VIV earlier than what is predicted in Figure 3.10c. A possible explanation is wind speed estimation errors caused by vessel blockage and atmospheric boundary layer effects. Furthermore, VIV is sensitive

to hoisting cable length variations, despite the apparent limited influence of hoisting on the dynamic response of the system (see Figure 3.7). For Lift 2, Figure 3.10d shows that the wind speed is well outside the lock-in region for all three modes of vibration. Therefore, VIV is not be expected to occur.

Note that a limitation of this analysis is the high uncertainty in the width of the VIV lock-in region for structures with small relative added mass. [47] reports locking ranges for systems with m* (object mass/added mass) up to 67, while the system under consideration is estimated to have m* ≈ 245. Furthermore, the wind measurements were performed on top of the cranes' A-brackets (Figure 3.2a). They are therefore not necessarily representative of the flow field at the tower's location.

(a) Lift 1.

(b) Lift 2.

(c) Lift 1.

(d) Lift 2.
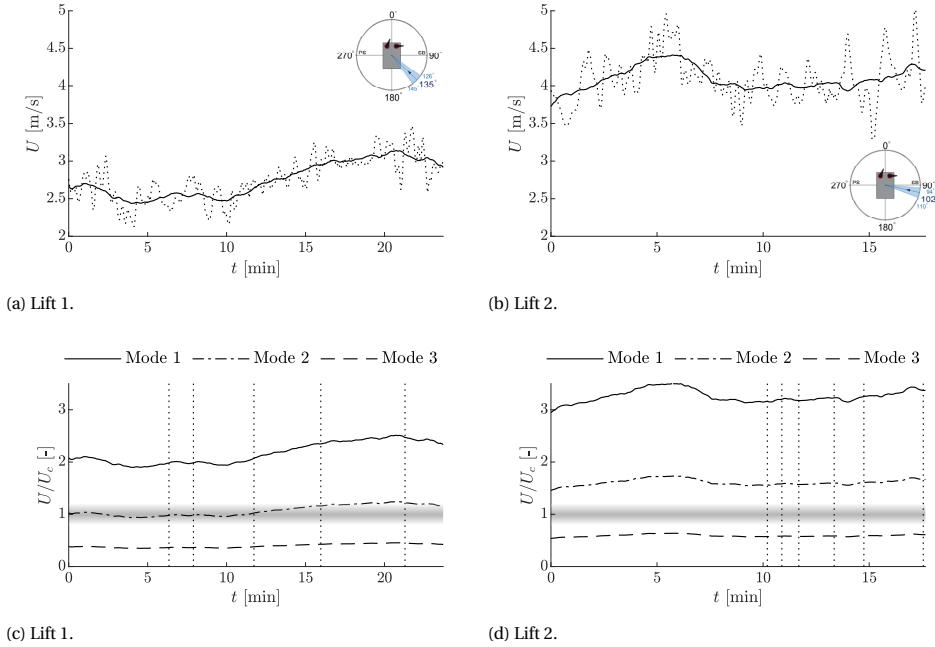
Figure 3.10: Wind speed and direction during the offshore measurement campaign of Lifts 1 (left) and 2 (right). In the top panels, the measured wind speed is shown in the dotted lines, while the solid lines are the moving averages using a three-minute window. The lower panels present the velocity divided by the mode-dependent critical velocities. The gray band denotes the area where frequency lock-in is possible.

3.4.4. INDIVIDUAL CONTRIBUTIONS OF DISTURBANCES TO THE MOTION OF THE TOWER AND BLOCK

Figure 3.8 presents the power density spectra of the accelerations at the hook block and upper tower. Converting these results to translational displacements is not trivial. Therefore, to compare the impact of each source of disturbance of block and tower motion, the cumulative standard deviation is computed. The motion of the sensors respective to the equilibrium position of the system **u** is obtained by the double-time integration of the
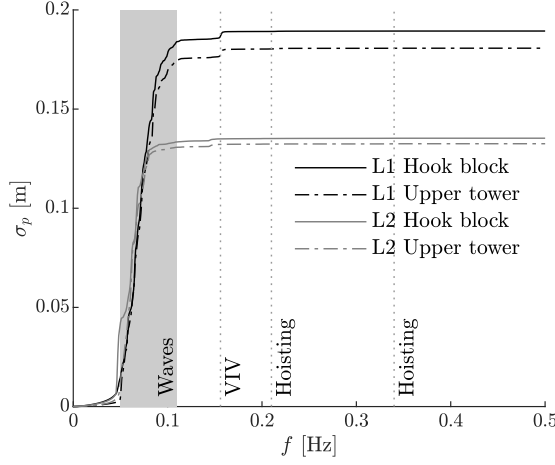
Figure 3.11: Cumulative standard deviation spectrum of the hook-block and upper-tower motion during Lift 1 (L1) and Lift 2 (L2).

acceleration:

$$\mathbf{u} = \iint \tilde{\mathbf{a}} \, dt \, dt, \tag{3.9}$$

in which $\tilde{\mathbf{a}}$ is the filtered in-plane acceleration vector, the components of which were filtered using a high-pass filter with $F_c = 0.05$ Hz to eliminate the effect of sensor drift.

From here, the motion spectrum of $\mathbf{u}$ is obtained by computing the Fast Fourier Transform (FFT) in which the two in-plane displacements (u_x and u_y) are treated as a single complex-valued quantity $u = u_x + u_y \mathrm{i}$, resulting in the position frequency spectrum $p(f)$. The power density spectra of $p(f)$ are then given by:

$$S_p(f_i) = \frac{p^2(f_i)}{2\Delta f}, \tag{3.10}$$

where i represents the ith discrete frequency, and Δf the chosen frequency step in Hz. Finally, the cumulative standard deviation is given by:

$$\sigma_p(f_i) = \sqrt{\int_0^{f_i} S_p(f) \, df}. \tag{3.11}$$

More details on the frequency analysis methodology can be found in [43] and [60]. Figure 3.11 presents the resulting positional cumulative standard deviation (σ_p), determined from the measured data.. The figure reveals that during the floating installation of the wind turbine tower, waves contributed approximately 96% of the block and tower-top motion, while VIV accounted for 3%. Although the effect of hoisting is visible in Figure 3.8 and 3.9, it clearly did not significantly affect the hook block and upper-tower motion during the measurement campaign.

3.5. Conclusions

The first-ever full-scale measurement campaign for the installation of an offshore wind turbine (OWT) tower using a floating heavy-lift vessel was reported. A series of novel time-synchronized motion tracking modules were developed and placed in strategic positions to capture the dynamic response of the suspended system to environmental disturbances throughout the operation. An analysis of two tower lifts shows that wave disturbances were consistently present during the whole operation and were responsible for about 96% of the hook block and tower motion, while 3% of the motion is attributed to the presence of an additional passive tugger line, which introduced a natural frequency in the range of wind-driven vortex shedding frequencies, despite the calm environmental conditions. Although the remaining disturbances did not significantly contribute (<1%) to the positional standard deviation of the hook block and tower, a rotational motion of the hook block around its vertical axis is still observed, and its excitation coincides with the hoisting of the payload. According to the data collected, vortex-induced vibration (VIV) is sensitive to hoisting cable length variations, despite the apparent limited influence of hoisting on the dynamic response of the system. Measurements of the tension in the active tugger line, connected to the hook block, show variations in the frequency range of the wave-induced motion, with a small peak at 0.21 Hz, which corresponds to the natural frequency of the block rotation.

The time-synchronized motion tracking modules developed for this campaign succeeded in gathering relevant data in an environment where robustness and versatility are key features. Therefore, their use is advised in future wind turbine installations. In future work, it is recommended to perform an analysis of other phases of the OWT assembly process, so that motion control strategies can be developed for them. Furthermore, conducting measurements in more demanding weather conditions will offer a broader perspective on the floating installation of OWTs, yielding valuable insights for crew training purposes and for improving motion control strategies.

Appendix

Numerical Model: Governing Equations

The triple pendulum shown in Figure 3.4 has six degrees of freedom (DOFs), which pertain to the different angles of the pendulum components in the two planes, namely in *xz*-

and yz-plane: the point mass pendulum angle is given by α and β, the sling angle is ζ and ξ, and the angle of rotation of the cylinder around its top point is θ and ϕ in xz- and yz-plane, respectively, as shown in Figure 3.4.

The coordinates that describe the motion of the pendulum are given in terms of its three moving components as follows:

$$\mathbf{P}_h(t) = \begin{pmatrix} \ell_h \sin\alpha \\ \ell_h \cos\alpha \sin\beta \end{pmatrix}, \tag{3.12a}$$

$$\mathbf{P}_s(t) = \begin{pmatrix} \ell_s \sin\zeta \\ \ell_s \cos\zeta \sin\xi \end{pmatrix} + \mathbf{P}_h(t), \text{ and} \tag{3.12b}$$

$$\mathbf{P}_L(t) = \begin{pmatrix} L \sin\theta \\ L \cos\theta \sin\phi \end{pmatrix} + \mathbf{P}_s(t), \tag{3.12c}$$

where $\mathbf{P}_L(t)$, $\mathbf{P}_s(t)$ and $\mathbf{P}_h(t)$ are the position vectors of the hanging cylinder, the sling endpoint, and hook mass, respectively. L corresponds to the distance along the longitudinal axis of the cylinder.

The kinetic K and potential U energy of the dynamical system are given by

$$K = \frac{1}{2} M \left\| \dot{\mathbf{P}}_{L,c}(t) \right\|^2 + \frac{1}{2} m \left\| \dot{\mathbf{P}}_h(t) \right\|^2 + T_\omega, \tag{3.13a}$$

$$U = Mg \left(\ell_h + \ell_s + L_c - \hat{\mathbf{k}} \vec{\mathbf{P}}_{L,c}(t) \right) + mg \left(\ell_h - \hat{\mathbf{k}} \mathbf{P}_h(t) \right) + \tag{3.13b}$$

$$\frac{1}{2} k \left\| \cos\gamma \hat{\mathbf{i}} \mathbf{P}_{L,p}(t) \right\|^2 + \frac{1}{2} k \left\| \sin\gamma \hat{\mathbf{j}} \mathbf{P}_{L,p}(t) \right\|^2,$$

where $\hat{\mathbf{i}}$, $\hat{\mathbf{j}}$, and $\hat{\mathbf{k}}$ represent the unit vectors of the horizontal x- and y-axis, and the vertical z-axis, respectively. γ is the directional angle of the passive tugger line with respect to the x-axis. $\mathbf{P}_{L,c}(t)$ and $\mathbf{P}_{L,p}(t)$ correspond to the position vectors of two points on the hanging cylinder, namely the endpoint ($L = L_c$) and a point above the center of gravity at $L = 31$ m. T_ω represents the rotational kinetic energy of the hanging load [89] and can be expressed as

$$T_\omega = \frac{1}{2} I_x (\dot{\phi})^2 (\cos\theta)^2 + \frac{1}{2} I_z (\dot{\phi})^2 (\sin\theta)^2 + \frac{1}{2} I_y (\dot{\theta})^2, \tag{3.14}$$

where I_x, I_y, and I_z are the moments of inertia of the rotation of the cylinder around its three axes.

For the derivation of the equation of motion, the Lagrangian $\mathscr{L}$ is formulated as follows:

$$\frac{\mathrm{d}}{\mathrm{d}t} \left(\frac{\partial \mathscr{L}}{\partial \dot{\theta}} \right) - \frac{\partial \mathscr{L}}{\partial \theta}, \tag{3.15}$$

where $\mathscr{L} = K - U$. To simplify the simulation of the system, the following assumptions are made: 1) the cable lengths of the hook (ℓ_h) and sling (ℓ_s) are considered as rigid massless elements in the derivation, and 2) the displacements of the hanging components are small compared to the lengths of the pendulum, resulting in the small angle approximation ($\sin\theta \approx \theta$ and $\cos\theta \approx 1$). With assumptions, evaluating eq. (3.15) gives the following linearized equations of motion (EOMs) of the free vibrations of the dynamical system:

where **R** is a transformation matrix, given by

$$\mathbf{R} = \begin{pmatrix} \cos^2\gamma & \cos\gamma\sin\gamma \\ \cos\gamma\sin\gamma & \sin^2\gamma \end{pmatrix}. \tag{3.17}$$

Note that geometrically linearizing the EOMs around the equilibrium position leads to the uncoupling of the motion of the triple pendulum in the two separate planes. The resultant of the two planes is the spherical position of the system. In the case of a free suspension ($k = 0\,\text{N/m}$), the system is fully symmetrical, and, therefore, the problem can be reduced to two identical planar triple penduluns in two perpendicular planes, each with 3 DOFs. However, the additional constraint added to the cylinder by the spring introduces an asymmetry in terms of stiffness and coupling of the planes depending on the orientation of the spring.

The equations of motion can be represented in matrix form as:

$$\mathbf{M}\ddot{x} + \mathbf{K}x = 0, \tag{3.18}$$

where $x = [\theta, \phi, \alpha, \beta, \zeta, \xi]^{\mathrm{T}}$ is the vector of the system's states, and **M** and **K** are the mass and stiffness matrices, respectively.

The response of the system is assumed to be equal to:

$$x = \bar{X}e^{i\omega_n t}, \tag{3.19}$$

where ω_n represents the natural frequencies of the system which can be determined by solving the eigenvalue problem [30].

The characteristic equation is given as

$$\det\left(\mathbf{K} - \omega_n^2\mathbf{M}\right) = 0, \tag{3.20}$$

with the non-trivial, real and positive roots of ω_n^2 giving the natural frequencies.

(a) Hook block a_x (b) Hook block a_y (c) Hook block Ω_z

(d) Hook block a_x, no rotation   (e) Hook block a_y, no rotation   (f) Active tugger line
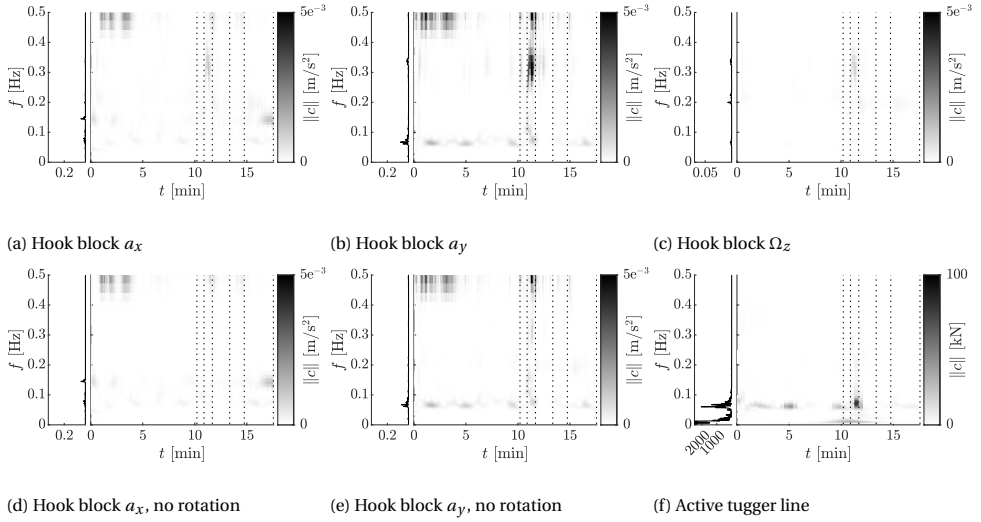
Figure 3.12: Time-frequency plot of the hook block accelerations and angular velocity around its vertical axis, and active tugger tension during Lift 2. The dashed vertical lines indicate the moments at which the tower was lowered. For each component, the corresponding power density spectrum is presented on the left-hand side.

TIME-FREQUENCY PLOTS

Figure 3.12 presents the time-frequency analysis of the hook block in-plane acceleration and angular velocity together with the active tugger line load for Lift 2. By employing the same procedure as described in section 3.4.2 for Lift 1, the acceleration caused by pure rotation of the block is removed from the acceleration signals. Just as for Lift 1, the acceleration peaks at 0.34 Hz are caused solely by block rotation, which in turn is caused by the lowering of the block.

UNCERTAINTY PROPAGATION ANALYSIS

Figure 3.13 presents the uncertainty in the acceleration power spectra, based on the data in Table 3.2.
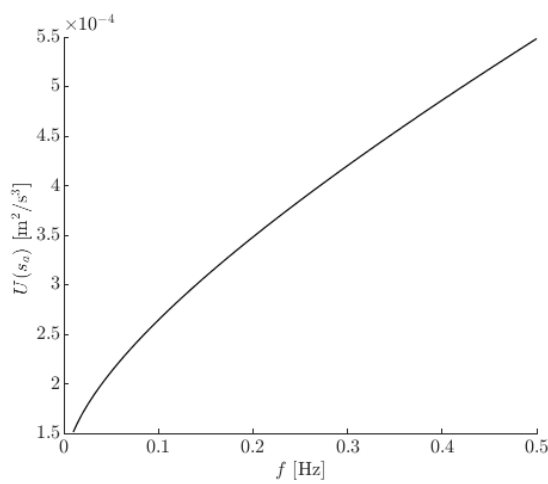
Figure 3.13: Uncertainty of the acceleration power density spectra based on the sensor's specifications, see Table 3.2.

4

MODEL-BASED CONTROL OF A CONTROL MOMENT GYROSCOPE FOR FLOATING INSTALLATION OF WIND TURBINE TOWERS

"Anyone who believes that exponential growth can go on forever in a finite world is either a madman or an economist."

-Kenneth Boulding

With wind farms moving towards deeper waters and wind turbines getting bigger, floating crane vessels become an attractive alternative to jack-up vessels. However, floating vessels are more susceptible to wave induced motions, which increases operational downtime. To address this issue, the present work explores the modeling and control of a scissored pair control moment gyroscope. This active motion compensation system is attached to the crane's hook, mitigating wind turbine tower motions during the installation.

A mixed sensitivity $\mathcal{H}_\infty$ framework is proposed for the controller synthesis, ensuring a trade-off between, performance, robustness and actuator usage. The resulting controller performs disturbance rejection and applies motion damping. Consequently, a 20 to 40% motion reduction is observed across a wide range of tower sizes and payout lengths, while keeping the actuation below prohibitive limits. In the context of a case-study, a 16 percentage point increase in yearly workability is achieved compared to previous results.

4.1. INTRODUCTION

Wind energy is one of the most promising renewable sources of energy, for mainly two reasons: availability and cost. Currently, onshore wind is by far the most inexpensive source of energy overall, with a levelized cost of energy (LCOE) less than half that of coal [107]. However, public opinion and space constraints have driven the development of its counterpart, offshore wind energy [9]. With offshore turbines increasing in size and being installed in areas with higher wind speeds, exponential power gains are expected [76]. As a result, the European Union has set an ambitious target of reaching 88 GW of offshore wind capacity by 2030 and 360 GW by 2050 [5], attracting significant investments for the development of larger turbines [23, 10].

The installation of offshore wind turbines (OWTs) requires a high level of precision. Thus, a steady platform on the sea greatly improves the safety and complexity of the operation. For this reason, jack-up vessels became an industry standard regarding the installation of wind turbines [43]. These vessels use large metallic legs to lift themselves above the sea surface, mitigating wave-induced motions during installation, see Figure 4.1. However, what makes them convenient also limits them. With wind farms moving towards

Figure 4.1: A wind turbine jack-up installation vessel [21].

deeper waters and turbines getting bigger, jack-up vessels face challenges in keeping up with the market. Fortunately, there is an already existing alternative: Semi-Submersible Crane Vessels (SSCVs), see Figure 4.2a.

These SSCVs featuring two large cranes, are made to perform complex installations at sea without the need of jacking up. This allows operations at any water depth and their orientation relative to the wind can be adjusted in real time. However, these vessels are more susceptible to wind and wave induced motions compared to jack-up vessels. To prevent down-time, motion control is often applied using active tugger lines, which are designed to handle a wide range of payloads, from hundreds to thousands of tons, see Figure 4.2b. However, the offshore wind energy sector has prompted interest in more

(a) SSCV *Sleipnir* performing the first floating installation of a wind turbine tower.

(b) SSCV *Sleipnir's* tugger line system during offshore wind turbine tower installation.

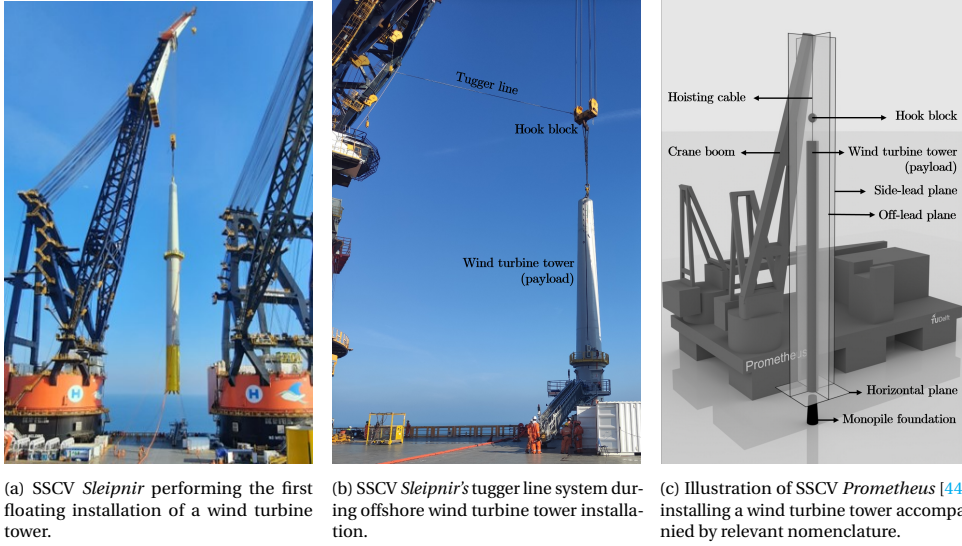(c) Illustration of SSCV *Prometheus* [44] installing a wind turbine tower accompanied by relevant nomenclature.

Figure 4.2: Floating installation of wind turbine towers.

tailored motion compensation systems, with three main reasons being: 1) Compared to offshore oil and gas (O&G) structures, wind turbine components have a small weight to size ratio, making them more susceptible to wind induced motions; 2) their installation consists of many high precision steps; and 3) in contrast to O&G structures, offshore wind turbines are installed at the scale of hundreds, all featuring nearly identical components.

The use of tugger lines to enhance the success and safety of offshore operations has become a standard in the offshore industry. These lines are often attached either to hook block or to the payload directly [82], see Figure 4.2b. Frequently used in constant tension (CT) mode, tugger lines are usually actuated via a winch [82]. Although CT mode does not reduce payload motions, it is useful to adjust the position of the payload. With the intention of enhancing their effectiveness, a linear feedback control loop, which adjusts the line tension proportionally to its speed has been proposed in the literature to damp motions [64]. Simulations and tank tests have demonstrated promising results [82]. However, these studies have not explored the robustness and performance of the control system for different payload types and sizes. Furthermore, a drawback of this system is that it does not allow compensating motions in the side-lead and off-lead planes in an independent manner, see Figure 4.2c. This has motivated research into alternative mechanisms, one being the use of a large number of lifting wires which can compensate both vertical and horizontal plane motions using an ingenious control allocation algorithm [98]. However, with this lifting concept being fundamentally different from traditional ones, it does not provide an answer to the needs of existing heavy-lift vessels.

A challenging aspect of motion compensation for wind turbine tower installation is that the attachment of installation aiding devices to the tower can compromise its structural integrity and corrosion protection coating. When using tugger lines this often

means attaching them to the hook block instead, as shown in Figure 4.2b. This results in an challenging control problem, since the controller is indirectly controlling the tower position. This added difficulty arises from the presence of system dynamics between the location of the actuator (*e.g.* the hook-block) and the desired location of motion control performance (the tower bottom), requiring a careful controller design. In a ingenious attempt to overcome this issue, Atzampou *et al.* have proposed a novel actuator using electromagnets, which can induce a force directly on the tower without being in direct contact with it [16]. However, the simultaneous control of motions in the side-lead and off-lead planes remains a challenge since in the proposed system the direction of magnetic force is unique and constant. In an attempt to overcome these limitations, this paper looks into the use of Control Moment Gyroscopes (CMGs).

CMGs consist of one or more gyroscopes bundled together to generate momentum in a desired direction, or multiple directions in an independent manner, without the need of applying external force/momentum. This can be used to attenuate motions (*e.g.* ship roll [92]), stabilize systems (*e.g.* humans [106]) and/or to control the orientation of objects (*e.g.* spacecrafts [70]). Preliminary research conducted by *Kusters* [67], showed that a scissored pair of actively controlled gyroscopes connected to the crane's hook of an SSCV, could significantly increase the workability of OWT tower installations. However, it shows that model-based manual-loop shaping fails to ensure a reasonable trade-off between performance, robustness and actuator usage, which still remains a challenge.

So far, it is possible to identify four main gaps in literature regarding motion compensation for floating installation of wind turbine towers: 1) Lack of specificity for tower installations, *e.g.* [82];2) too low technological readiness level for offshore application, *e.g.* [98]; 3) lack of independent side-lead and off-lead motion control ability, *e.g.* [16]; and 4) Lack of a suitable controller synthesis framework which ensures a reasonable trade-off between motion compensation actuation, performance and robustness, *e.g.* [67]. To address these points, in this paper we propose to use a $\mathcal{H}_\infty$ mixed-sensitivity framework for the synthesis of a controller for a hook-mounted control moment gyroscope, which can eventually be used to independently control motions in both side and off-lead planes. Given this, the main contributions of this paper are: 1) Investigation of the effectiveness of a scissored pair control moment gyroscope in enhancing the workability of floating installation of wind turbine towers; 2) An analysis of the control system robustness and performance to parametric uncertainties; and 3) Analysis of year-round workability gains in the context of a case-study.

The remainder of this paper is structured in the following way. In section 4.2 the mathematical modeling of the system and actuator is presented, as well as the respective numerical values. This is followed by the introduction of a model-based control framework in section 4.3. The robustness and performance of the control system are analyzed in section 4.4, and the year-round workability is discussed in the context of a case-study. This finally leads to the conclusions of this paper, section 4.5.

4.2. System Modelling
The floating installation of an OWT tower is characterized by wave loads, wind loads and multi-body dynamics. For the sake of model based control this system is simplified. Therefore, this paper extends the 2D linear time-invariant model proposed in [43] to
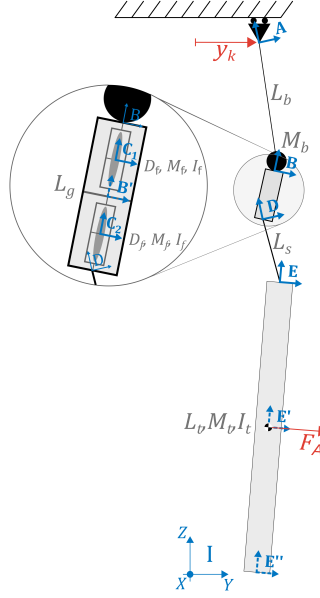
Figure 4.3: Free body diagram of the system representing the floating installation of an OWT tower using a control moment gyroscope.

include a control moment gyroscope (CMG). This actuator is composed of a scissored pair of gyroscopes on top of each other, as shown in Figure 4.3. By spinning and precessing the gyroscopes symmetrically, a reaction torque can be generated exclusively in the off-lead or side-lead planes of motion. This approach aims to mitigate tower motions while simultaneously canceling undesired out-of-plane torque components. [67]. This section delves into a detailed derivation of this linear time-invariant model.

4.2.1. FRAMES OF REFERENCE AND THE GYROSCOPIC EFFECT

In Figure 4.3 we represent the floating installation of an OWT tower, where the movement of the cart represents the crane tip moving horizontally, due to wave induced motions. The symbol y_K is the crane tip position relative to the inertial Frame of Reference (FoR) I, in [m]; L_b and M_b are the hoisting cable length and hook-block mass in [m] and [kg], respectively; D_f, M_f and I_f are the diameters, mass and spinning inertia of the flywheels in [m], [kg] and [kgm^2], respectively; L_g and L_s are the length of the CMG and of the link connecting the CMG to the tower top, in [m]; L_t, M_t and I_t are the height, mass and inertia of the OWT tower in [m], [kg] and [kgm^2], respectively; and finally F_A are the aerodynamic forces on the tower induced by wind [43], in [N].

The non-inertial FoR A, attached to the hoisting cable, has an angle ϕ_A relative to I, in [rad]. With the notation being consistent for the angles of the remaining non-inertial FoR, *i.e.* ϕ_B, ϕ_{C1}, ϕ_{C2}, ϕ_D and ϕ_E, in [rad]. For the ease of mathematical representations FoR E' and E'' are defined at the tower's center of gravity and bottom, also sharing ϕ_E. FoR B' is defined at the center of gravity of the CMG, sharing ϕ_B with FoR B.

The system states so far discussed allow to describe the positions of any element of the system in the cartesian YZ plane. However, the frames of reference C have an additional degree of freedom (DoF), namely the precession. This DoF, represented as ψ in [rad], gives direction to the angular momentum of the flywheel, resulting in a reaction torque in a differentdirection, as can be seen from the *Euler* equations for a spinning disk:

$$\begin{cases} \frac{I_f}{2}(\ddot{\phi} - \dot{\alpha}\dot{\psi}) = \tau_\phi \\ I_f \cdot \ddot{\alpha} = \tau_\alpha \\ \frac{I_f}{2}(\ddot{\psi} + \dot{\alpha}\dot{\phi}) = \tau_\psi \end{cases}, \tag{4.1}$$

here τ represents an external torque applied to the flywheel, in [Nm]. Dots above symbols represent differentiation with respect to time. For the sake of generalization ϕ, α and ψ represent rotations around the x, y and z axis, in [rad]. It is possible to observe that an induced torque component arises in ϕ as result of the cross-coupling between the spinning speed ($\dot{\alpha}$) and the precession speed ($\dot{\psi}$), [rads^{-1}] . This is justified by the conservation of angular momentum, the fundamental physical principle behind gyroscopic actuation:

A precession torque τ_ψ results in a precession speed $\dot{\psi}$, causing an induced torque in ϕ, proportional the spinning speed $\dot{\alpha}$.

There are two more aspects to be stressed. The first one regards the reversed principle, in which an angular speed $\dot{\phi}$ results in an induced torque in ψ. In the context of this paper this would represent a twisting torque, and is therefore undesired. A solution to cancel the undesired torque components is to introduce a twin flywheel which spins and precesses symmetrically. This arrangement of flywheels is what was referred above as CMG but now with the reasoning behind it included. The second aspect to be stressed regards the linearity of the system. eq. (4.1) is a second order non-linear ordinary differential equation of which we want to derive a linear time-invariant mathematical model of the system. When the spinning speed is assumed to be constant:

$$\begin{cases} \psi_1 = -\psi_2 = \psi \\ \dot{\alpha}_1 = -\dot{\alpha}_2 = \dot{\alpha} \\ \ddot{\alpha} = 0 \end{cases}, \tag{4.2}$$

which leads to simplifications in order to linearize the system.

4.2.2. GOVERNING EQUATIONS OF MOTION
The equations of motion of the system represented in Figure 4.3 are derived following the *Lagrange* method as in [43]

$$\frac{\partial}{\partial t}\left(\frac{\partial T(q_i)}{\partial \dot{q}_i}\right) - \frac{\partial T(q_i)}{\partial q_i} + \frac{\partial R(q_i)}{\partial \dot{q}_i} + \frac{\partial U(q_i)}{\partial q_i} = Q_i, \tag{4.3}$$

in which $q_i \in \mathbb{R}^{6\times1}$ represents an array of the independent coordinates of the system for each degree of freedom, in this case the pendulation angles in [rad]: $\phi_A, \phi_B, \phi_C, \phi_D, \phi_E$

and the precession angle ψ. $T(q_i)$, $U(q_i)$ and $R(q_i)$ are functions of q_i, representing the system's kinetic, potential and dissipative energies, in [J]. The symbol $Q_i \in \mathbb{R}^{6 \times 1}$ represents an array of the external loading applied to each independent coordinate system q_i, in this case a precession torque τ_ψ and wind load F_A. It is assumed that both flywheels have a diameter D_f, mass M_f and inertia I_f in [m], [kg] and [kgm²], respectively. In the remaining part of this section the formulations for the kinetic, potential and dissipative energies are established, as well as the loading terms. The first step to achieve this is to define a relative position vector for each frame of reference. Let $\vec{p}_i^I \in \mathbb{R}^{3 \times 1}$ represent the position vector of FoR i (where i can be A, B, etc...) relative to FoR I in [m]. Then the potential energy U contained in the system is given by:

$$U = g\left(M_b \cdot \vec{p}_B^I + M_f \cdot \left(\vec{p}_{C_1}^I + \vec{p}_{C_2}^I\right) + M_t \cdot \vec{p}_{E'}^I\right) \cdot I.\vec{k} + k_\psi \psi^2, \tag{4.4}$$

where $I.\vec{k} \in \mathbb{R}^{3 \times 1}$ in [m] is a unitary vector pointing int the Z direction of I. To ensure numerical stability, a torsional spring term K_ψ in [Nm] is added to the potential energy. This term must be small enough such that it does not affect the system's dynamics in the frequency range of interest.

Now that the formulation for the potential energy has been defined, it is still necessary to introduce the formulation for the total kinetic energy T. This one is split in 2 components, a translational component (T_t) and a rotational one (T_r)

$$T = T_t + T_r. \tag{4.5}$$

Let $\vec{v}_i^I$ be the time derivative of $\vec{p}_i^I$, then the kinetic energy is given by:

$$\begin{cases} T_t = \frac{1}{2}\left(M_b \cdot |\vec{v}_B^I|^2 + M_f\left(|\vec{v}_{C_1}^I|^2 + |\vec{v}_{C_2}^I|^2\right) + M_t \cdot |\vec{v}_{E'}^I|^2\right) \\ T_r = \frac{1}{2}\left(I_t \cdot \dot{\phi}_E^2 + \vec{\omega}_{C_1}^T \cdot J_f \cdot \vec{\omega}_{C_1} + \vec{\omega}_{C_2}^T \cdot J_f \cdot \vec{\omega}_{C_2}\right) \end{cases}, \tag{4.6}$$

where the superscript T is the transpose operator, $J_f \in \mathbb{R}^{3 \times 3}$ in [kgm²] a diagonal matrix representing the principal inertia tensor of the flywheels:

$$J_f = \begin{bmatrix} I_f/2 & 0 & 0 \\ 0 & I_f & 0 \\ 0 & 0 & I_f/2 \end{bmatrix}, \tag{4.7}$$

and $\vec{\omega}_{C_j} \in \mathbb{R}^{3 \times 1}$ the angular velocity vector of the flywheels in their respective frame of reference, in [rads^{-1}]:

$$\vec{\omega}_{C_j} = \begin{bmatrix} \dot{\phi}_{C_j} \\ \dot{\alpha}_{C_j} \\ \dot{\psi}_{C_j} \end{bmatrix}, \qquad j \in [1,2]. \tag{4.8}$$

Since the FoR C_j is attached to FoR B it is necessary to translate the rotations of B to C_j. This is achieved using transformation matrices [13]. Hence $\vec{\omega}_{C_j} \in \mathbb{R}^{3 \times 1}$ in [rads^{-1}] is given by eq. (4.9):

$$\vec{\omega}_{C_j} = \begin{bmatrix} X_{C_j}^B & Y_{C_j}^{C_j} & Z_{C_j}^{C_j} \end{bmatrix} \begin{bmatrix} \dot{\phi}_b \\ \dot{\alpha}_j \\ \dot{\psi}_j \end{bmatrix}, \tag{4.9}$$

in which $X_{C_j}^B \in \mathbb{R}^{3 \times 1}$ is a non-dimensional unit vector in the x-direction of coordinate frame B observed from coordinate frame C_j. The equivalent applies to the remaining terms of the transformation matrix, see [25]. Finally, in the context of this research, the angular velocity vectors of the flywheels in [rads^{-1}] in their reference frame is given by:

$$
\begin{aligned}
\vec{\omega}_{C_1} &= \begin{bmatrix} cos(\psi) & 0 & 0 \\ sin(\psi) & 1 & 0 \\ 0 & 0 & 1 \end{bmatrix} \begin{bmatrix} \dot{\phi}_b \\ \dot{\alpha} \\ \dot{\psi} \end{bmatrix}, \\
\vec{\omega}_{C_2} &= \begin{bmatrix} cos(\psi) & 0 & 0 \\ -sin(\psi) & 1 & 0 \\ 0 & 0 & 1 \end{bmatrix} \begin{bmatrix} \dot{\phi}_b \\ -\dot{\alpha} \\ -\dot{\psi} \end{bmatrix}.
\end{aligned}
\tag{4.10}
$$

Now with the potential and kinetic energies defined, the two remaining terms to be described are: the dissipative energy function $R(q_i)$ and the external loading terms Q_i. The dissipative energy function is given by

$$
R = \frac{1}{2}\left(b_A \dot{\phi}_A^2 + b_C \dot{\psi}^2 + b_D \dot{\phi}_D^2 + b_{aero} |\vec{v}_{E'}^I|^2 \right),
\tag{4.11}
$$

in which b_i represents the damping of the body in [Nms] to which the reference frame i is attached. b_{aero} represents the coefficient of the linearized aerodynamic damping of the tower in [Nsm^{-1}] [43]:

$$
b_{aero} = \rho_{air} D_t L_t C_D \overline{V_w},
\tag{4.12}
$$

where ρ_{air} is the air density in [kgm^{-3}], D_t the tower diameter in [m], C_D the non-dimensional aerodynamic drag coefficient of the tower and $\overline{V_w}$ the mean wind speed in [ms^{-1}].

Finally the last terms to be introduced are the forcing terms Q_i, with these being

$$
\begin{cases}
Q_A = F_A \cdot L_b \\
Q_B = F_A \cdot L_g \\
Q_C = \tau_\psi \\
Q_D = F_A \cdot L_s \\
Q_E = F_A \cdot L_t / 2
\end{cases},
\tag{4.13}
$$

in which τ_ψ is the precession torque applied to the flywheels in [Nm], *i.e.* the total torque exerted to press both flywheels. The wind load on the tower F_A is given by eq. (4.14), [43]:

$$
F_A = \frac{1}{2}\rho_{air} D_t L_t C_D V_w^2
\tag{4.14}
$$

4.2.3. LINEAR TIME-INVARIANT STATE-SPACE

The dynamics of the system are governed by a set of non-linear, second-order, ordinary differential equations resulting from eq. (4.3). The linear approximation of this system, around its equilibrium point, is given by a first-order *Taylor* series expansion. This allows a representation of the system's dynamics in the following state-space form:

$$G = \begin{cases} \dot{x} = \mathscr{A}x + \mathscr{B}x \\ y = \mathscr{C}x + \mathscr{D}u \end{cases} \quad , \tag{4.15}$$

where $G \in \mathbb{R}^{3 \times 3}$ represents a multiple input, multiple output (MIMO) state-space system model, $x \in \mathbb{R}^{12 \times 1}$ is the state-array, $u \in \mathbb{R}^{3 \times 1}$ the input array, $y \in \mathbb{R}^{3 \times 1}$ the output array, $\mathscr{A} \in \mathbb{R}^{12 \times 12}$ the dynamics matrix (*i.e.* the *Jacobian* of $\dot{x}$ relative to x), $\mathscr{B} \in \mathbb{R}^{12 \times 3}$ the input matrix (*i.e.* the *Jacobian* of $\dot{x}$ relative to u), $\mathscr{C} \in \mathbb{R}^{3 \times 12}$ the output matrix (*i.e.* the *Jacobian* of y relative to x) and $\mathscr{D} \in \mathbb{R}^{3 \times 3}$ the direct feed through matrix (*i.e.* the *Jacobian* of y relative to u). The state, input and output arrays are:

$$x = \begin{bmatrix} \dot{y}'_K \\ y'_K \\ \phi_A \\ \dot{\phi}_A \\ \phi_B \\ \dot{\phi}_B \\ \dot{\psi} \\ \psi \\ \dot{\phi}_D \\ \phi_D \\ \dot{\phi}_E \\ \phi_E \end{bmatrix}, u = \begin{bmatrix} \ddot{y}_K \\ F_A \\ \tau_\psi \end{bmatrix}, y = \begin{bmatrix} y_{E''} \\ \psi \\ y_{B'} \end{bmatrix}, \tag{4.16}$$

with the crane tip accelerations $\ddot{y}_K$ in $[\text{ms}^{-2}]$ given by:

$$\ddot{y}_{E''} = \omega^2 \zeta_a(\omega) RAO_a(\omega) \quad , \tag{4.17}$$

where ω represents frequency in $[\text{rads}^{-1}]$, $\zeta_a(\omega)$ represents the free surface wave amplitudes spectra in [m] and $RAO_a(\omega)$ the non-dimensional magnitude of the vessel's frequency dependent Response Amplitude Operator (RAO).

To prevent numerical drift from the integration of $\ddot{y}_{E''}$, the variable y'_K is introduced to represent the filtered crane tip acceleration in $[\text{ms}^{-2}]$:

$$\begin{bmatrix} \ddot{y}'_K \\ \dot{y}'_K \end{bmatrix} = \begin{bmatrix} -2\zeta_f \omega_c & -\omega_c^2 \\ 1 & 0 \end{bmatrix} \begin{bmatrix} \dot{y}'_K \\ y'_K \end{bmatrix} + \begin{bmatrix} 1 \\ 0 \end{bmatrix} [\ddot{y}_K], \tag{4.18}$$

4.2.4. STANDARD DEVIATION AND MOST PROBABLE MAXIMUM

In section 4.4, standard deviation and most probable maximum are the two quantities used to assess the performance of the proposed control system. Given the wide range of system properties and environmental conditions to be considered, the computations of these quantities are performed in the frequency-domain, reducing the computational effort, with respect to otherwise needed in time-domain. Let us consider an arbitrary time signal x, with a power spectral density (PSD) defined as follows:

$$S_x(\omega) = \frac{x_a(\omega)^2}{2\Delta\omega} \quad , \tag{4.19}$$

where $x_a(\omega)$ represents the amplitude of x and $\Delta\omega$ the frequency step in [rads^{-1}]. The standard deviation and the most probable maximum can then be determined from the nth-order moment of this spectrum, defined as:

$$m_{n,x} = \int_0^\infty \omega^n S_x(\omega)\, d\omega. \tag{4.20}$$

By definition, the standard deviation of x is then given by:

$$\sigma(x) = \sqrt{m_{0,x}}. \tag{4.21}$$

In the context of this work, due to the narrow banded wave spectrum, the probability density function of x can be approximated as a *Rayleigh* distribution [60]:

$$f(x) = \frac{x}{\sigma^2} e^{-\frac{x^2}{2\sigma^2}}. \tag{4.22}$$

Thus, the most probable maximum of a signal x is then given by:

$$\text{MPM(x)} = \sqrt{2m_{0,x}\ln(\text{N})}, \tag{4.23}$$

in which ln(N) represents the natural logarithm of the number of cycles N:

$$N = \frac{T}{2\pi} \cdot \sqrt{\frac{m_{2x}}{m_{0x}}}\quad, \tag{4.24}$$

with T being the time interval necessary to perform the tower installation, in [s].

4.2.5. Case Study Definition

For the synthesis and analysis of a CMG controller a case-study is considered. The case-study looks at the installation of a *DTU* 10 [MW] OWT tower [18] at Figueira da Foz Wind Farm (Portugal), by the semi-submersible crane vessel (SSCV) *Prometheus* [44], see Figure 4.2c. The tower is suspended 3 [m] above the foundation, before the crane-operator proceeds to finalize the installation. The SSCV *Prometheus* is subjected to beam-waves, *i.e.* waves approaching the vessel from the side. Waves and wind are modeled using a *JONSWAP* and *Kaimal* spectra [43], respectively. A reference set of environmental conditions is provided in Table 4.3. A 30 year data set of site-specific weather conditions [2] is used for the workability calculations.

For the sake of clarity, the summary of the parameters is split in 3 parts: Baseline System Characteristics (Table 4.1), CMG Characteristics (Table 4.2) and Operational Details (Table 4.3). System characteristic refers to the set of system properties/characteristics defining the baseline case, including the installation setup, wind turbine tower and mathematical model parameters. The dimensions and characteristics of the control moment gyroscope actuator are provided in Table 4.2. For controller synthesis and performance analysis, a set of operational details is provided in Table 4.3.

High-pass filter, eq. (4.18)

Table 4.1: Baseline system characteristics [43].

Description	Notation	Value	Unit
Air density	ρ_{air}	1.293	[kgm^{-3}]
Gravitational acceleration	g	9.81	[ms^{-2}]
Crane tip height	H_k	176	[m]
Crane tip damping	b_A	1.75×10^7	[Nms]
Hoisting cable length	L_b	29.25	[m]
Hook block mass	M_b	50×10^3	[kg]
Sling length	L_s	10	[m]
Tower height	L_t	115	[m]
Tower diameter	D_t	5.5	[m]
Tower mass	M_t	600×10^3	[kg]
Tower moment of Inertia	I_t	66.125×10^7	[kgm^2]
Tower drag coefficient	C_D	0.65	[-]
HPF cut-off frequency	ω_c	0.1	[rads^{-1}]
HPF damping ratio	ζ_f	0.7	[-]
Additional system damping	b_D	1.5×10^4	[Nms]

Table 4.2: Control moment gyroscope characteristics [67].

Description	Notation	Value	Unit
Height	L_g	5.75	[m]
Flywheels' diameter	D_f	2.5	[m]
Flywheels' spinning speed	$\dot{\alpha}$	3.0×10^2	[rads^{-1}]
Flywheels' mass	M_f	18.5×10^3	[kg]
Flywheels' moment of inertia	I_f	35×10^3	[kgm^2]
Precession stiffness	K_ψ	1.0	[Nm]
Precession damping	b_C	4.63×10^3	[Nms]
Torque limit	$\tau_\psi^{\lim}$	2.0×10^6	[Nm]
Accelerometer Sensor Delay	τ_S	1.0×10^{-1}	[s]

Table 4.3: Operational Details [43].

Description	Notation	Value	Unit
Reference significant wave height	H_s^r	3.0	[m]
Reference waves peak period	T_p^r	8.0	[s]
Reference average wind speed	$\overline{V_w^r}$	5.0	[ms^{-1}]
Installation tolerance	$y_{E''}^{\lim}$	1.5	[m]
Installation Duration	T_{install}	120	[s]
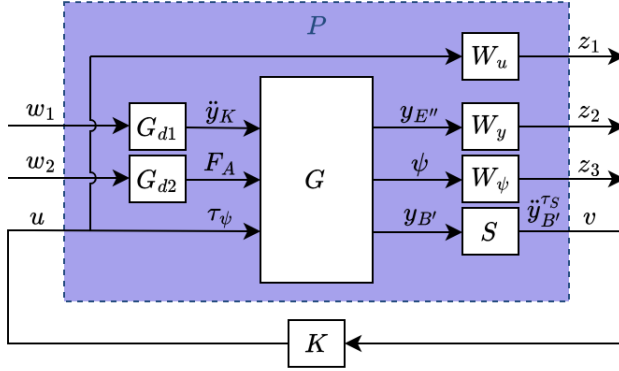
Figure 4.4: mixed-sensitivity design for optimal control.

4.3. CONTROLLER SYNTHESIS

Recall that the primary goal of this work is to assess the effectiveness of a scissored pair CMG in enhancing the workability of offshore operations. A key aspect to reach the goal is to design an adequate controller, which provides a trade-off between an effective reduction of tower bottom motions and actuator usage. Therefore, a model-based optimal control approach is proposed for the controller synthesis.

4.3.1. MIXED-SENSITIVITY FRAMEWORK OVERVIEW

Two main sources of disturbance are considered, crane-tip accelerations ($\ddot{y}_K$) caused by waves, and aerodynamic loads (F_A) caused by wind. These disturbances induce tower bottom motions ($y_{E''}$), increasing the chance of operational downtime. To prevent this, a feedback-loop with a controller K is implemented. The controller determines the input torque (τ_ψ) based on the acceleration measurement of the CMG ($\ddot{y}_{B'}$) combined together in vector z. To ensure that performance and actuation requirements are met simultaneously, the control problem is defined in a mixed-sensitivity design [111], as shown in Figure 4.4. The disturbance transfer functions G_{d1} and G_{d2} are used to convert the exogenous inputs [111] w_1 and w_2 into crane tip accelerations ($\ddot{y}_K$) and aerodynamic loads (F_A), respectively. The output variables are: tower bottom position $y_{E''}$, precession angle ψ and the position of the CMG center of gravity $y_{B'}$. The variable S represents the sensor transfer function: a double derivative of a 4th order Padé approximation of a delay τ_S [14], see Table 4.2. The transfer function outputs $\ddot{y}_{B'}^{\tau_S}$, the CMG acceleration signal with the delay, corresponding to measurement channel v. The functions W_y, W_u and W_ψ are weighting transfer functions which are used to adjust the trade-off between performance and actuation. To finalize, the goal of the optimization framework is to minimize the exogenous outputs z [111], in other words the weighted performance channels, which in this case are $y_{E''}$, $y_{B'}$ and τ_ψ. The following subsections discuss in detail the modeling of disturbances and weighting functions.

4.3.2. $\mathcal{H}_\infty$ SYNTHESIS

The mixed-sensitivity framework combines the control requirements into one multi-objective optimization problem. In the present work this optimization is solved by minimizing the $\mathcal{H}_\infty$ norm between the exogenous inputs w and exogenous outputs z. This norm is defined as the peak of the maximum singular value of the frequency response of the multiple input, multiple output (MIMO) system. This offers a great advantage compared to manual loop-shaping when a compromise between performance and actuation is required. The minimization algorithm of the $\mathcal{H}_\infty$ norm is well described in the literature [111, 45] and widely available.

4.3.3. DISTURBANCES AND SENSOR MODELING

The controller K obtained from the proposed mixed-sensitivity framework minimizes the peak of the maximum singular value spectrum of P between w and z. To achieve effective disturbance rejection, it is crucial to incorporate disturbance transfer functions into the mixed-sensitivity framework. This ensures that the control action is concentrated in frequency regions where the system is most vulnerable to disturbances.

To this end, the disturbance transfer functions G_{d1} and G_{d2}

$$G_{d1} = \frac{9.5 \times 10^{-4} s^2}{s^4 + 0.38 s^3 + 1.18 s^2 + 0.22 s + 0.32}, \tag{4.25}$$

$$G_{d2} = \frac{40 s}{s^2 + 0.04 s + 4 \times 10^{-4}}, \tag{4.26}$$

with s being the generalized frequency [14], are approximated based on the numerically computed wind and wave spectra [43], as shown in Figure 4.5. To highlight the most energetic frequency ranges, dominant frequency regions (DFR) are also marked in yellow and orange, for wind and waves respectively. In practice, the disturbance spectra continuously evolve with changing environmental conditions. However, for controller synthesis purposes, it is assumed that their overall shape and amplitude are well represented by the reference environmental conditions defined in Table 4.3.

4.3.4. WEIGHTING FUNCTIONS

The weighting functions have two purposes. The first is to normalize the output signals, such that the optimization results are not affected by their absolute values. The second is to emphasize the importance of each output in the optimization. As result of a manual iterative process we arrived at the weighting functions shown in Figure 4.6. These are:

$$\begin{cases} W_u = \frac{6s^2}{s^2 + 14s + 10^2} \times 10^{-5} \\ W_y = 10^0 \\ W_\psi = \frac{5.5}{s^2 + 0.14s + 0.1^2} \times 10^{-2} \end{cases}, \tag{4.27}$$

in which W_u is designed with a low input penalty at lower frequencies to compensate for the double derivation performed by the sensor S. In contrast, W_ψ imposes a larger penalty at lower frequencies, preventing excessive precession angle amplitudes that could jeopardize the model's linearity. As result of these weighting functions, the controller in
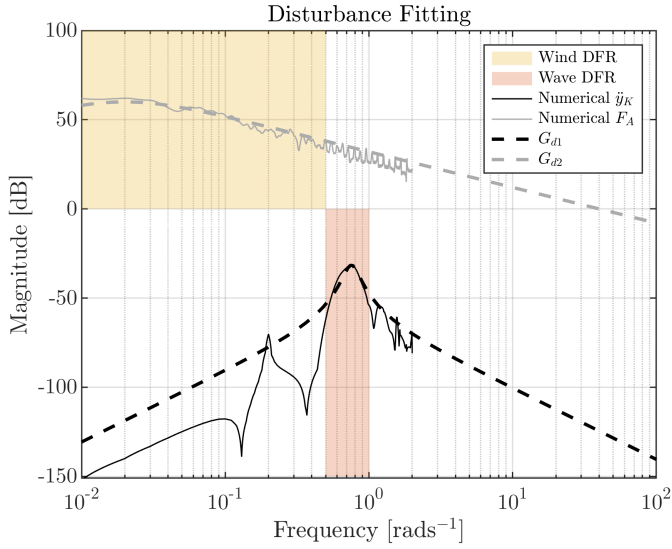
Figure 4.5: Disturbance modeling. Approximation of the numerically computed disturbance spectra with the transfer functions G_{d1} and G_{d2}. The dominant frequency ranges of wind and wave loads are marked yellow and orange, respectively.
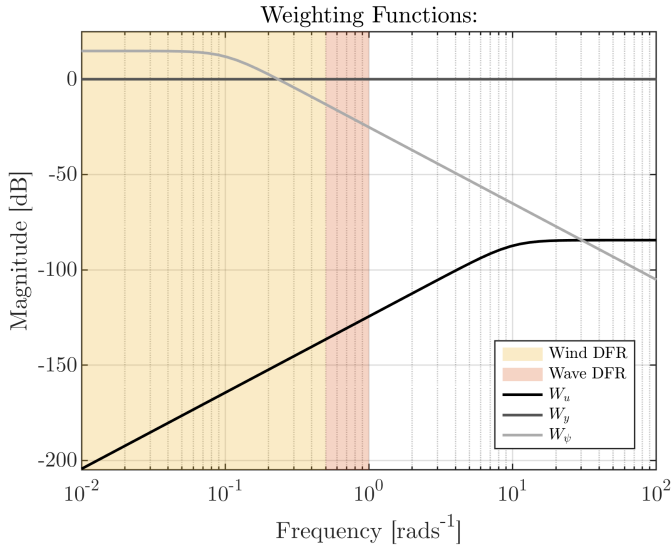
Figure 4.6: Frequency response spectra of the weighting functions for controller synthesis. The dominant frequency ranges of wind and wave loads are marked yellow and orange, respectively.
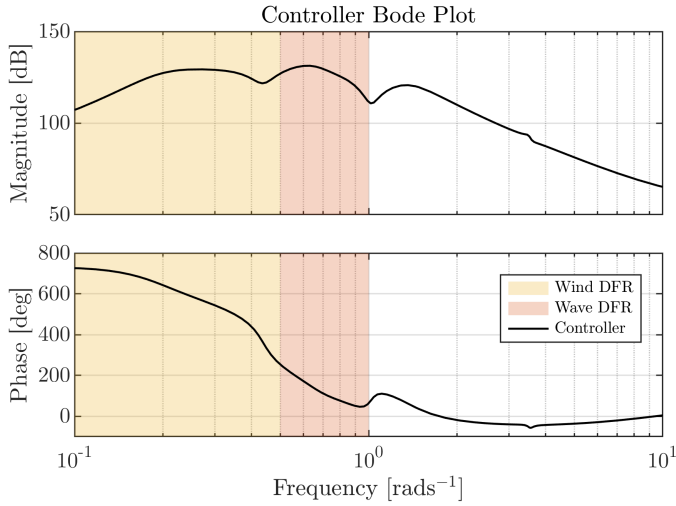
Figure 4.7: Magnitude and phase plots of the controller resulting from the optimization of the $\mathcal{H}_\infty$ norm of the plant P. The dominant frequency ranges of wind and wave loads are marked yellow and orange, respectively.

Figure 4.7 is obtained. The controller displays roll-off towards low and high frequencies, reducing the risk of instabilities caused by high-frequency noise and mitigating too large precession angles caused by low-frequency disturbances. As result, the control action is concentrated in the dominant frequency range of crane tip accelerations. The coming section discusses the effect of this controller on the closed-loop system dynamics.

4.4. RESULTS AND ANALYSIS

This section provides an in-depth analysis of control system's performance and robustness. The assessment is split into three parts: 1) Closed-Loop Response; 2) Robustness and Performance; and finally 3) Workability. The workability is evaluated in the context of the case-study introduced in section 4.2.5, where *Prometheus SSCV* [44] performs the installation of a 10 [MW] offshore wind turbine tower at Figueira da Foz Wind Farm (Portugal) [6].

4.4.1. CLOSED-LOOP RESPONSE

The goal of the feedback controller is to reduce wind and wave induced motions. Figure 4.8 compares the tower bottom motion response to disturbances, in open and closed-loop. It is possible to observe two types of controller action: damping and wave disturbance rejection, with the latter located between the first and second system modes. Active payload damping has been previously introduced [82], and it constitutes the current industry standard. However, alone it only has the ability to target the response amplitude at resonant frequencies, being unable to reduce the system's response outside these regions. The $\mathcal{H}_\infty$ mixed-sensitivity framework here proposed, combines active damping with crane-tip disturbance rejection, enhancing motion reduction in a larger range of frequencies.

4
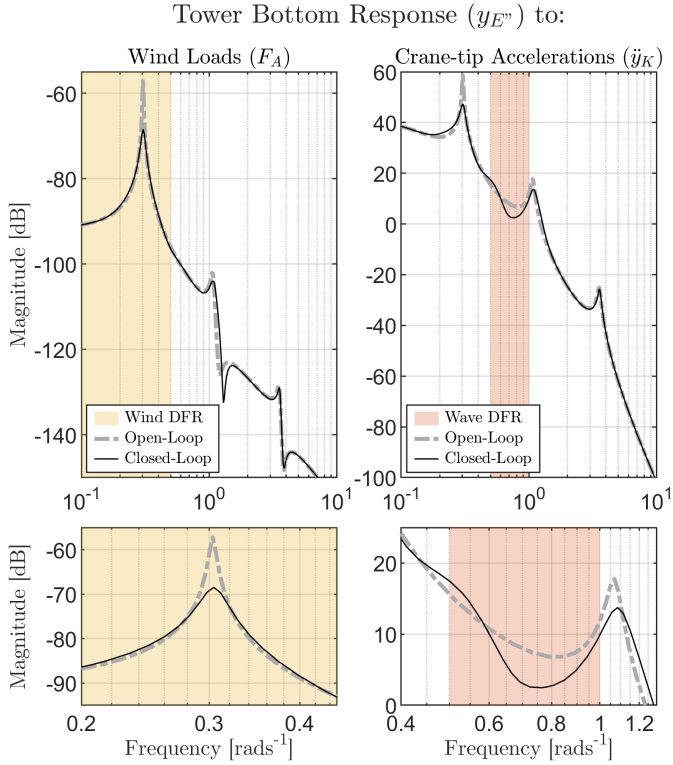
Figure 4.8: Frequency response functions of the tower motions to crane tip accelerations and wind loads. A comparison between the open and closed-loop systems, left and right. The dominant frequency ranges of wind and wave loads are marked yellow and orange, respectively. Bottom zooms in on the specified frequency ranges.
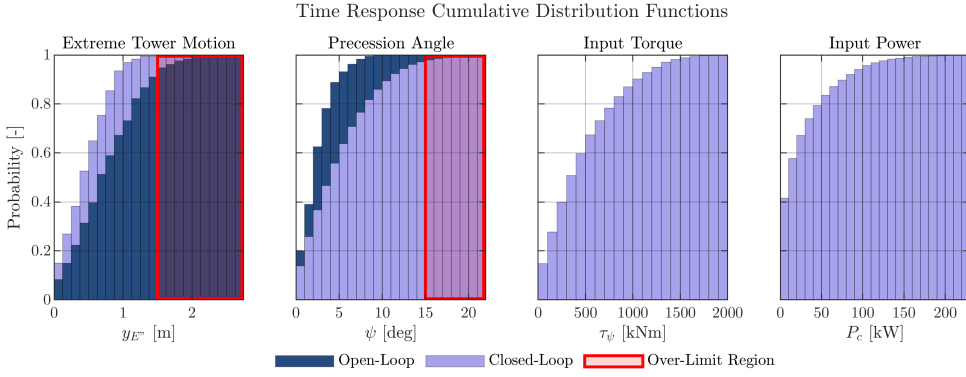
Figure 4.9: Discrete cumulative probability distribution functions of the open and closed-loop time responses of the system in reference environmental conditions *i.e.:* H_s = 3 [m] , T_p = 8 [s], and $\overline{V_w}$ = 5 [ms^{-1}], see Figure 4.12.

To demonstrate the capabilities of the CMG motion control system in enhancing the floating installation of a wind turbine tower in reference environmental conditions (Table 4.3), an analysis of a 30 minutes response of the system in open and closed-loop is presented in Figure 4.9, in the form of discrete cumulative probability density functions (CDFs), derived from the time signals of Figure 4.12, in the Appendix. The dark blue bars represent the CDFs of the open-loop system, while the lighter blue colored bars correspond to the closed-loop CDFs. The translucent red regions indicate areas where a limit has been exceeded. In the open-loop configuration, 9% of extreme tower motions (i.e., the maximum tower bottom excursion in a motion cycle) surpass the 1.5 [m] installation limit (as defined in Table 4.3). In contrast, the proposed control system reduces this probability to 0.5%, demonstrating the motion control system's effectiveness at mitigating tower motions.

To evaluate the validity of the proposed linear model, the precession angle of the flywheels during operation is analyzed. The results indicate that the precession angle exceeds 15 degrees for less than 3% of the time, leading to an overestimation of the CMG-generated reaction moment by at most 1% in over 97% of cases. Furthermore, 95% of the required torque to actuate the CMG remains below 1300 [kNm], while the power demand exceeds 110 [kW] in only 5% of cases, with the power being the product of the precession torque τ_ψ and precession speed $\dot{\psi}$. This represents a significant reduction in actuation demands compared to a previous study [67], underscoring the benefits of the proposed controller synthesis framework as an alternative to manual loop-shaping.

4.4.2. ROBUSTNESS AND PERFORMANCE

To evaluate the robustness and performance of the proposed motion control system, the stability margin, motion reduction, and actuator usage maps are presented in Figure 4.10. These maps contain information regarding the system's response across all possible combinations of hoisting cable lengths (L_b) for a given range of tower sizes (L_t), while maintaining a constant crane-tip height (see Table 4.1). The black dots represent the baseline system Table 4.1, on which the controller synthesis is based. The smaller dots
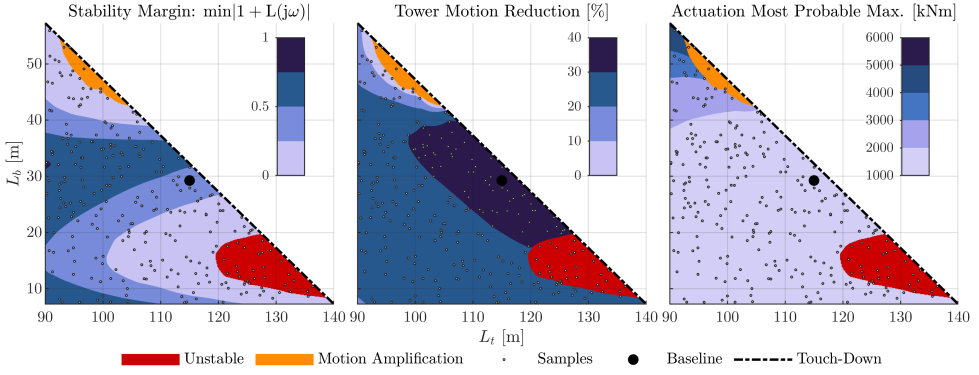
Figure 4.10: System's maps. Stability, motion reduction and actuator usage maps for different tower sizes (L_t) and hoisting cable lengths (L_b). These results are computed assuming the reference environmental conditions Table 4.3. *Crameri* colormap [36].

are system samples for specific combinations of L_b and L_t. The dashed-line represents the finalization of the installation when the tower gets in contact with the foundation. For the sake of consistency, the tower mass is defined as a function of tower length, varying with the third power of the scaling factor [43].

The stability margin is defined as the shortest distance of the *Nyquist* curve of the loop transfer function to the point -1 [14], with the loop transfer function being

$$L(s) = -G_{3,3}SK \quad , \tag{4.28}$$

with $G_{3,3}$ being the open-loop transfer function between the precession torque τ_ψ and the position of the CMG $y_{B'}$, see Figure 4.4. This stability margin definition holds as long as the system is closed-loop stable, *i.e.* that the number of counter clock-wise encirclements of the point -1 made by the *Nyquist* plot of $(1 + L(s))$ is equal to the number of right half plane poles of $L(s)$.

According to the stability margin map, the proposed controller guarantees the stability of the system for towers between 90 and 120 meters long. Beyond 120 [m], an unstable region marked in red is visible. A significant portion of the parameter space displays stability margin values between 0.25 and 0.75, corresponding to an allowable loop-gain uncertainty ranging between 33 and 300% .

Tower motion reduction is defined as the relative standard deviation reduction, between the open and closed-loop systems. A consistent reduction of 20 to 40% is observed for most of the cases. Yet, for tower lengths between 93 and 105 meters, the control system amplifies tower motions just before touch-down, instead of attenuating them, although it remains stable..

The third and last map refers to the most probable maximum torque input. For a large portion of the parameter-space it remains below 2000 [kNm], being consistent with the time domain data previously presented. Interestingly, it is possible to observe that for a combination of smaller towers with large hoisting lengths a larger torque is required.
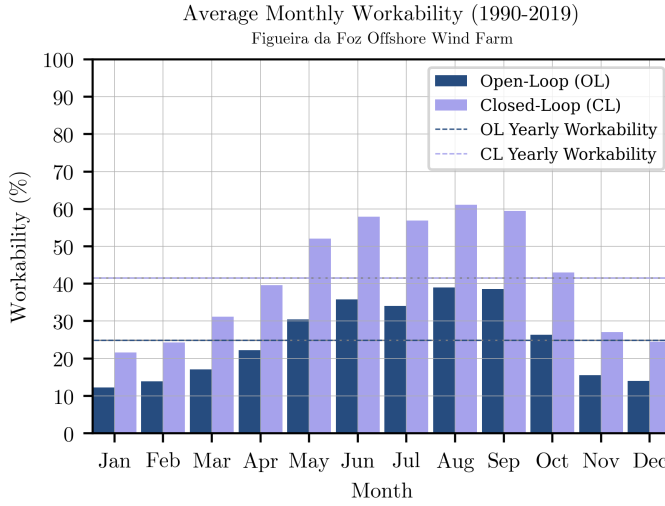
Figure 4.11: Workability at Figueira da Foz offshore wind farm in beam seas.

4.4.3. Workability Analysis

Now we have all elements in place to perform a workability analysis of the baseline system. The result is shown in Figure 4.11. It is the result of an analysis taking into account 30 years of weather records at *Figueira da Foz Wind Farm* (Portugal) [6]. A workable weather condition means that the following two criteria are satisfied during the installation time $T_{install}$, see Table 4.3: 1) The most probable maximum tower bottom motion must not exceed $y_{E''}^{lim}$; and 2) The most probable maximum actuator torque must not exceed τ_{ψ}^{lim}.

The dark blue bars in Figure 4.11 represent the open-loop workability, while the light colored bars the closed-loop workability. The dashed lines represent the average yearly workability. According to these results it is possible to observe that in closed-loop the system consistently displays higher workability than in open-loop. The absolute difference is amplified in summer and reduced in winter. The winter months display the lowest workability values, down to 12% in open-loop and 21% in closed-loop. In contrast, the summer months display the highest workability values, up to 39% in open-loop and 61% in closed-loop. This seasonal pattern is explained by the more challenging and unstable weather conditions in winter than in summer. However, the most clear indicator of the added benefit of the proposed control system is the average yearly workability. The control moment gyroscope with the proposed controller leads to an increase of the yearly workability from 25% in open-loop to 41% in closed-loop. Given the day-rate of heavy-lift vessels, 16% percentage points difference in yearly workability can translate in significantly increased installation window. Moreover, the effectiveness of the proposed motion compensation system holds in both side and off-lead directions, offering a significant improvement over conventional tugger-line systems. This highlights the potential of control moment gyroscopes for floating installation of offshore wind turbines.

4.5. CONCLUSIONS

This paper explores the modeling and control of a scissored pair control moment gyroscope, attached to the crane's hook, to mitigate wind turbine tower motions during installation. A detailed derivation of a linear time invariant model for this system is presented, and a mixed-sensitivity $\mathcal{H}_\infty$ framework is proposed for the controller synthesis. The resulting controller outputs a precession torque, given a translation acceleration signal of the control moment gyroscope. In closed-loop the first and second system modes are more damped and the controller is able to part,ially reject wave disturbances located between the natural frequencies of these modes. As result, a 20 to 40% tower motion reduction is observed across a wide range of tower sizes and payout lengths, whilst maintaining precession torque under 2000 [kNm] for most of the parameter space.

The workability of the open and closed-loop systems is compared in the context of a case-study based on 30 years of wind and wave records at Figueira da Foz wind farm (Portugal). In closed-loop, a consistent workability increase is observed, resulting in a 16 percentage point difference in yearly workability from 25% in open-loop to 41% in closed-loop.

APPENDIX

Figure 4.12: Time response of the open and closed-loop systems in reference environmental conditions, *i.e.: H_s* = 3 m , T_p = 8 s, and $\overline{V_w}$ = 5 m/s .

5

CONCLUSIONS AND RECOMMENDATIONS

This chapter summarizes the key conclusions on motion compensation for the floating installation of wind turbines and discusses recommended directions for future research.

5.1. CONCLUSIONS

The results of this thesis demonstrate that wave-induced motions can significantly compromise the installation of offshore wind turbine towers. However, their impact on workability can be mitigated using a hook-mounted active control moment gyroscope, where model-based control techniques proved to play a key role in balancing performance, robustness, and actuator usage. This conclusion is detailed in the remainder of this chapter and results from achieving the objective of this thesis:

intro recap removed

> **Thesis Objective:** To develop a methodology for assessing the impact of wind- and wave-induced motions on the floating installation of wind turbine towers and exploring their mitigation through (novel) motion compensation techniques.

5.1.1. A FREQUENCY-DOMAIN FRAMEWORK FOR WORKABILITY PREDICTIONS

Floating crane-vessels are an attractive alternative to jack-up vessels for wind turbine installations. Their size and versatility allow the installation of larger turbines, farther offshore. However, the impact of wind and wave loads on their workability was so far unknown in the context of wind turbine tower installation. With the goal of bridging this gap in the literature, the first contribution of this thesis was:

> **Contribution I**: A frequency-domain method to assess the impact of waves and wind on the workability of floating installations of wind turbine towers.

The frequency-domain framework was applied in the in the context of a case-study and verified against WEC-Sim. The outcome of the verification procedure confirms the hypothesis that tower motions are strongly coupled to vessel motions, but not the opposite. Furthermore, a sensitivity analysis of the model parameters, revealed that: 1) larger towers tend to reduce motions; 2) heavier hook-blocks tend to increase motions; 3) sling angle has little influence on tower motions

A workability assessment was performed considering 30 years of weather records, showing that the installation is significantly affected by wave-induced motions. Furthermore, with an average yearly workability of 25%, beam-waves do not compromise the operation as much as head-waves. This is explained by the lower hydrostatic stiffness of the vessel in roll when compared to pitch. Finally, a dynamic error budgeting analysis shows that the disturbances at 0.3 and 0.4 rad/s contribute the most for tower motions.

These outcomes allow to conclude that floating installation of offshore wind turbine towers can benefit from motion compensation. However, the lack of reference data regarding the dynamics of semi-submersible crane-vessels compromises open-research in the field, which motivated the second contribution of this thesis:

> **Contribution II**: Introduction of an open-source semi-submersible crane-vessel (*SSCV Prometheus*) and respective data.

The relevance of this contribution is demonstrated by the sustained interest in *SSCV Prometheus'* dataset .

5.1.2. FULL-SCALE EXPERIMENTAL DATA ANALYSIS

The framework earlier introduced relies on a set of assumptions, such as linearity and time invariance. Given the complex and uncontrolled environment in which offshore installations take place, such set of assumptions can lead to shortcomings of the model. To prevent it, physical experiments ca be used for validation. However, in the context of offshore operations, scaling laws do not permit an accurate scaling of wind and wave loads simultaneously. Therefore, the third contribution of this thesis focused on gathering, sharing and analyzing motion data from the first-ever full-scale floating installation of an offshore wind turbine tower.

> **Contribution III**: A motion dataset from the first full-scale floating installation of a wind turbine tower and an analysis of its dynamic behavior.

5.1.3. MODEL-BASED CONTROL FOR GYROSCOPIC MOTION COMPENSATION

As shown so far, wind and wave induced motions significantly affect workability, and addressing this can lead to reduced installation times. Currently, active damping tugger

---

Since the its release in February 2024 up until the present time (February 2025), *SSCV Prometheus'* dataset was downloaded over 150 times.

lines constitute an industry standard in motion control. With limited actuation capacity in the side-lead direction and generally designed to handle a wide variety of payload types and sizes, these tugger lines do not answer to the specific needs of the offshore wind market. With a goal of providing a more tailored solution, this thesis investigates the use and control of a hook-mounted active control moment gyroscope (CMG), leading to the fourth and final contribution of this work:

> **Contribution IV**: Development of a model-based control strategy for a gyroscopic actuator to enhance the workability of floating installation of wind turbine towers.

In this work, the floating installation of an offshore wind turbine tower is modeled as an interconnected set of pendulums, masses and flywheels. The proposed actuator consists of a scissored pair of gyroscopes, having as control input a precession torque. This torque is made a function of the CMG's translational acceleration by means of a feedback loop with a controller. The lack of system damping and the fact that wave disturbances occur away from natural frequencies, creates a challenge difficult to overcome with manual model-free controller synthesis, such as PID control. Instead, a mixed sensitivity $\mathcal{H}_\infty$ optimal control framework is proposed, offering a more effective and streamlined alternative to manual loop-shaping. The resulting controller combines damping and disturbance rejection actions, significantly reducing tower motions for a wide range of payout lengths and tower sizes. Regarding the yearly workability of *SSCV Prometheus* at Figueira da Foz wind farm, this one is shown to increase from 25% in open-loop to 41% in closed-loop. To finalize, this work demonstrates the potential of gyroscopic actuation in the field of offshore payload motion compensation, and highlights the added value of model-based control techniques in this field.

5.2. Recommendations

This thesis investigates the floating installation of offshore wind turbine towers and explores the use of active motion compensation to enhance their workability. The results are clear: wave loads significantly impact installation, but their effects can be partially mitigated using active control moment gyroscopes. This work serves as a stepping stone in the field, and further research is recommended to consolidate and expand its findings. To address this, we outline several directions for future research.

5.2.1. Operation

In this work, the mitigation of payload motions was investigated based on three main operational assumptions: (1) beam waves, (2) aligned wind and wave directions, and (3) focus on tower installation. To provide a more comprehensive perspective on the problem, these assumptions should be challenged in future work.

Furthermore, the complexity of assembling floating wind turbines offshore has led the industry to conduct their assembly onshore before towing them offshore. An alternative to this long and costly process is to perform the turbine assembly directly offshore. Therefore, it is recommended to investigate the potential of motion control strategies in enabling floating to floating installation.

5.2.2. MODELING

In the context of the case study here presented, tower to vessel interactions are shown to be negligible. However, this assumption does not hold for heavier payloads as shown in the literature. To address this limitation, in the future it is recommended to perform the identification of a linear model of dynamic response of *SSCV Prometheus.*

5.2.3. GYROSCOPIC ACTUATION

Despite the promising results of employing gyroscopic actuation for the floating installation of wind turbines, its full potential in offshore heavy-lift operations remains unexplored. Increasing the number of flywheels could extend its motion compensation capabilities across the entire horizontal plane. Additionally, future improvements may involve simultaneously controlling both the spinning and precession speeds while operating over a wider range of precession angles. Ultimately, this can be formulated as a co-design problem, where the actuator and controller are developed in parallel.

Two other relevant aspects for further research are: 1) the impact of dynamic positioning on workability and payload motion control; and 2) enhancing the performance and robustness of the gyroscopic actuator through more advanced control strategies, such as gain-scheduling.

5.2.4. VALIDATION

As a result of a trade-off between complexity and accuracy, this thesis opted for using reduced-order models of the system. On one hand, their linear and time-invariant properties enabled the use of stochastic methods, significantly reducing the cost of workability estimations, while also allowing the application of well-established frequency-domain techniques for controller design. On the other hand, these same properties limited the analysis of nonlinear phenomena such as wind and wave misalignment and directional wave spreading. Therefore, future research should validate the applicability of reduced-order models for controller synthesis when considering these non-linearities.

Finally, the analysis of full-scale offshore measurements presented in this thesis provided a unique perspective on the dynamics of floating installation of wind turbines. However, conducting additional measurements in more demanding weather conditions would result a richer dataset, essential for model validation.

ACKNOWLEDGEMENTS

With the closing of this chapter, it feels good to remember how it all started: an online meeting in the heart of rural South Australia, at Flinders Chase Farm on Kangaroo Island, when Corona was still just a rumor. I wore the only shirt I had for **Peter** to introduce me to **Jan-Willem**. Coming from a background of fluids and maritime engineering, I was fascinated by the chance to learn about systems and control, though I wondered if it might be too ambitious to pursue a PhD in a field I was not yet familiar with. **Jan-Willem** and **Peter** reassured me and I decided to take the step. Well, here we are now.

As with any PhD, this was a journey full of troughs and crests, during which I learned a lot and became a more resilient and driven person. First of all, thank you **Peter** and **Jan-Willem** for trusting me with this project, and for valuing my well-being whenever it was needed. **Jan-Willem**, your pragmatism and contagious enthusiasm created a path to explore exciting and challenging topics while ensuring their relevance for this work. **Peter**, thank you for the coffee breaks, for inviting me to thesis committees, for helping shaping this work into a well-rounded story from day one, and for your remarkable attention to detail. I am deeply grateful for this experience.

I would also like to thank **Ad Reniers**, **Xinshu Zhang**, **Jurnan Schilder**, **Wim van Horssen**, and **Bayu Jayawardhana** for being part of the committee, for taking the time to assess this thesis, and for providing valuable feedback and questions that allow me to highlight the work and lessons learned hidden behind each chapter.

Thanks to my paranymnphs, **Emanuel** and **Miguel**, for all the moments we shared on the way here. **Emanuel**, I still find it fascinating how we can differ and overlap at the same time. While I often need about $\mathcal{O}(10)$ more words than you to say the same, I am grateful that together we can derive our own non-dimensional numbers, enjoy classical music concerts, or hang from a self-made anchor several meters above the ground. Afilhado **Miguel**, given how our friendship began, having you here as my paranymnph feels very special. Your sense of responsibility and commitment is inspiring. Even at more than 2000 km away, you have always been present, whether to celebrate or to offer support. Thank you.

A highlight of my PhD was being onboard the largest crane vessel in the world (*SSCV Sleipnir*) for the installation of a wind turbine. Although preparing for the campaign absorbed almost my entire first year, it gave me the chance to meet people from whom I learned a lot. **Alejandro**, **Thom**, **Nick**, **Chris**, and the rest of the **DOT** team: the sheer amount of work and responsibility such a young team was able to carry is nothing short of inspiring. **Thijs**, **Rolf**, **Joris**, **Cris**, **Sandor**, and the rest of the **HMC** team, thank you for the countless meetings, calls, and insights that kept my work grounded in reality. **Jesus**, thank you for your openness and light spirit, and for that "quick" tower ascent that ended hours later with us dripping in sweat, the very definition of type II fun.

A special thank you to the **Técnico Solar Boat (TSB)** team, especially to **Sebastião Beirão**, always ready to debug C++ via text message at any time of day. I still wonder about

your sleeping habits, MVP! It was a privilege to work once again with the TSB team, this time not on a racing boat but on a set of novel motion-measuring units essential for the offshore campaign. The expertise and dedication of this team are unique and inspiring, and makes me truly proud. Thanks also to **Wim** and **Will** for always being willing to help in the lab and for taking care of equipment orders. And to **Erica**, **Sandra**, **Francy**, and the secretaries: thank you for always providing support to the staff and for organizing social events that are crucial for the department's cohesion.

Julie and **Peter**, it was a pleasure to meet you and work together. We started off in the harshest phase of the pandemic, with countless online meetings to prepare for the offshore campaign. Soon after, we found ourselves in offshore trainings, backing each other day and night at sea, and eventually writing a paper together (emphasis on *together*), which earned a well-deserved award. **Peter** (a.k.a. the king of plotting), your proactiveness and drive, always combined with a light spirit, were key. **Julie**, your kindness and attention to detail are remarkable, and it was great traveling together in the U.S. before NAWEA. I am truly grateful for having shared this journey with you.

To my dear office colleagues and friends, first of all, *goede morgen*. I will always carry great memories from our time together. Thank you for the discussions, the fun moments, and the support throughout what is probably the longest professional solo project of our lives. **Jonas**, which card did I choose? Where others see obstacles, you see opportunities, and this mindset makes the lives of those around you lighter and more fun. I look forward to many more moments together, whether looking at the plot of the day or slacklining over the *Schie*. **Dr. Becker** (soon-to-be Dr. Domingos speaking here), the way you juggle and excel in so many aspects is as impressive as **Paul**'s magic tricks (to whom I'll come back in a minute). Thank you for being a co-author on all our non-materialized papers, for the Community Mondays and dinners, the epic dance moves, and the climbing sessions. **Amr**, habibi, next week is your turn! Yours and **Wassima**'s wedding was the most epic I have ever been to, not sure Emanuel has fully recovered from the tinnitus though. Thank you for your calm presence and your caring nature, always reaching out when it was most needed. **Daniel**, the control guru, thank you for your patience and for showing me the beauty of control theory. I still admire the way you organize your lunch box. **Unai**, thanks for the visits in Delft and climbing, looking forward to more trips together. I find it impressive how much energy you have and how you managed to balance a PhD, a job, and a family. **Livia**, my long-hours office partner, thank you for bringing a sense of fashion into the office. Go-go-go! **Maarten**, your diligent and methodical way of working are a reference, though not always applicable, like when a casual walk turned into an hours-long hike after a missed turn. I have to admit, I enjoyed it. **Atin** and **Daan**, thank you for your friendly and calming presence and for always being willing to help. **Mees** and **Matteo**, thanks for showing how to work hard and party harder. **Marion**, **Guido**, and **Sander**, thank you for bringing so much life into our group. **Rogier**, thank you for your willingness to teach and explain control, as well as for the amazing DJ sets. **Sebastiaan**, your door was always open whenever results didn't make sense or for techno party suggestions. **Sam**, thanks for the climbing sessions, the nights out, the BBQs, and for providing a much-needed Australian vibe in the office. **Afra**, thank you for so many fantastic days in the office, the most amazing ones ever. Mamma mia, **Paul**! Thank you for all the "magic" moments together, inside and outside the office, it's impressive to see so much talent concentrated

in just one person. **Salim**, the Italian tiles are just better. Thank you for the fun in the office, on the tatami, when going out, or really, wherever you are. **Methab**, thanks for the open and friendly vibes, whether in the office, at BBQs, or at Halloween in Boulder. **Jesse**, thank you for your contagious excitement during the many hours we spent looking at Bode plots. **Tim**, besides all the fun moments (and the banana plant I let die), I am deeply grateful for our career discussions, which eventually led me to complete a traineeship at the European Commission. Thank you. **Leendert**, that ice bath did nothing, I could barely walk for three days. Thank you for the interesting discussions and for being an example of discipline. Thanks also to **Claudia**, **Frida**, **Fred**, **Clara**, **Luca**, **Alex**, **Coen**, **Lotfi**, **Elias**, and **Tushar** for all the spontaneous talks that helped distract from work. **Alexandra**, **Robin**, **Sachin**, **Tristan**, **Fafa**, and **Fritz**, thank you for bringing fresh air to the team, and for all the talks over coffee, lunch, or a *biertje*. And to my master students, **Job** and **Thom**, thank you for the long discussions during your theses, it was great working with you on such exciting topics.

Obrigado **Manas**, for being a home no matter where, for being a support net as well as a source of life-long joyful memories, ob ab. Despite all the careful planning and vision one might have, life remains stochastic in nature, and certain low-probability realizations turn out to be key. **Aldo**, if we had not randomly met at the beach that summer day, my life today would perhaps be much different. Besides the friendship we developed, having lived and studied with you was the best catalyst I could have had in my academic path. Obrigado meu pouroo. **Gonçalo Augusto**, thank you for all the rejuvenating and fun moments together—they always made my holidays in Portugal special. **António** and **Eusébio**, meus kangaroos, just yesterday we were in the upside-down building fences. Thank you for all the unforgettable memories. **Raquel**, thank you for all the support and advice when deciding to take the step of engaging in this PhD.

Kathi and **Guillaume**, thanks for all the visits, trips, fun moments, and the most amazing memories together, I look forward to many more to come. Dear **Rike**, thank you for showing me that feelings are not ruled by equations, that there is no black and white but shades of grey, and that when life gives oranges they are meant to be eaten. I am grateful for how you helped me grow and for all the moments together. **João Francisco** (aka **Lenny**), you have been a constant presence since I first moved to the Netherlands. I admire your curious, honest, and trusting way of approaching friendships. I cannot thank you enough for all the help with the van, the long night talks, the time spent at your place, the BBQs and because without you this path would have felt much more empty. **Ticha**, thank you for always having the door of your place open and making me feel at home. Thank you for not being shy in giving your honest opinion when asked, for showing empathy when needed, and for asking the right questions at the right moments. Above all, thank you for being someone I can hold on to. Over the past three years, I had the luck of sharing my living space with some good friends: **Marina**, **Parreira**, and **Nuno**, who one day will make me look back at this period of life with a smile and a true feeling of *saudade*. Marina, thank you for your bubbliness, kindness, and for being an amazing alarm clock. Parreira, my climbing partner, thank you for always being willing to help with anything and for keeping the house livable, I owe you a lot. Nuno, rato-esquilo, thank you for being a good listening ear, for being so caring, and for being such a fantastic source of life. **Pedro**, seu pirata, thank you for the long talks and reuniões de condomínio, it never

"Altogether on the mountains side,
(...)
When you reach the top – don't stop,
Start again."

-Dreadzone

Bibliography

[1] "Active Heave Compensation", Seaqualize. *Available: `https://www.seaqualize.com/`*. 2023.

[2] "ESOX", LAUTEC. *Available: `https://esox.lautec.com/map/`*. Mar. 2023 [Online].

[3] "Map Viewer", European Marine Observation and Data Network. *Available: `https://emodnet.ec.europa.eu/geoviewer/`*. 2023.

[4] "Next Generation Jack-Up, Voltaire", Jan de Nul. *Available: `https://www.jandenul.com/news/jan-de-nul-launched-worlds-tallest-next-generation-jack-installation-vessel-voltaire/`*. 2023.

[5] "Offshore Renewable Energy", European Union. *Available: `https://energy.ec.europa.eu/topics/renewable-energy/offshore-renewable-energy_en`*. 2023.

[6] "Portugal to Launch First Offshore Wind Auction, Eyes 10 GW by 2030", Reuters. *Available: `Portugaltolaunchfirstoffshorewindauction,eyes10GWby2030`*. 2023.

[7] "Salome Mesh User's guide: Introduction to Mesh", Salome. *Available: `https://docs.salome-platform.org/latest/main/index.html`*. 2023.

[8] "TU Delft on Board the World Largest Crane Vessel for Exploring Future Offshore Wind Turbines", Delft University of Technology. *Available: `https://www.tudelft.nl/en/2021/3me/october/tu-delft-on-board-the-world-largest-crane-vessel-for-exploring-future-offshore-wind-turbines`*. 2023.

[9] "A review of land use, visibility and public perception of renewable energy in the context of landscape impact". In: *Applied Energy* 276 (2020), p. 115367. ISSN: 0306-2619. DOI: `https://doi.org/10.1016/j.apenergy.2020.115367`. URL: `https://www.sciencedirect.com/science/article/pii/S0306261920308795`.

[10] International Energy Agency. *Offshore Wind Outlook 2019*. Tech. rep. IEA, 2019.

[11] CF Alsop, GA Forster, and FR Holmes. "Ore unloader automation—a feasibility study". In: *Proceedings of IFAC on Systems Engineering for Control Systems* (1965), pp. 295–305.

[12] Matthieu Ancellin and Frédéric Dias. ""Capytaine: A Python-Based Linear Potential Flow Solver"". In: *Journal of Open Source Software* 4.36 (Apr. 2019), p. 1341. DOI: `10.21105/joss.01341`.

[13] Stanislav Aranovskiy, Igor Ryadchikov, Nikita Mikhalkov, Dmitry Kazakov, Alexey Simulin, and Dmitry Sokolov. "Scissored pair control moment gyroscope inverted pendulum". In: *Procedia Computer Science* 186 (2021), pp. 761–768.

[14] Karl Johan Åström and Richard Murray. *Feedback systems: an introduction for scientists and engineers*. Princeton university press, 2021.

[15] Panagiota Atzampou, Peter C Meijers, Apostolos Tsouvalas, and Andrei V Metrikine. "Contactless control of suspended loads for offshore installations: Proof of concept using magnetic interaction". In: *Journal of Sound and Vibration* (2024), p. 118246.

[16] Panagiota Atzampou, Peter C Meijers, Apostolos Tsouvalas, and Andrei V Metrikine. "Contactless control of suspended loads for offshore installations: Proof of concept using magnetic interaction". In: *Journal of Sound and Vibration* 575 (2024), p. 118246.

[17] Aurélien Babarit and Gérard" Delhommeau. ""Theoretical and Numerical Aspects of the Open Source BEM Solver NEMOH"". In: *Proceedings of EWTEC*. Nantes, France, Sept. 2015.

[18] Christian Bak et al. *"The DTU 10-MW Reference Wind Turbine"*. Tech. rep. Technical University of Denmark, 2013.

[19] Roxana Bardan. *Temperatures Rising: NASA Confirms 2024 Warmest Year on Record*. National Aeronautics and Space Administration. 2024. URL: https://www.nasa.gov/news-release/temperatures-rising-nasa-confirms-2024-warmest-year-on-record/.

[20] Merel van Beek, R van Dijk, K van Dalen, and Andrei Metrikine. ""A Feasibility Study for the Installation of 10 MW Offshore Wind Turbines with an SSCV"". MA thesis. Delft University of Technology, 2018.

[21] Tom Bergeron. *Ørsted official: Ocean Wind 1 remains on schedule for 2025*. ROI-NJ. 2023. URL: https://www.roi-nj.com/2023/09/05/industry/energy-utilities/orsted-official-ocean-wind-1-remains-on-schedule-for-2025/.

[22] Fernando D Bianchi, Hernán De Battista, and Ricardo J Mantz. *"Wind Turbine Control Systems: Fundamental Concepts in Wind Turbine Engineering"*. Springer, 2010. ISBN: 9781846284922. DOI: 10.1115/1.802601.ch14.

[23] Mehmet Bilgili and Hakan Alphan. ""Global Growth in Offshore Wind Turbine Technology"". In: *Clean Technologies and Environmental Policy* 24.7 (2022), pp. 2215–2227.

[24] Richard Bishop and A Hassan. ""The Lift and Drag Forces on a Circular Cylinder Oscillating in a Flowing Fluid"". In: *Proceedings of the Royal Society of London. Series A. Mathematical and Physical Sciences* 277.1368 (1964), pp. 51–75. ISSN: 0080-4630. DOI: 10.1098/rspa.1964.0005.

[25] Tom Bloemers and Roland Tóth. "Equations of motion of a control moment gyroscope". In: (2019).

[26] R Bos and P Wellens. ""Fluid-Structure Interaction Between a Pendulum and Monochromatic Waves"". In: *Journal of Fluids and Structures* 100 (2021), p. 103191. DOI: 10.1016/j.jfluidstructs.2020.103191.

[27] L.G. Buitendijk. ""Floating Installation of Offshore Wind Turbine Foundations"". MA thesis. Delft University of Technology and Van Oord, 2016.

[28] Colin J Carlson, Gregory F Albery, Cory Merow, Christopher H Trisos, Casey M Zipfel, Evan A Eskew, Kevin J Olival, Noam Ross, and Shweta Bansal. "Climate change increases cross-species viral transmission risk". In: *Nature* 607.7919 (2022), pp. 555–562.

[29] Ju-Hwan Cha, Myung-Il Roh, and Kyu-Yeul Lee. "Dynamic response simulation of a heavy cargo suspended by a floating crane based on multibody system dynamics". In: *Ocean Engineering* 37.14-15 (2010), pp. 1273–1291.

[30] Anil K Chopra. *Dynamics of structures*. Pearson Education India, 2007.

[31] J.A. Cis and F.A.F. Tojo. "A Lipschitz condition along a transversal foliation implies local uniqueness for ODEs". In: *Electronic Journal of Qualitative Theory of Differential Equations* (13 2018), pp. 1–14. ISSN: HU ISSN 1417-3875. DOI: 10.14232/ejqtde.2018.1.13.

[32] Jimmy Bo Clarenburg. ""Efficient Design of Controlled Offshore Systems"". MA thesis. Delft University of Technology, 2014.

[33] GF Clauss and T Riekert. "Operational Limitations of Offshore Crane Vessels". In: *Proceedings of Offshore Technology Conference*. Houston, Texas, US, May 1990. DOI: 10.4043/6217-MS.

[34] European Commission et al. *GHG emissions of all world countries – 2023*. Publications Office of the European Union, 2023. DOI: doi/10.2760/953322.

[35] JL Cozijn, RJ van der Wal, and C Dunlop. ""Model Testing and Complex Numerical Simulations for Offshore Installation"". In: *Proceedings of ISOPE*. Vancouver, Canada, July 2008.

[36] Fabio Crameri. "Scientific colour maps". In: *Zenodo* 10 (2018).

[37] Our World in Data. *Installed capacity for different renewable technologies*. Renewable Capacity Statistics. 2024. URL: https://ourworldindata.org/grapher/installed-global-renewable-energy-capacity-by-technology.

[38] Hugo Díaz and C Guedes Soares. "Review of the current status, technology and future trends of offshore wind farms". In: *Ocean Engineering* 209 (2020), p. 107381.

[39] DOB-Academy. *FOX Project video - Offshore Campaign*. https://www.youtube.com/watch?v=BGcLoREJI-c. 2022.

[40] David Domingos, Panagiota Atzampou, Peter Meijers, Sebastião Beirão, Andrei Metrikine, van Wingerden, J.W., and Peter Wellens. ""First floating installation of an OWT Tower: Full-Scale Inertial Data"". In: *4TU.ResearchData* (2024). DOI: 10.4121/17ae06bb-7da0-4045-ac81-484fa52af13f.

[41] David Domingos, Panagiota Atzampou, Peter Meijers, Sebastião Beirão, Andrei Metrikine, van Wingerden, J.W., and Peter Wellens. "Full-scale measurements and analysis of the floating installation of an offshore wind turbine tower". In: *Ocean Engineering* (2024). DOI: 10.1016/j.oceaneng.2024.118670..

[42] David Domingos, Thom Kusters, Peter Wellens, and van Wingerden, J.W. "Model-Based Control of a Control Moment Gyroscope for Floating Installation of Wind Turbine Towers". In: *Submitted to Mechatronics Journal* (2025).

[43] David Domingos, Peter Wellens, and van Wingerden, J.W. "Frequency-Domain Framework for Floating Installation of Wind-Turbine Towers". In: *Ocean Engineering* (2023). DOI: 10.1016/j.oceaneng.2024.116952..

[44] David Domingos, Peter Wellens, and van Wingerden, J.W. "Prometheus: An Open-Source SSCV". In: *4TU.ResearchData* (2023). DOI: 10.4121/aa0a24fc-b7e2-4e05-b0cb-f1dc2af1c9ac.

[45] John Doyle, Keith Glover, Pramod Khargonekar, and Bruce Francis. "State-space solutions to standard H2 and Hinf control problems". In: *1988 American Control Conference*. IEEE. 1988, pp. 1691–1696.

[46] Caitlyn Eberle, Jack O'Connor, Liliana Narvaez, Melisa Mena Benavides, and Zita Sebesvari. "Interconnected disaster risks 2023: Risk tipping points". In: (2023).

[47] R.S. Ehrmann, K.M. Loftin, S. Johnson, and E.B. White. "Lock-in of Elastically Mounted Airfoils at a 90° Angle of Attack". In: *Journal of Fluids and Structures* 44 (2014), pp. 205–215. ISSN: 08899746. DOI: 10.1016/j.jfluidstructs.2013.10.008.

[48] Wind Europe. *Wind energy in Europe - 2023 Statistics and the outlook for 2024-2030*. Tech. rep. Wind Europe, 2023.

[49] Carolina Ganem-Karlen, Gustavo Javier Barea-Paci, and Soledad Elisa Andreoni-Trentacoste. "What It Takes to Go Net Zero: Why Aren't We There Yet?" In: *Towards Net Zero Carbon Emissions in the Building Industry*. Ed. by Ali Sayigh. Cham: Springer International Publishing, 2023, pp. 195–212. ISBN: 978-3-031-15218-4. DOI: 10.1007/978-3-031-15218-4_10. URL: https://doi.org/10.1007/978-3-031-15218-4_10.

[50] Jingjing Gao, Lei Wang, Rui Gao, and Jiangshuai Huang. "Adaptive control of uncertain underactuated cranes with a non-recursive control scheme". In: *Journal of the Franklin Institute* 356.18 (2019), pp. 11305–11317.

[51] Zhen Gao, Amrit Verma, Yuna Zhao, Zhiyu Jiang, and Zhengru Ren. ""A Summary of the Recent Work at NTNU on Marine Operations Related to Installation of Offshore Wind Turbines"". In: *Proceedings OMAE*. Madrid, Spain, June 2018.

[52] Ievgen Golovin and Stefan Palis. "Robust control for active damping of elastic gantry crane vibrations". In: *Mechanical Systems and Signal Processing* 121 (2019), pp. 264–278.

[53] Hossein Habibi and William O'Connor. "Payload motion control of rotary gantry and luffing cranes using mechanical wave concepts". In: *Transactions of the Institute of Measurement and Control* 39.11 (2017), pp. 1649–1662.

[54] Sunghun Hong, Houxiang Zhang, and Karl Henning Halse. ""Hydrodynamic and Environmental Modelling Influence on Numerical Analysis of an Innovative Installation Method for Floating Wind"". In: *Ocean Engineering* 280 (2023), p. 114681. DOI: 10.1016/j.oceaneng.2023.114681.

5

[55] Gerben Hoogendoorn, Wouter Van Den Bos, and Henk Polinder. ""Design in principle of crane vessel for flexible fully assembled wind turbine installation"". In: *Proceedings of International Conference on Advanced Intelligent Mechatronics*. IEEE. 2021, pp. 1083–1088.

[56] Leon Jabben and Jan van Eijk. ""Performance Analysis and Design of Mechatrnic Systems"". In: *Mikroniek* 51 (2011), pp. 5–12.

[57] Zhiyu Jiang. "Installation of offshore wind turbines: A technical review". In: *Renewable and Sustainable Energy Reviews* 139 (Apr. 2021), p. 110576. ISSN: 1364-0321. DOI: 10.1016/J.RSER.2020.110576.

[58] Zhiyu Jiang, Zhen Gao, Zhengru Ren, Ye Li, and Lei Duan. ""A Parametric Study on the Final Blade Installation Process for Monopile Wind Turbines Under Rough Environmental Conditions"". In: *Engineering Structures* 172 (2018), pp. 1042–1056.

[59] Karl Johan Åström and Richard M. Murray. *"Feedback Systems: An Introduction for Scientists and Engineers"*. Princeton University Press, 2021. ISBN: 0691135762. DOI: 10.5860/choice.46-2107.

[60] J M J Journée, W W Massie, and R H M Huijsmans. *"Offshore Hydromechanics"*. Delft University of Technology, 2015.

[61] B Kroft, Peter Wellens, J Bokhorst, and R van Dijk. "Motion Prediction of a Semi-Submersible Crane Vessel at Inconvenient Draft". MA thesis. Delft University of Technology, 2022.

[62] Bas J de Kruif and Bruno Rossin. "Pendulation control for dynamical positioning capable ship; considerations on actuator usage". In: *IFAC-PapersOnLine* 54.16 (2021), pp. 120–125.

[63] Bas J de Kruif and Bruno Rossin. "Pendulation Control for Dynamical Positioning Capable Ship: Considerations on Actuator Usage". In: *IFAC-PapersOnLine* 54.16 (2021), pp. 120–125. ISSN: 24058963. DOI: 10.1016/j.ifacol.2021.10.082.

[64] Nam-Kug Ku, Ju-Hwan Cha, Myung-Il Roh, and Kyu-Yeu Lee. "A Tagline Proportional-Derivative Control Method for the Anti-Swing Motion of a Heavy Load Suspended by a Floating Crane in Waves". In: *Engineering for the Maritime Environment* 227.4 (2013), pp. 357–366.

[65] Namkug Ku and Myung-Il Roh. "Dynamic Response Simulation of an Offshore Wind Turbine Suspended by a Floating Crane". In: *Ships and Offshore Structures* 10.6 (2015), pp. 621–634. ISSN: 1744-5302. DOI: 10.1080/17445302.2014.942504.

[66] Pijush Kundo, Ira Cohen, and David Dowling. *"Fluid Mechanics"*. Elsevier, 2016. ISBN: 978-0-12-405935-1. DOI: 10.1016/C2012-0-00611-4.

[67] Thom Kusters. "Gyroscopic Payload Motion Control for Floating Installation of Offshore Wind Turbine Towers". In: (2024).

[68] Lars Larsson. "Ship resistance and flow". In: *Published by The Society of Naval Architects and Marine Engineers, SNAME, The Principles of Naval Architecture Series, ISBN: 978-0-939773-76-3* (2010).

[69] M Lenton et al. "Global Tipping Points Report 2023". In: *University of Exeter* (2023).

[70] Frederick A Leve, Brian J Hamilton, and Mason A Peck. *Spacecraft momentum control systems*. Vol. 1010. Springer, 2015.

[71] *Lisnave distribui lucro de 1,5 milhões pelos trabalhadores*. ADN-Agência de Notícias. 2016. URL: https://www.adn-agenciadenoticias.com/2016/04/lisnave-distribui-lucro-de-15-milhoes.html.

[72] Jenny Yan Lu, Santhosh Kumar Mony, Henning Carlsen, and Carl Sixtensson. ""Solution to Design Challenges and Selections of Wind Turbine Installation Vessels"". In: *Proceedings of Offshore Technology Conference*. Houston, Texas, USA, May 2011.

[73] Oleg Makarov and Takashi Harada. ""Effective Approach to Modeling the Hydrodynamic Response of a Multibody System with Suspended Load in The Time Domain"". In: *Proceedings of Jc-IFToMM*. Kyoto, Japan, July 2022, pp. 95–102. DOI: 10.57272/jciftomm.5.0_95.

[74] Jay R Malcolm, Canran Liu, Ronald P Neilson, Lara Hansen, and LEE Hannah. "Global warming and extinctions of endemic species from biodiversity hotspots". In: *Conservation biology* 20.2 (2006), pp. 538–548.

[75] Pim der Male and Eliz-Mari Lourens. ""Operational Vibration-Based Response Estimation for Offshore Wind Lattice Structures"". In: *Proceedings of the Society for Experimental Mechanics Series*. Feb. 2015, pp. 83–96. DOI: 10.1007/978-3-319-15230-1.

[76] James F Manwell, Jon G McGowan, and Anthony L Rogers. *Wind energy explained: theory, design and application*. John Wiley & Sons, 2010.

[77] S. Marelli, C. Lamas, K. Konakli, C. Mylonas, P. Wiederkehr, and B. Sudret. *"UQLab user manual - Sensitivity analysis"*. Tech. rep. ETH Zurich, 2022.

[78] S. Marelli, C. Lamas, K. Konakli, C. Mylonas, P. Wiederkehr, and B. Sudret. *"UQLab: A Framework for Uncertainty Quantification in Matlab"*. Tech. rep. ETH Zurich, 2022. DOI: 10.1061/9780784413609.257.

[79] Iain A Martin and Rishad A Irani. "Dynamic modeling and self-tuning anti-sway control of a seven degree of freedom shipboard knuckle boom crane". In: *Mechanical Systems and Signal Processing* 153 (2021), p. 107441.

[80] C Meloni and G Dellino. *"Uncertainty Management in Simulation-Optimization of Complex Systems: Algorithms and Applications"*. Elsevier, 2015. ISBN: 978-1-4899-7547-8. DOI: 10.1007/978-1-4899-7547-8.

[81] Geert Meskers and Radboud van Dijk. ""A Damping Tugger System for Offshore Heavy Lifts"". In: *Proceedings of OMAE*. Vol. 44885. American Society of Mechanical Engineers. 2012, pp. 315–323.

[82] Geert Meskers and Radboud van Dijk. "A Damping Tugger System for Offshore Heavy Lifts". In: *International Conference on Offshore Mechanics and Arctic Engineering*. Vol. 44885. American Society of Mechanical Engineers. 2012, pp. 315–323.

[83] Ministerios: Economia e Mar, Ambiente e Acao Climatica e, Infraestruturas e Habitacao. *"Proposta Preliminar das Areas Espacializadas e dos Pontos para a Ligação à Rede Nacional de Transporte de Eletricidade"*. Tech. rep. Republica Portuguesa, 2023.

[84] C Mora, T McKenzie, IM Gaw, JM Dean, H von Hammerstein, TA Knudson, et al. *Over half of known human pathogenic diseases can be aggravated by climate change. Nat Clim Chang. 2022; 12 (9): 869-75.*

[85] Amir R. Nejad, Lin Li, Wilson Ivan Guachamin Acero, and Torgeir Moan. ""A Systematic Design Approach of Gripper's Hydraulic System Utilized in Offshore Wind Turbine Monopile Installation"". In: *Proceedings of OMAE*. Vol. 11A. 2018, pp. 1–10. ISBN: 9780791851326. DOI: 10.1115/OMAE2018-77228.

[86] Jorg Neupert, Tobias Mahl, Bertrand Haessig, Oliver Sawodny, and Klaus Schneider. ""A Heave Compensation Approach for Offshore Cranes"". In: *Proceedings of ACC*. Vol. 44885. IEEE. 2008, pp. 538–543.

[87] Jörg Neupert, Eckhard Arnold, Klaus Schneider, and Oliver Sawodny. "Tracking and anti-sway control for boom cranes". In: *Control Engineering Practice* 18.1 (2010), pp. 31–44.

[88] Nobuhiro Nojiri and Tsuneto Sasaki. ""Motion Characteristics of Crane Vessels in Lifting Operation"". In: *Proceedings of Offshore Technology Conference*. OnePetro. 1983.

[89] W. O'Connor and H. Habibi. "Gantry crane control of a double-pendulum, distributed-mass load, using mechanical wave concepts". In: *Mechanical Sciences* 4 (2 2013), pp. 251–261. ISSN: 2191916X. DOI: 10.5194/MS-4-251-2013.

[90] David Ogden, Kelley Ruehl, Yi-Hsiang Yu, Adam Keester, Dominic Forbush, Jorge Leon, and Nathan Tom. ""Review of WEC-Sim Development and Applications"". In: *International Marine Energy Journal* 5.3 (Dec. 2022). DOI: 10.36688/imej.5.293-303.

[91] E Ohnishi, I Tsuboi, T Egusa, and M Uesugi. "Automatic control of an overhead crane". In: *IFAC Proceedings Volumes* 14.2 (1981), pp. 1885–1890.

[92] Tristan Perez and Paul D Steinmann. "Analysis of ship roll gyrostabiliser control". In: *IFAC Proceedings Volumes* 42.18 (2009), pp. 310–315.

[93] Joseph A Pratt, Tyler Priest, and Christopher J Castaneda. *"Offshore pioneers: Brown and Root and the History of Offshore Oil and Gas"*. Elsevier, 1997.

[94] Lizet Ramirez, Daniel Fraile, and Guy Brindley. *"Offshore Wind in Europe"*. Tech. rep. WindEurope, 2019.

[95] Zhengru Ren, Zhiyu Jiang, Zhen Gao, and Roger Skjetne. ""Active Tugger Line Force Control for Single Blade Installation". In: *Wind Energy Journal* 21.12 (2018), pp. 1344–1358. ISSN: 10991824. DOI: 10.1002/we.2258. URL: https://doi.org/10.1002/we.2258.

[96] Zhengru Ren, Roger Skjetne, and Zhen Gao. ""A Crane Overload Protection Controller for Blade Lifting Operation Based on Model Predictive Control"". In: *Energies* 12.1 (2018), p. 50.

[97] Zhengru Ren, Roger Skjetne, Zhiyu Jiang, Zhen Gao, and Amrit Shankar. ""Integrated GNSS/IMU Hub Motion Estimator for Offshore Wind Turbine Blade Installation"". In: *Mechanical Systems and Signal Processing* 123 (2019), pp. 222–243. ISSN: 0888-3270. DOI: 10.1016/j.ymssp.2019.01.008. URL: https://doi.org/10.1016/j.ymssp.2019.01.008.

[98] Zhengru Ren, Amrit Shankar Verma, Behfar Ataei, Karl Henning Halse, and Hans Petter Hildre. "Model-free anti-swing control of complex-shaped payload with offshore floating cranes and a large number of lift wires". In: *Ocean Engineering* 228 (2021), p. 108868.

[99] Zhengru Ren, Amrit Shankar Verma, Behfar Ataei, Karl Henning Halse, and Hans Petter Hildre. "Model-free anti-swing control of complex-shaped payload with offshore floating cranes and a large number of lift wires". In: *Ocean Engineering* 228 (May 2021), p. 108868. ISSN: 0029-8018. DOI: 10.1016/J.OCEANENG.2021.108868.

[100] Hannah Ritchie. "What are the safest and cleanest sources of energy?" In: *Our World in Data* (2020). https://ourworldindata.org/safest-sources-of-energy.

[101] Hannah Ritchie and Pablo Rosado. "Fossil fuels". In: *Our World in Data* (2017). https://ourworldindata.org/fossil-fuels.

[102] Hannah Ritchie, Pablo Rosado, and Max Roser. "CO2 and Greenhouse Gas Emissions". In: *Our World in Data* (2023). https://ourworldindata.org/co2-and-greenhouse-gas-emissions.

[103] Hannah Ritchie, Pablo Rosado, and Max Roser. "Energy Production and Consumption". In: *Our World in Data* (2020). https://ourworldindata.org/energy-production-consumption.

[104] Hannah Ritchie, Pablo Rosado, and Max Roser. "Greenhouse gas emissions". In: *Our World in Data* (2020). https://ourworldindata.org/greenhouse-gas-emissions.

[105] Hannah Ritchie, Fiona Spooner, and Max Roser. "Biodiversity". In: *Our World in Data* (2022). https://ourworldindata.org/biodiversity.

[106] Parineak Romtrairat, Chanyaphan Virulsri, Panipat Wattanasiri, and Pairat Tangpornprasert. "A performance study of a wearable balance assistance device consisting of scissored-pair control moment gyroscopes and a two-axis inclination sensor". In: *Journal of Biomechanics* 109 (2020), p. 109957.

[107] Max Roser. "Why did renewables become so cheap so fast?" In: *Our World in Data* (2020). https://ourworldindata.org/cheap-renewables-growth.

[108] Hanspeter Schaub. "Rate-based ship-mounted crane payload pendulation control system". In: *Control Engineering Practice* 16.1 (2008), pp. 132–145.

[109] Job Schepers, David Domingos, Jelle ter Braak, Ivan van Winsen, and van Wingerden, J.W. ""Design of Gain-Scheduling Cascade Control for a Motion Compensated Gripper Frame"". In: *Journal of Physics: Conference Series* 2265.3 (May 2022), p. 032082. DOI: 10.1088/1742-6596/2265/3/032082. URL: https://dx.doi.org/10.1088/1742-6596/2265/3/032082.

[110] William E Singhose and Samuel T Towell. "Double-pendulum gantry crane dynamics and control". In: *Proceedings of the 1998 IEEE International Conference on Control Applications (Cat. No. 98CH36104)*. Vol. 2. IEEE. 1998, pp. 1205–1209.

[111] Sigurd Skogestad and Ian Postlethwaite. *Multivariable feedback control: analysis and design*. john Wiley & sons, 2005.

[112] C H K Williamson and R Govardhan. "VORTEX-INDUCED VIBRATIONS". In: *Annu. Rev. Fluid Mech* 36 (2004), pp. 413–55. DOI: 10.1146/annurev.fluid.36.050802.122128. URL: www.annualreviews.org.

[113] WindEurope. *Wind energy in Europe: 2021 Statistics and the outlook for 2022–2026*. https://windeurope.org/intelligence-platform/product/wind-energy-in-europe-2021-statistics-and-the-outlook-for-2022-2026/. 2022.

[114] Xianqing Wu and Xiongxiong He. "Partial feedback linearization control for 3-D underactuated overhead crane systems". In: *ISA transactions* 65 (2016), pp. 361–370.

[115] Yuna Zhao, Zhengshun Cheng, Zhen Gao, Peter Christian Sandvik, and Torgeir Moan. "Numerical study on the feasibility of offshore single blade installation by floating crane vessels". In: *Marine Structures* 64 (2019), pp. 442–462.

Curriculum Vitæ

David André FIDALGO DOMINGOS

Education

2020–2025	**Doctor of Philosophy in Systems and Control**
	Delft University of Technology, Delft, The Netherlands
	Thesis: *Motion Compensation for Floating Installation*
	of Offshore Wind Turbines
	Promotors: prof. dr. ir. Jan-Willem van Wingerden and dr. ir. Peter R. Wellens
2016-2019	**Master of Science in Maritime Engineering**
	Delft University of Technology, Delft, The Netherlands
	Thesis: *Manoeuvring Prediction of Foil-Assisted Vessels*
2012-2015	**Bachelor of Science in Naval Architecture and Maritime Engineering**
	cum laude
	Instituto Superior Técnico, Lisbon, Portugal

Experience

2025	**European Electricity Market Analyst Trainee**
	European Commission, Petten, The Netherlands
2019	**Computational Fluid Dynamics Engineer**
	Van Oossanen Naval Architects, Wageningen, The Netherlands
2019	**Naval Architect and Hydrodynamicist**
	Sun Concept, Olhão, Portugal
2015-2016	**Founder, Team Leader and Naval Architect**
	Dream team Técnico Solar Boat, Lisbon, Portugal
2015-2016	**President**
	Núcleo de Alunos de Engenharia Naval, Lisbon, Portugal

LIST OF PUBLICATIONS

JOURNAL PUBLICATIONS

5. **David A. Fidalgo Domingos**, Thom Kusters, Peter R. Wellens, Jan-Willem van Wingerden, *Model-Based Control of a Control Moment Gyroscope for Floating Installation of Wind Turbine Towers*, Mechatronics Journal, under review, 2025.

4. **David A. Fidalgo Domingos**, Panagiota Atzampou, Peter Christiaan Meijers, Sebastião Holbeche Beirão, Andrei V. Metrikine, Jan-Willem van Wingerden, Peter R. Wellens, *Full-Scale Measurements and Analysis of the Floating Installation of an Offshore Wind Turbine Tower*, Ocean Engineering, 2024.

3. **David A. Fidalgo Domingos**, Peter R. Wellens, Jan-Willem van Wingerden, *Frequency-Domain Framework for Floating Installation of Wind-Turbine Towers*, Ocean Engineering, 2024.

2. Job M. Schepers, **David A. Fidalgo Domingos**, Jelle ter Braak, Ivan van Winsen, Jan-Willem van Wingerden, *Design of Gain-Scheduling Cascade Control for a Motion Compensated Gripper Frame*, Journal of Physics, 2022.

1. Liliana A. Fidalgo Domingos, Enrique M. San Norberto, **David A. Fidalgo Domingos**, Miguel Martín-Pedrosa, Noelia Cenizo, Isabel Estévez, Álvaro Revilla, Carlos Vaquero, *Geometric and Hemodynamic Analysis of Fenestrated and Multibranched Aortic Endografts*, Journal of Vascular Surgery, 2020.

Included in this thesis.

[2] Awarded TU Delft *Best Wind and Ocean Energy Paper* of 2024.

[1] Awarded *Best Original Research* at Leipzig Interventional Vascular Course 2019 and *Fernando Martorell* award by Sociedad Española de Anomalias Vasculares in 2019.